Resource Allocation in 5G: NR Sidelink Mode 2 & Wi-Fi 6/7

Liu Cao

A dissertation
submitted in partial fulfillment of the
requirements for the degree of

Doctor of Philosophy

University of Washington

2024

Reading Committee:
Sumit Roy, Chair
Payman Arabshashi
Mahmood Hameed

Program Authorized to Offer Degree:
Electrical and Computer Engineering

University of Washington

Abstract

Resource Allocation in 5G: NR Sidelink Mode 2 & Wi-Fi 6/7

Liu Cao

Chair of the Supervisory Committee:
Sumit Roy
Electrical and Computer Engineering

5G/5G advanced era brings about two emerging wireless technologies: New Radio (NR) Sidelink (SL) and Wi-Fi 6/7. First, 5G New Radio (NR) Sidelink (SL) has demonstrated the promising capability for infrastructure-less cellular coverage. Understanding the fundamentals of the NR SL channel access mechanism, Semi-Persistent Scheduling (SPS), which is specified by the 3rd Generation Partnership Project (3GPP), is a necessity to enhance the NR SL Packet Reception Ratio (PRR). However, most existing works fail to account for the new SPS features introduced in NR SL, which might be out-of-date for comprehensively describing the NR SL PRR. The existing models ignore the relationships between SPS parameters and, therefore, do not provide sufficient insights into the PRR of SPS. This work proposes a novel SPS PRR model incorporating MAC collisions based on new features in NR SL. We extend our model by loosening several simplifying assumptions made in our initial modeling. The extended models illustrate how the PRR is affected by various SPS parameters. The computed results are validated via simulations using the network simulator (ns-3), which provides important guidelines for future NR SL enhancement work.

Second, new features brought by 5G New Radio V2X (NR-V2X) support multiple vehicular communication types (unicast, groupcast, and broadcast) to coexist in road scenarios.

However, the current standard does not specify the resource scheduling approach for groupcast to support such a new feature, which may severely degrade its packet delivery performance impacted by other communication types. In this paper, we investigate the scheduling and resource allocation approaches for a groupcast-based application, vehicle platooning, under the environment characterizing this new feature. We first analyze two baseline resource allocation approaches, i.e., Semi-persistent Scheduling (SPS) stated in the 3rd generation partnership project (3GPP) and Random Selection (RS), based on the metric of packet collision probability. Subsequently, considering the issues from baseline approaches, we develop an Improved Random Selection (IRS) scheme to decrease the collision probability. We further propose to employ Deep Deterministic Policy Gradient (DDPG) algorithm to overcome the impact of inter-vehicle collaboration in the platoon based on local information. A Monte Carlo simulator is then used to verify the analytical models' results. The numerical results show that IRS significantly mitigates the packet collision probability compared with the baselines. Meanwhile, DDPG outperforms IRS in terms of the packet collision probability as well as average scheduled delay and is more robust to the change in the environment.

Third, Downlink (DL) Multi-User (MU) Multiple Input Multiple Output (MU-MIMO) is a key technology that allows multiple concurrent data transmissions from an Access Point (AP) to a selected sub-set of clients for higher network efficiency in Wi-Fi 6 (IEEE 802.11ax). However, DL MU-MIMO feature is typically turned off as the default setting in AP vendors' products, that is, turning on the DL MU-MIMO may not help increase the network efficiency, which is counter-intuitive. In this thesis, we provide a sufficiently deep understanding of the interplay between the various underlying factors, i.e., channel state information (CSI) overhead and spatial correlation, which result in negative results when turning on the DL MU-MIMO. Furthermore, we provide a fundamental guideline as a function of operational scenarios to address the fundamental question "when the DL MU-MIMO should be turned on/off".

TABLE OF CONTENTS

LIST OF FIGURES

Figure Number Page

ACKNOWLEDGMENTS

I would like to express my greatest appreciation and highest respect to my academic supervisor, Dr. Sumit Roy. I'm so grateful that Dr. Roy would like to accept me as his new Ph.D. student in my second year when I had to find a new faculty advisor due to some reasons. During my new Ph.D. journey with Dr. Roy, he has given me a lot of guidance on my research projects and papers about Sidelink, PHY layer abstraction, Downlink MU-MIMO, etc. He can always enlighten me by giving me instructions on how to select a good research topic that is not only academically sound but also industrially contributing. I appreciate Dr. Roy for not only his dedicated guidance on my research but also his strong support on my future faculty career. I always remember what he told me "Life is not easy if you want to be successful", which will inspire me whenever I encounter any difficulties in my life.

Meanwhile, I thank all of my other supervisory committee members, Dr. Payman Arabshahi, Dr. Mahmood Hameed, and Dr. Mingwen Yang for their time in supervising me. I also thank other faculties at the UW, Dr. Tom Henderson and Dr. Akshay Gadre, for their guidance on my research.

I am deeply indebted to my parents, whose encouragement gave me the confidence to pursue my dreams, and their unconditional love provided me with the motivation to continue, even in the face of obstacles. I am so fortunate to have them as my parents, and this achievement is as much theirs as it is mine. I would like to extend my deepest gratitude to Ling Zou for her unwavering support, understanding, and patience on my PhD study and future career.

Many thanks to my colleagues in my lab, Hao Yin, Lyutianyang Zhang, Sian Jin, Xiangyu Gao, Collin Brady, Jesse (Kuan-Po) Chiu, Muyuan Shen, Juan V Leon Rosas, Laxman

Balamurugan. Many thanks to my colleagues from collaborative institutes/labs, Chunmei Liu, Peng Liu, Chen Shen, Fernando Cintrón, Richard Rouil (all from NIST), Jingyuan Zhang (Georgia Institute of Technology), and Qiancheng Li (UW NEWT Lab). I also thank my close friends in the U.S. including but not limited to, Wenqiu Ma, Ruixuan Wan, Mingfei Chen, Ran Wei, Qinlin Yu, Dongyu Wei, Yizhan Huang, Peiyang Li, Yuhua Nie, Yanxiao Sun, Haorui Ji, Dave Chen, Ning Wang, Junnan Kou, Yilin Wang, Yiheng Pan, Mengyue Sun, Tianqi Liu, Jie Hu, Ziwei Dong, Fan Liu, Yunxuan Li, Di An, Lingtao Shui, Yuqi Zhao, Huaiyu Wang, Kaiyang Zeng, Runlong Lin, Yuhao Ju, etc. I always enjoyed the moment with all of my colleagues and friends in the past five years, and sincerely hope our paths will cross again in the future!

During my Ph.D. study, I had two summer research internships. I took my first internship at Futurewei Technologies in Dallas, TX. I thank my colleagues, Tony Saboorian, Abbas Kiani, Amanda Xiang, Kaippallimalil John. Particularly, I thank Amanda Xiang for her supervision during my internship and her consistent help when I sought faculty positions. I also appreciate my second internship experience at MediaTek in San Diego, CA. I thank my colleagues, Shawn Tsai, Yahia Shabara, Parisa Cheraghi, Meng-Che Chang, Yu-Jen Ku.

I also wish to express my sincere appreciation to the University of Washington which was my dream school when I applied for the Ph.D. program five years ago. I felt so fortunate to be admitted by the UW ECE department and had the opportunity to work towards my Ph.D. degree. Receiving the Ph.D. degree from UW is bound to be one of the greatest honors in my life.

Finally, I want to thank myself. I have devoted all my efforts without reservation and regret in the past five years. This journey was not without its struggles, but every challenge provided a valuable lesson and helped shape the person I am today. As I move forward, I will carry with me the resilience and discipline this experience has instilled in the future.

DEDICATION

To my dear family

Chapter 1

INTRODUCTION

1.1 Background

In 5G/5G advanced era, two emerging wireless technologies have drawn intensive attention: New Radio (NR) Sidelink (SL) and Wi-Fi 6. Sidelink is a 3rd Generation Partnership Project (3GPP) standardized technology that enables direct user-to-user communications, with or without the assistance of a base station. Current sidelink (Release 16) has evolved from the device-to-device communication system developed for proximity services (ProSe) targeting public safety via the emergency first responder community. Sidelink is attractive in such uses because it provides support for users needing data connectivity with ultra-low latency and high-reliability requirements. These characteristics are also useful in a variety of other scenarios such as coverage extension to planned cellular networks, connectivity for Vehicle-to-Everything (V2X), communications for augmented/virtual reality (AR/VR) devices, and network support for intra-body sensors, leading to interests in expanding sidelink usage. In view of these emergent applications, 3GPP is currently developing Release 18 to further enhance sidelink technology. While Wi-Fi was first released to consumers in 1997, its standards have been continually evolving from 802.11b to current 802.11ax, resulting in faster speeds and networking efficiency for users. Over the past 20 years, Wi-Fi has evolved from megabit speeds to multi-gigabit speeds by populating new features. In Wi-Fi 6, new features such as OFDMA, MU-MIMO, 1024 QAM bring new opportunities for higher throughput in the indoor scenario. In particular, Wi-Fi 6/ 802.11ax is defined in IEEE Standard ax-2021. This is a high-efficiency wireless for the indoor scenario that emphasizes on higher network throughput. My research work primarily focuses on these two emerging wireless technologies from the fundamentals and optimization perspectives.

Semi-Persistent Scheduling in NR Sidelink Mode 2. A promising application for SL is support for mission-critical data connectivity needs with Ultra-Reliable Low-Latency Communications (URLLC) requirements. These characteristics are helpful in various scenarios, such as Vehicle-to-Everything (V2X), various first-responder use, and industrial IoT, leading to continued interest in expanding SL scope. SL mode 2 supports the formation of local-area, ad-hoc networks without cellular infrastructure (e.g., remote areas or complex propagation environments such as underground, undersea, or airborne). All such applications also bring new technical challenges for network formation over SL, e.g., the necessity to re-architect key primitives such as neighbor discovery, authentication, and efficient channel acquisition [1]. Because of this, enhancements to the current SL continue to be an active topic in 3GPP Rel-18/Rel-19 with several study items [2].

This work focuses on performance evaluation of the NR SL mode 2 Semi Persistent Scheduling (SPS) protocol, a distributed media access control (MAC) scheme that was initially introduced in Long Term Evolution (LTE) SL mode 4 (Release 14) and subsequently adopted for 5G NR. SPS enables all UEs in a decentralized network to monitor the channel, determine which resources are in use, and avoid utilizing these (in-use resources) for upcoming message transmissions. SL design has evolved from the original Rel-14 specifications to include 5G NR numerology, operate over multiple frequency bands such as FR2 (mmWave), and support more communication types (unicast and groupcast in addition to broadcast); correspondingly, this has led to updates in SPS design in terms of new parametrization to meet the reliability requirements faced with network reconfiguration and scalability.

Resource Allocation in 5G Platoon Communication. Vehicle-to-everything (V2X) communications over cellular networks (C-V2X) are being standardized by 3GPP to enable traffic safety and transport efficiency features within future connected intelligent transportation systems. C-V2X was initially defined as LTE-V2X in 3GPP Release 14 [3] for 4G LTE; it is currently evolving as NR-V2X starting from 3GPP Release 16 for 5G NR PHY to support advanced services such as vehicle platooning [4]. While LTE-V2X is only provisioned for broadcast transmissions, NR-V2X allows multiple communication types [5]. For example, in vehicle platooning: the platoon leader (PL) can communicate with platoon members (PM) using the groupcast mode while utilizing the broadcast mode to transmit periodic messages to vehicles that are not part of the platoon. The PL may also coordinate the movement of a group of PMs by broadcasting Basic Safety Messages (BSMs) cyclically [6].

NR-V2X defines two sidelink (NR-PC5) modes: sidelink Mode 1 signifies mechanisms that allow direct vehicular communications *within gNodeB coverage* where the gNodeB schedules sidelink resources for vehicles. The NR-V2X sidelink Mode 2 supports direct vehicular communications in *out-of-coverage* scenario [7]. In NR-V2X Mode 2 operation, a vehicle selects resources for communication autonomously by performing sensing on a resource pool prior to access to minimize V2X packet collisions [8]. Mode 2 resources are randomly selected from among the idle resources within the pool; however, this does not eliminate packet collisions resulting from the hidden terminal effects. Therefore, novel approaches that decrease the probability of packet collisions for platoon communication as a function of node density continue to be of significant interest for latency-sensitive applications.

This work investigates efficient resource allocation approaches for platoon communication in out-of-coverage scenarios supported by NR-V2X new features. We analyze the baseline algorithms possibly aimed for platoon communication based on the current 3GPP Release 16 and then develop an approach that overcomes the drawbacks of baselines. We further identify the deep reinforcement learning (DRL) algorithm as a potential enhancement due to the availability of feedback in the platoon communication; i.e., the Platoon Lead (PL) obtains acknowledgments from Platoon Members (PM) and takes a series of actions (resource scheduling) to improve communication efficiency (packet delivery ratio and average scheduled delay). A Monte Carlo simulator is employed to verify the analytical model's results and compare results between the discussed approaches.

Downlink Multi-User MIMO in IEEE 802.11ax. IEEE 802.11ax (Wi-Fi 6) marked a significant evolution milestone via the introduction of Multi-User (MU) communication modes (in contrast with legacy Single-User (SU) communication) for both Uplink (UL) and Downlink (DL) in tri-band (2.4/5/6 GHz) [9]. For the Uplink, this implies the use of trigger-based OFDMA; in this article, we focus solely on DL Multi-User (MU) Multiple Input Multiple Output (MU-MIMO). Legacy Single-User MIMO (SU-MIMO) - the precursor to MU-MIMO - laid the groundwork by allowing transmission of multiple spatial streams from an access point (AP) equipped with multiple antennas to a single client device on downlink. With the proliferation of wireless client devices, a single Wi-Fi network access point (AP) can have multiple associated stations (STAs) [10, 11]. With multi-antenna clients [1], it is feasible via DL Transmit Beamforming (TxBF) at the AP to send multiple streams to multiple STAs simultaneously (DL MU-MIMO).

A typical configuration [12, 13] such as Fig. 1.1 assumes an 8 x 8 AP (e.g., NetGear RAXE500) and 2 x 2 STAs (e.g., iPhone 15 and MacBook Air), implying that a single downlink transmission opportunity can potentially send a total of 8 spatial streams [2] to a selected sub-set of clients, e.g. each 2 streams to each selected four STAs. While DL SU-MIMO results in scaling of per-user throughput as a result of multi-stream transmission, its benefits are limited by the fact that most clients support either 1 or 2 spatial streams (i.e., a total of 2-stream transmissions in DL SU-MIMO in Fig. 1.1). By contrast, it is evident that in dense overlapped network scenarios - such as the enterprise or residential cluster - DL MU-MIMO provides a natural pathway to increasing network efficiency (aggregate network throughput) by *enabling simultaneous transmissions of multiple streams to multiple clients* (i.e., a total of 8-stream transmissions in DL MU-MIMO in Fig. 1.1), with appropriate choice of the user sub-set and TxBF to minimize inter-user/inter-stream interference.

Despite the promise of MU-MIMO for improved network capacity via simultaneous transmission to multiple users on downlink[3], real-world user testing has revealed significant challenges. A noticeable discrepancy exists between the theoretical speeds advertised by man-

---

[1] However, the number of antennas at the AP always exceeds the number of antennas at a client.

[2] Note that Wi-Fi 5 (IEEE 802.11ac) included support for MU-MIMO but limited to 4 streams on only 5 GHz downlink operation; whereas Wi-Fi 6 supports up to 8-stream on 2.4/5/6 GHz uplink/downlink operations.

[3] There exists an analogous feature for the uplink: trigger-based OFDMA whereby a 20 MHz channel may be shared synchronously by multiple users. However, consideration of UL OFDMA is beyond the scope of this article.

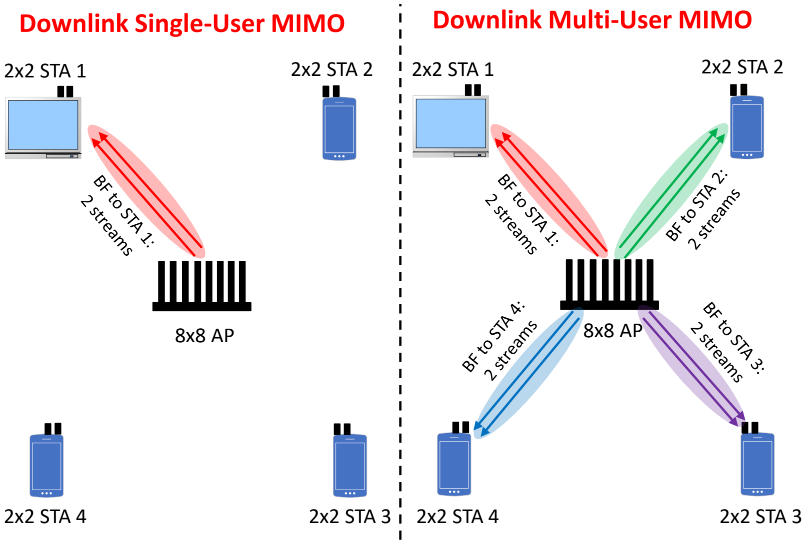

Figure 1.1: SU-MIMO vs MU-MIMO on Downlink Operations.

ufacturers who incorporate DL MU-MIMO and the actual throughput measured in specific conditions [14–16]. The primary purpose of this work is therefore to provide *new insights underlying the fundamental question*: “**when should DL MU-MIMO be turned on/off**” as a function of the operational scenario.

1.2 Summary of Research Contributions

In [17], the primary contribution of this work is a complete analytical model for MAC collision events for C-V2X mode 2, which is used to derive the PRR. Our model accounts for all key MAC parameters present in V2X mode 2, including the resource-keeping probability, the number of duplicate transmissions, and the proportion of available PRBs for reselection. We investigate the effects of these MAC parameters on PRR and on a set of intermediate performance metrics such as the probability of collision or the number of available resources. To validate our model, we provide results based on ns-3-based V2X simulation that corroborates our analysis. In [18], we analyze the baseline resource allocation approaches (Semi-persistent scheduling (SPS) described in 3GPP and Random Selection (RS)) for platoon communication, and determine that RS cannot outperform SPS no matter the resource-keeping probability set in the SPS-based broadcast environment. Thereafter, we propose an improved random selection (IRS) and find that IRS significantly mitigates packet collision from hidden terminal effects. We finally propose to employ a deep reinforcement learning algorithm, i.e., Deep Deterministic Policy Gradient (DDPG), to explore the impact of inter-vehicle collaboration further to decrease the collision probability based on local information. Our work reveals that DDPG is less sensitive than the IRS in terms of the change of resource-keeping probability in the environment, and the average scheduled delay with DDPG is also reduced compared with the IRS. In [19], we provides new insights about the key underlying factors (i.e., CSI overhead and spatial correlation) that have resulted in AP vendors turning off the DL MU-MIMO feature as the default setting in their products. Based on our study and analysis, guidelines as a function of operational scenarios is provided to address the fundamental question "when DL MU-MIMO should be turned on/off" for current/next-generation Wi-Fi systems. By a combination of analysis and computation/simulation, we attempt to answer the above question by (1) Identifying set of conditions where DL SU-MIMO outperforms MU-MIMO and vice-versa; and (2) Providing broad 'rules of thumb' regarding use of DL MU-MIMO in current/future Wi-Fi systems.

1.3 Thesis Outline

The remainder of this thesis is organized as follows. In Chapter 2 of this thesis, we describe the system setup and define the MAC collision events. Then we provide the analytical model for the defined collision events and PRR for some MAC parameters. Afterward, we update the model of collision probabilities and PRR to incorporate the number of duplicate transmissions. Finally, we describe and show results from the simulation regime used to validate the model. In Chapter 3 of this thesis, we analyze the performance of two baseline resource allocation approaches and the proposed IRS scheme in terms of the overall collision probability. Then a Deep Deterministic Policy Gradient framework is proposed to solve this resource allocation problem. Furthermore, we verify the analytical models of the baselines as well as the IRS scheme and then compare the performance between the baselines and the proposed algorithms from different perspectives. In Chapter 4 of this thesis, we first introduce the impact of Downlink Single-user (SU) and multi-user (MU) CSI overhead differences on their effective channel capacity; Then we explore the impact of spatial correlation on the MU channel capacity under the IEEE 802.11ax indoor channel model. Finally, a design guideline table for DL MU-MIMO is proposed by unifying the CSI overhead and the spatial correlation.

This thesis includes the material in the author's previous papers published on IEEE [17–39][4].

---

[4] In reference to IEEE copyrighted material which is used with permission in this thesis, the IEEE does not endorse any of University of Washington's products or services. Internal or personal use of this material is permitted. If interested in reprinting/republishing IEEE copyrighted material for advertising or promotional purposes or for creating new collective works for resale or redistribution, please go to http://www.ieee.org/publications_standards/publications/rights/rights_link.html to learn how to obtain a License from RightsLink.

Chapter 2

SEMI-PERSISTENT SCHEDULING IN NR SIDELINK MODE 2: MAC PACKET RECEPTION RATIO MODEL AND NS-3 VALIDATION

2.1 Motivation

In this work, we focus on analyzing broadcast NR SL mode 2 that uses SPS for basic safety/status messaging in C-V2X scenarios. A significant set of prior work analyzing SPS performance has been primarily based on simulations [35,40–49]. For instance, [41–43,50–52] proposed different simulation frameworks to study LTE/NR V2X. While a custom framework was developed in Matlab in [41], [42] and [43] built modules in Objective Modular Network Testbed in C++ (OMNeT++) and network Simulator 3 (ns-3), respectively. Both [44] and [45] used the simulation framework from [41] to explore the effects of varying the numerology and the physical (PHY)/MAC parameters on the Packet Reception Ratio (PRR) in V2X, respectively. In summary, none of these studies undertake any analytical modeling of SPS performance. A few efforts have been devoted to SL MAC and PHY analysis in recent years [53–59], exploring the impact of system parameters and network conditions on SL performance. For example, [53, 54] focused on the cross-layer (MAC + PHY) modeling of the C-V2X SPS in a vehicle platooning scenario. A novel discrete-time Markov chain (DTMC) approach was presented in [60] to calculate the average delay, collision probability and channel utilization in LTE SL mode 4. However, the proposed Markov-based SPS analysis incorporated only limited SPS parameters - the reselection counter and the selection window size. The authors in [55, 56] modeled the PRR and the access collision probability for LTE SL mode 4, respectively. However, they only focused on the legacy SPS protocol for LTE SL and failed to account for the new NR SL SPS features, such as the multiple packet transmission that significantly impacts the PRR. Meanwhile, most existing analytical models for the legacy SPS protocol may not provide insights into how SPS parameters relate to each other for determining the SL performance, such as PRR. However, understanding their mutual impacts is important for the performance enhancement of future beyond 5G (B5G) and 6G SL applications.

The primary contribution of this work is the *first* complete analytical model for C-V2X mode 2 MAC collision events, which is used to derive the PRR. Our model accounts for all key MAC parameters present in V2X mode 2, including the resource-keeping probability, the number of duplicate transmissions, and the proportion of available PRBs for reselection. We investigate the effects of these MAC parameters on PRR and on a set of intermediate performance metrics such as the Layer-2 packet collision probability or the number of available resources. Finally, we provide results based on ns-3 based V2X simulation that corroborates our analysis and provides independent simulation validation.

The rest of this chapter is organized as follows. Section II describes the system setup and defines the MAC collision events. Section III provides the analytical model for the defined collision events and PRR for some MAC parameters, while Section IV updates the model of collision probabilities and PRR to incorporate the number of duplicate transmissions. Section V then describes and shows results from the simulation regime used to validate the model.

2.2 System setup

Consider a typical SL mode 2 scenario where static UEs are randomly distributed in a local region such that the resulting network is fully connected. SL packet traffic sent from each UE is periodic, representing the Basic Safety Message (BSM) class, and uses the sensing-based Semi-Persistent Scheduling (SPS) defined in [2, 61] for channel access. An SL *resource pool*[1]

---

[1] A set of available time/frequency resources dedicated for SL TB transmissions.

comprised of a set of contiguous sub-channels[2] in the frequency domain and slots in the time domain, enables transmission of (data) Transport Block (TB) which, for our purposes, constitutes a single SL Layer-2 packet [62]. This combination of one sub-channel and one slot to transmit a TB is a Physical Resource Block (PRB) that constitutes the unit resource in sensing-based SPS. We assume a perfect PHY-layer as befits a pure MAC analysis, i.e., any Layer-2 packet sent from a source is received perfectly by all intended receivers if not interfered with due to simultaneous transmission(s) by other UE sources.

2.2.1 Sensing-based SPS: Recap

Sensing-based SPS [63, 64] is a distributed MAC protocol for NR SL that seeks to achieve collision avoidance based on predictive resource reservation by UEs over a resource reservation interval (RRI), T_{RRI}. A flowchart of the SPS procedure is shown in Fig. 2.1, which can be decomposed into two stages for purposes of understanding key aspects of protocol operation.

Stage 1: Sensing → Initial Selection. This is the initial stage where a reference UE performs sensing-based initial selection for subsequent resource reservation. A reference UE first determines the PRBs occupied by other UEs during the sensing window[3] via comparison to a reference signal received power (RSRP) threshold and then excludes those occupied PRBs for the subsequent reservation during selection window. The reference UE then **randomly** selects one among the remaining available PRBs in the selection window (for transmission of Layer-2 packet) and simultaneously chooses a *Reselection counter* $R_{c,init}$, implying reservation of the initially selected PRB for subsequent $R_{c,init}$ transmissions. $R_{c,init}$ is selected as independent and identically distributed (i.i.d.) random variable from the uniform distribution $U(5, 15)$ [4]. The counter is decremented by 1 after each T_{RRI}. An example is illustrated

---

[2] A subchannel is composed of a network maintainer configured number of resource blocks, which are in turn composed of 12 subcarriers whose bandwidth is defined by the subcarrier spacing.

[3] The sensing window covers one or multiple T_{RRI} defined in the 3GPP standard, depending on the upper layer setup.

[4] $R_{c,init}$ range varies if $T_{RRI} < 100$ ms but always satisfies $R_{c,init} \in U(5, 15)$ for $T_{RRI} \geq 100$ ms per the 3GPP standard. Since T_{RRI} is defined at the application layer, it is not the variable of interest

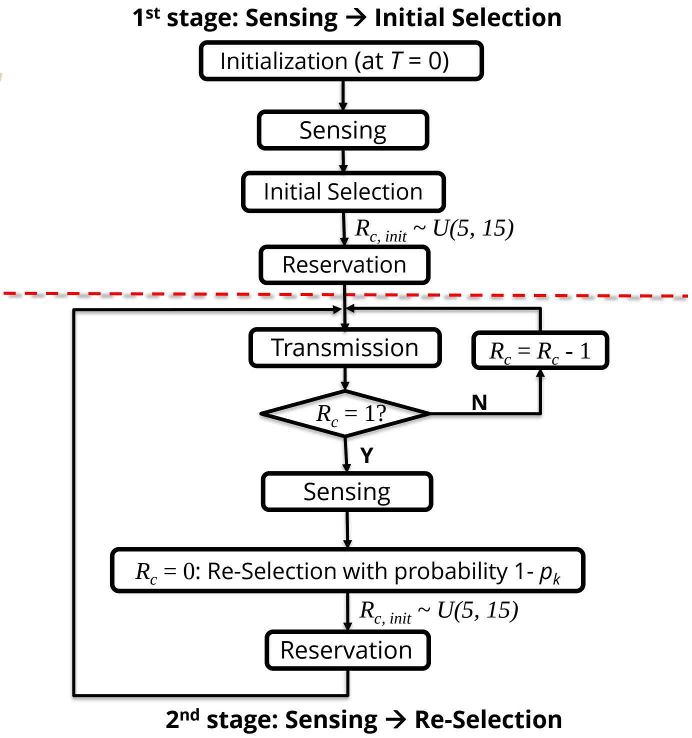

Figure 2.1: SPS MAC Procedure.

in Fig. 2.2.

Stage 2: Sensing → Reselection. In this stage, the reference UE starts packet transmissions, counts down the reselection counter until $R_c = 0$ and then enters reselection of PRBs:

- *Exclusion of occupied PRBs during the sensing window.*

  Since SL UEs are typically half-duplex (i.e., incapable of transmitting and receiving simultaneously), the reference UE cannot detect the RSRP of PRBs in the same slot when it transmits. Thus, in the sensing window for reselection, reference UE will exclude all ‘occupied’ PRBs due to not only exceeding the RSRP threshold but also

---

for the MAC-layer analysis. For simplicity, we consider the SL applications with $T_{RRI} \geq 100$ ms, thus $R_{c,init} \in U(5, 15)$ range always holds.

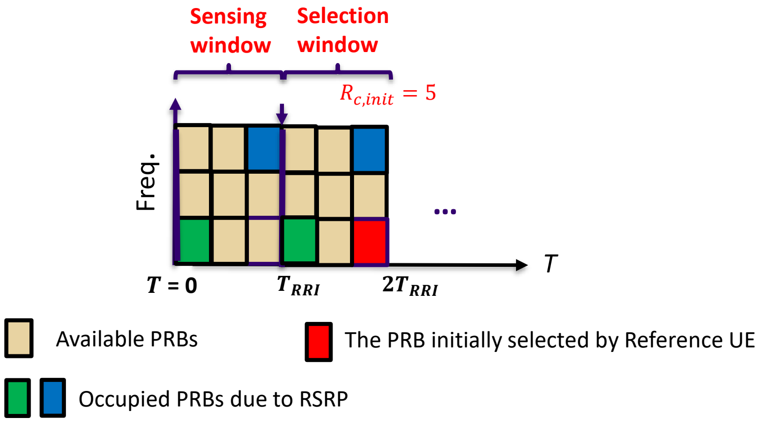

Figure 2.2: SPS Stage 1: Reference UE Case.

the half-duplex constraint.

- *Reselection.*
  When the reference UE's $R_c = 0$, it randomly **re-selects** one of the available PRBs with probability $1 - p_k$ during the selection window while persisting with the prior reserved PRB selection with probability p_k. $p_k \in [0, 0.8]$ is the *resource keeping* parameter specified in 3GPP standard and is identical for all UEs in the network. Such a reselection cycle is repeated in Stage 2 and is illustrated via example in Fig. 2.3. Since UE performs the process of sensing and initial selection only once during the 1^{st} stage while repeating the process of sensing and reselection during the 2^{nd} stage, the packet reception ratio (PRR) in the long term (i.e., the steady state) is determined by the 2^{nd} stage. We thereby develop the PRR model based on the events in the 2^{nd} stage.

The structure of the Sensing and Selection windows is shown in Fig. 2.4. Each UE reserves a PRB for a periodic packet transmission within T_{RRI}. For simplicity, the *Sensing*

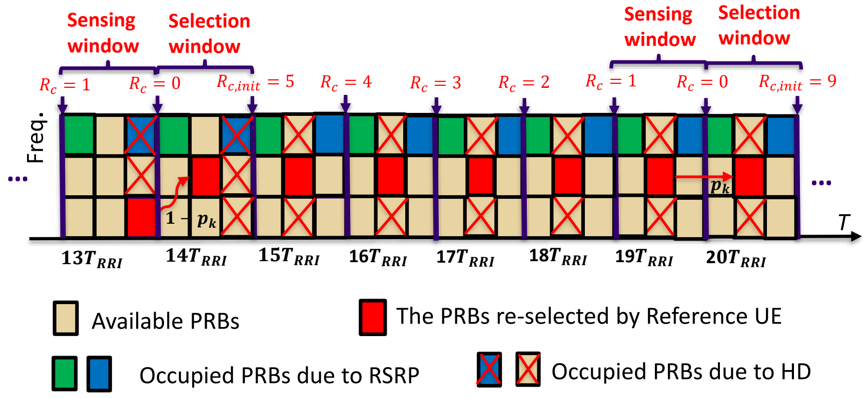

Figure 2.3: SPS Stage 2: Reference UE Case.

window covers the duration $[T_g - T_{RRI}, T_g]$ [5], where T_g is the packet generation instant at $R_c = 0$, followed by the *Selection window* over the duration $[T_g, T_g + T_{RRI}]$ [6]. If we denote the slot duration as t_s that depends on the numerology, the total number of slots within the sensing/selection window equals T_{RRI}/t_s and consequently, the total number of PRBs within the sensing/selection window is given by

$$N_r = \frac{T_{RRI} N_{sc}}{t_s}. \tag{2.1}$$

It should be noted the selection window size can range from 1 slot upto T_{RRI} according to the 3GPP standard. N_r can be readily adapted by replacing T_{RRI} in Eq. (3.5) with any selection window size from 1 slot to T_{RRI}. In this paper, however, we consider the selection window size to be T_{RRI}, which more adequately characterizes the collision events and key SPS parameters with their mutual impacts on the PRR model.

---

[5] Per the 3GPP standard, the sensing Window is defined as the duration $[T_g - T_{RRI}, T_g - T_0]$, where the processing time T_0 duration is typically equal to 1 or 2 slots, which is significantly smaller than T_{RRI} duration.

[6] In such a selection window, the access delay (the elapsed time from the instant packet generates to the instant it transmits) ranges from 1 slot to the maximum packet delay budget, i.e., T_{RRI}.

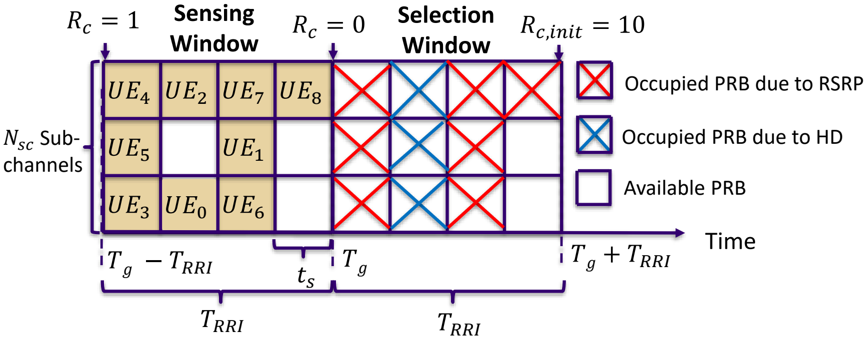

Figure 2.4: Sensing Window and Selection Window.

2.2.2 *MAC Collision Events in the Selection Window*

MAC collision happens when two (or more) UEs transmit in the same PRB, and all other UEs fail to decode any transmitted packets. Such a MAC collision event starts in a selection window and is followed by consecutive collisions at the next several RRIs. When reference UE 0's R_C decrements to 0, it enters the selection window and either performs reselection with probability $1 - p_k$, or does not with probability p_k. The MAC collisions in the selection window are thereby conditioned on whether UE 0 performs (or does not perform) reselection in the selection window, i.e.:

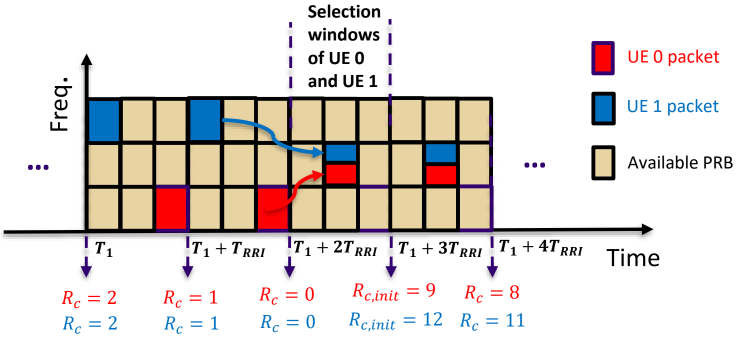

Figure 2.5: Collision Event 1.

Collision Event 1 - UE 0 performs reselection in the selection window and

collides with another UE that also performs reselection. In Fig. 2.5 we see when UE 0's R_c decrements to 0 at $T = T_1 + 2T_{RRI}$, UE 1's R_c also decrements to 0, indicating that both enter the selection window simultaneously. Each performs reselection by randomly and independently choosing one of 7 available PRBs out of $N_r = 9$ PRBs in the selection window during $[T_1 + 2T_{RRI}, T_1 + 3T_{RRI}]$. If two UEs select the same PRB, it leads to MAC collision in their overlapping selection window. At $T = T_1 + 3T_{RRI}$, $R^{UE0}_{c,init}(T) = 9$ while $R^{UE1}_{c,init}(T) = 12$, indicating that the PRB reselected by UE 0 and UE 1 in the selection window will be reserved for the following 9 RRIs and 12 RRIs, respectively. The number of consecutive collisions is thus $\min\left\{R^{UE0}_{c,init}(T), R^{UE1}_{c,init}(T)\right\}$. Since both $R^{UE0}_{c,init}(T)$ and $R^{UE1}_{c,init}(T) \in [5, 15]$, the number of consecutive collisions right after UE 0's selection window lies in the range [5, 15].

Collision Event 2 - UE 0 does not perform reselection in the selection window and continues to collide with a UE that it has previously collided with in prior RRIs. Collision Event 2 includes two collision sub-events that depend on the collided UE's R_c state at the moment UE 0's $R_c = 0$:

- **Sub-event 1 - Collided UE's $\boldsymbol{R_c = 0}$ when UE 0's $\boldsymbol{R_c = 0}$.** In Fig. 2.6(a) we see UE 0's R_c decrements to 0 at $T = T_1 + 2T_{RRI}$, meanwhile the collided UE 1 also decrements to 0. Then, both UEs do not perform reselection, indicating that both persist with the PRB reserved in the prior selection window to the current, i.e., over $[T_1 + 2T_{RRI}, T_1 + 3T_{RRI}]$. Since both UEs have collided with each other by reserving the same PRB in the prior RRIs, MAC collisions between UE 0 and UE 1 will continue in their overlapping selection window. The number of consecutive collisions right after UE 0's selection window under Collision Event 2 Sub-event 1 is still $\min\left\{R^{UE0}_{c,init}(T), R^{UE1}_{c,init}(T)\right\}$ which lies in the range [5, 15].

- **Sub-event 2 - Collided UE's $\boldsymbol{R_c \neq 0}$ when UE 0's $\boldsymbol{R_c = 0}$.** In Fig. 2.6(b) we see UE 0's R_c decrements to 0 at $T = T_1 + 2T_{RRI}$, meanwhile the collided UE 1's $R_c = 4$. In the UE 0's selection window during $[T_1 + 2T_{RRI}, T_1 + 3T_{RRI}]$, UE 0 does not perform reselection by sticking with the PRB reserved in the prior RRIs; meanwhile,

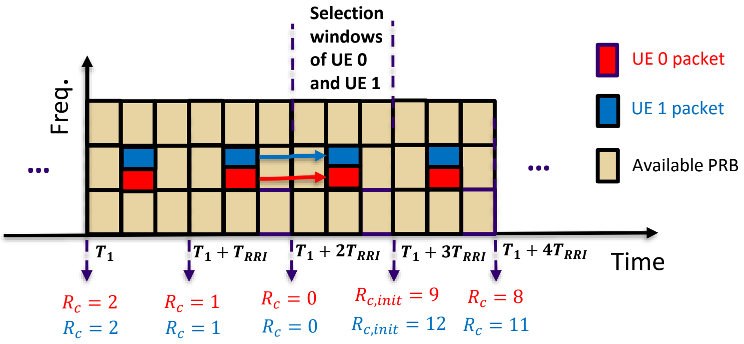

(a) Sub-Event 1

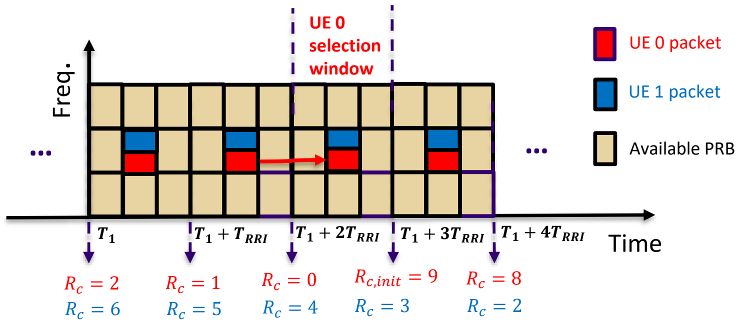

(b) Sub-Event 2

Figure 2.6: Collision Event 2.

UE 1 still uses the PRB reserved in the past RRIs to send packet because UE 1's R_c has not decremented to 0 yet. Since both UEs have collided with each other by reserving the same PRB in the RRIs prior to UE 0's selection window, MAC collisions will continue between UE 0 and UE 1 after UE 0's selection window. The number of consecutive collisions after UE 0's selection window under Collision Event 2 Sub-event 2 is $\min\left\{R_{c,init}^{UE0}(T), R_c^{UE1}(T)\right\}$. As $R_{c,init}^{UE0}(T) \in [5, 15]$ and $R_c^{UE1}(T) \in [0, 14]$, the number of consecutive collisions after UE 0's selection window under Collision Event 2 Sub-event 2 lies in the range $[0, 14]$.

Finally, note that if UE 0 does not suffer a collision in its selection window, no further

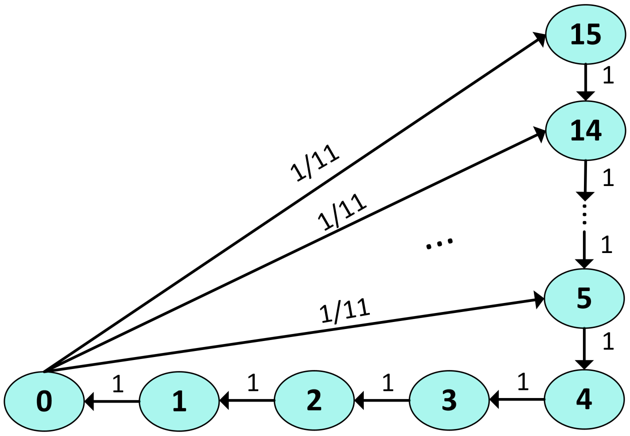

Figure 2.7: Reselection Counter (R_c) State Diagram.

collisions occur in the following $R_{c,init}^{UE0}$ RRIs after UE 0's selection window. Since the PRB selected by UE 0 in the selection window is reserved for the following $R_{c,init}^{UE0}$ RRIs, this occupied PRB must be excluded in the following $R_{c,init}^{UE0}$ RRIs for any UE that enters its selection window in this interval.

2.3 SPS PRR analytical model

As Sec. 2.2 shows, the collision of reference UE 0 in the selection window includes Collision Events 1 and 2. Let P_{COL} be the total probability of MAC collision, $P_{COL,1}$ as the probability for Collision Event 1, and $P_{COL,2}$ as the probability for Collision Event 2. Since Events 1 and 2 are mutually exclusive,

$$P_{COL} = P_{COL,1} + P_{COL,2}, \tag{2.2}$$

where $P_{COL,1}$ and $P_{COL,2}$ are analyzed in the following sections.

2.3.1 Performance Analysis - Reselection Counter State

Fig. 3.12 shows R_c state diagram for our SPS model, identical for all UEs. At any nT_{RRI}, the corresponding $R_c(nT_{RRI}) \in [0, 15]$. If $R_c(nT_{RRI}) = 0$, it is randomly re-initialized s.t.

$R_{c,init}((n+1)T_{RRI}) \in [5, 15]$. Thus, the probability that

$$\Pr\{R_{c,init}((n+1)T_{RRI}) = i | R_c(nT_{RRI}) = 0\} = \frac{1}{11}. \tag{2.3}$$

Denote π_i as the probability that $R_c(nT_{RRI}) = i, 0 \leq i \leq 15$. According to Fig. 3.12, π_i satisfies

$$\pi_i = \begin{cases} \pi_0 & \text{for } 0 \leq i \leq 4, \\ \frac{1}{11}\pi_0 + \pi_{i+1} & \text{for } 5 \leq i \leq 14, \\ \frac{1}{11}\pi_0 & \text{for } i = 15. \end{cases} \tag{2.4}$$

Using the normalization condition $\sum_{i=0}^{15} \pi_i = 1$, and solving (3.35), we obtain $\pi_0 = \frac{1}{11}$. Notice that the proposed R_c state diagram in Fig. 3.12 can be easily extended to cover different $R_{c,init}$ ranges for $T_{RRI} < 100$ ms, if necessary, which leads to a moderate revision in Eq. (3.35) following a similar calculation manner. Since investigating the impact of the $R_{c,init}$ range is not the focus in this paper, using $R_{c,init} \in [5, 15]$ for $T_{RRI} \geq 100$ ms is used for model simplicity.

We consider asynchronous R_c decrement whereby UEs' R_c counters follow independent clocks. Therefore, UEs' selection windows will partially overlap (when their R_c decrement to 0) within an T_{RRI}. Fig. 2.8 shows a two-UE example for asynchronous R_c decrement, where UE 0's selection window spans two consecutive RRIs of UE 1, either of which may be UE 1's selection window. Note that since the probability that any UE 1 RRI is its selection window equals π_0, the probability that UE 0's selection window partially overlaps with UE 1's is $2\pi_0$.

2.3.2 Performance Analysis - Collision Event 1

Collision Event 1 happens if at least one of the other UEs also selects the same available PRB as UE 0 (reference UE). Thus, Collision Event 1 is triggered by the reselection behavior of multiple UEs in the overlapping selection window. Suppose UE 0's $R_c = 0$ at time T and

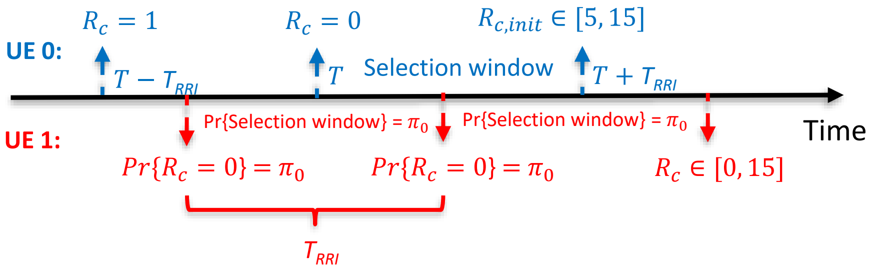

Figure 2.8: Asynchronous R_c Decrement.

UE 0 then performs reselection in its selection window during $[T, T + T_{RRI}]$. If another UE among N_{UE} UEs participates in reselection during $[T - T_{RRI}, T + T_{RRI}]$, its R_c should first decrement to 0 during $[T - T_{RRI}, T + T_{RRI}]$ (whose probability is $2\pi_0$), and then this UE performs reselection with probability $1 - p_k$. As each UE's R_c state is independent, if any n out of total N_{UE} UEs participate in reselection during $[T - T_{RRI}, T + T_{RRI}]$, the corresponding probability follows the binomial distribution, given by

$$\begin{aligned} &\Pr\{n \text{ UEs } R_c = 0, \text{Reselection} | R_c^{UE0} = 0, \text{Reselection}\} \\ &= P_s(n) = \binom{N_{UE}}{n} \Big(2\pi_0(1 - p_k)\Big)^n \Big(1 - 2\pi_0(1 - p_k)\Big)^{N_{UE}-n}. \end{aligned} \tag{2.5}$$

The UE 0 and n UEs then randomly reselect one of the available (unoccupied) PRBs in the overlapping selection window. The collision occurs if at least one of these n UEs selects the same available (unoccupied) PRB as UE 0. We define such a collision due to n-UE participating in reselection in the overlapping selection window as ***n*-fold collision**. Note that the number of available PRBs in the selection window N_a depends on the total number of PRBs in the selection window N_r and the number of occupied PRBs in the selection window N_o, i.e.,

$$N_a = N_r - N_o, \tag{2.6}$$

where both N_a and N_o are random variables. Since each UE with a packet to send needs to select a PRB in each RRI (including the selection window), N_{UE} UEs will occupy N_{UE}

PRBs in each RRI if no collision happens (i.e., $N_o = N_{UE}$, a fixed number). However, in the event of collisions, $N_o < N_{UE}$ is a random variable. The average number of occupied PRBs $\overline{N_o}$ in the selection window can be expressed in terms of the total MAC collision probability,

$$\overline{N_o} = N_{UE} - P_{COL}N_{UE} + \frac{P_{COL}N_{UE}}{\overline{N_c}}, \tag{2.7}$$

where P_{COL} is the total MAC collision probability (Collision Event 1 + Collision Event 2) to be determined, and the random variable $N_c \geq 2$ is the number of UEs in an occupied PRB where the collision happens. In Eq. (2.7), $P_{COL}N_{UE}$ represents the average number of UEs who collide with other UEs in the selection window. Thus $\frac{P_{COL}N_{UE}}{\overline{N_c}}$ represents the average number of occupied PRBs where collisions happen in the selection window, while $N_{UE} - P_{COL}N_{UE}$ represents the average number of occupied PRBs where collisions do not happen in the selection window. As Eq. (2.7) suggests, $\overline{N_o}$ will decrease if $\overline{N_c}$ increases. Then the average number of available (unoccupied) PRBs in the selection window, $\overline{N_a}$, is given by

$$\overline{N_a} = N_r - \overline{N_o} = N_r - N_{UE} + \frac{(\overline{N_c} - 1)P_{COL}N_{UE}}{\overline{N_c}}. \tag{2.8}$$

Given $\overline{N_a}$ available (unoccupied) PRBs in the selection window, the probability that one of n UEs collides with UE 0 by reselecting the same available PRB is $1/\overline{N_a}$. As a result, the probability that n-fold collision happens (i.e., at least one of n UEs select the same PRB as UE 0) given that n UEs participate in reselection is

$$\begin{aligned} &\Pr\{n\text{-fold Collision}|n \text{ UEs } R_c = 0, \text{ Reselection}\} \\ &= P_r(n) = 1 - \left(1 - \frac{1}{\overline{N_a}}\right)^n. \end{aligned} \tag{2.9}$$

Therefore, the probability that n-fold collision happens given that UE 0 performs reselection in the selection window is $P_r(n)P_s(n)$. Considering all n ($1 \leq n \leq N_{UE}$), we can obtain the collision probability when UE 0 performs reselection in the selection window as:

$$\Pr\{\text{Collision}|R_c^{UE0} = 0, \text{ Reselection}\} = \sum_{n=1}^{N_{UE}} P_r(n)P_s(n). \tag{2.10}$$

Substituting Eq. (3.6) and (2.9) into Eq. (3.9), yields

$$\begin{aligned}&\Pr\{\text{Collision}|R_c^{UE0}=0,\text{ Reselection}\}\\&=1-\left(1-\frac{2\pi_0(1-p_k)}{\overline{N_a}}\right)^{N_{UE}}.\end{aligned}\tag{2.11}$$

$P_{COL,1}$ is thus expressed as

$$\begin{aligned}P_{COL,1}&=\Pr\{\text{UE 0 Reselection}|R_c^{UE0}=0\}\\&\quad\cdot\Pr\{\text{Collision}|R_c^{UE0}=0,\text{ Reselection}\}\\&=(1-p_k)\left[1-\left(1-\frac{2\pi_0(1-p_k)}{\overline{N_a}}\right)^{N_{UE}}\right],\end{aligned}\tag{2.12}$$

where $\overline{N_a}$ is given by Eq. (3.7). Note that for $p_k = 0$, $P_{COL} = P_{COL,1}$ from Eq. (2.2) and hence $P_{COL,1}$ can be directly determined by solving Eq. (3.7) and (2.12) simultaneously. However for $p_k > 0$, $P_{COL,1}$ cannot be directly determined yet because $P_{COL,1}$ is a function of $P_{COL,2}$. Meanwhile, according to Eq. (2.12), $P_{COL,1}$ decreases as $\overline{N_a}$ increases, and hence from Eq. (3.7), $P_{COL,1}$ will decrease as $\overline{N_c}$ increases.

2.3.3 Performance Analysis - Collision Event 2

Collision Event 2 happens if UE 0 has collided with at least one of the other UEs in UE 0's most recent selection window, and collision will continue in UE 0's current selection window if both UE 0 and the collided UE(s) do not change the PRB after UE 0's most recent selection window. Similar to Collision Event 1 potentially involving multiple (> 2) packets/UEs as indicated by Eq. (2.9) resulting in n-fold collision, Collision Event 2 may also involve multiple packets/UEs. For instance, if $n = 10$, ten other UEs participate in reselection within the overlapping selection window as UE 0, the number of collided packets/UEs in a collision N_c can be up to 10. However, Fig. 2.9 shows that the 2-packet/UE collision (i.e., $N_c = 2$) probability dominates for all N_{UE}, as observed from data gathered through ns-3 simulations, especially in under-saturated condition. Since our analytical model is aimed at the under-

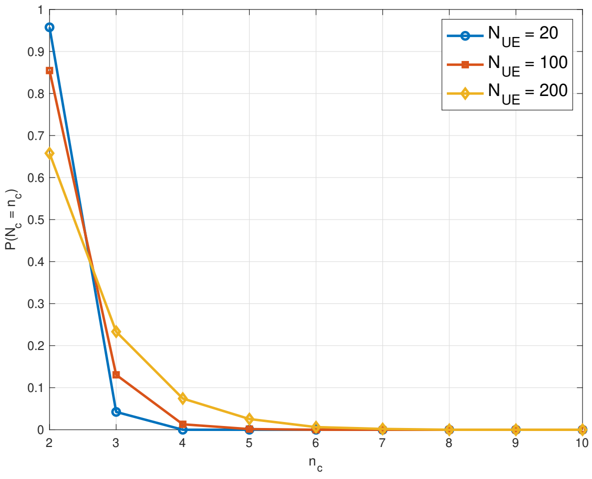

Figure 2.9: The Proportion of n_c-Packet Collision at Different N_{UE}.

saturated condition, we hereafter assume that only the 2-packet/UE collisions constitute Collision Event 2 to simplify the analytical model, as shown in Fig. 2.10.

Since Collision Event 2 occurs conditioned on the events in UE 0's *most recent* previous selection window during $[T_1, T_1 + T_{RRI}]$, as represented by the following event sets:

- $E1 = \Big\{\text{Collision during } [T_1, T_1 + T_{RRI}], \text{and } R_{c,init}^{UE0} = R_c^{UE1} \text{ at } T = T_1 + T_{RRI}\Big\}$, shown in Fig. 2.10(a). Then $R_c^{UE0} = R_c^{UE1} = 0$ at the beginning of UE 0's current selection window, and collision will continue into UE 0's current selection window if both UEs do not perform reselection (with probability $= p_k^2$). Since the probability that E_1 happens is given by:

$$\Pr\{E1\} = P_{COL} \cdot \Pr\{R_{c,init}^{UE0} = R_c^{UE1}\}, \tag{2.13}$$

where $\Pr\{R_{c,init}^{UE0} = R_c^{UE1}\} = \Pr\{R_c^{UE1} = 0 | R_c^{UE0} = 0\} = 2\pi_0$. Then, the probability that Collision Event 2 happens due to $E1$ is thereby derived as

$$P_{COL,2}^{E1} = \Pr\{\text{Collision}|E1\} \cdot \Pr\{E1\}. \tag{2.14}$$

where $\Pr\{\text{Collision}|E1\} = p_k^2$.

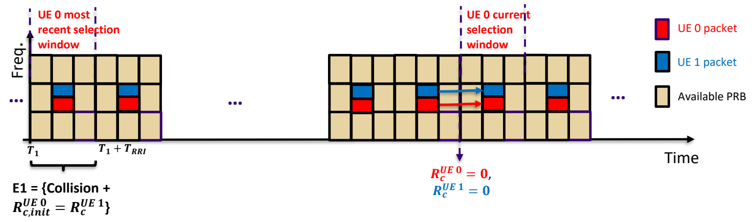

(a) Sub-event 1: E1 Followed by no Reselection of both UEs.

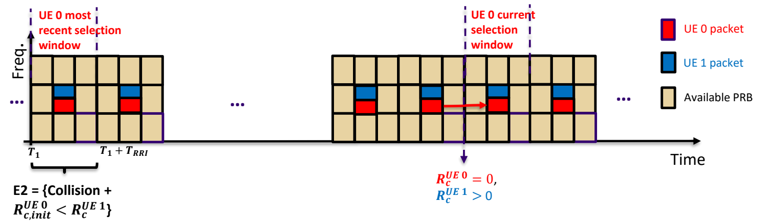

(b) Sub-event 2: E2 Followed by no Reselection of UE 0.

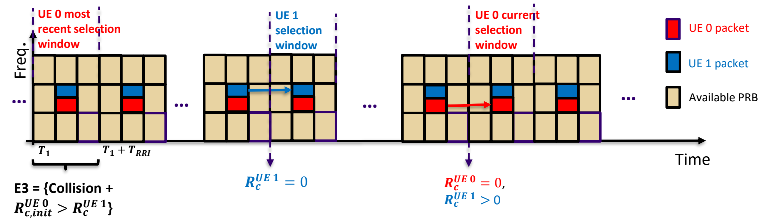

(c) Sub-event 2: E3 Followed by no Reselection of both UEs.

Figure 2.10: Events During $[T_1, T_1 + T_{RRI}]$ Followed by UEs' Behaviors that leading Collision Event 2.

- $E2 = \Big\{\text{Collision during } [T_1, T_1 + T_{RRI}], \text{and } R_{c,init}^{UE0} < R_c^{UE1} \text{ at } T = T_1 + T_{RRI}\Big\}$, shown in Fig. 2.10(b). Then $R_c^{UE0} = 0$ while $R_c^{UE1} > 0$ at the beginning of UE 0's current selection window, and collision will continue in the current reselection window if UE 0 does not perform reselection (with probability $= p_k$). The probability that E_2 happens is given by:

$$\begin{aligned} &\Pr\{E2\} = P_{COL} \cdot \Pr\{R_{c,init}^{UE0} < R_c^{UE1}\} = \\ &P_{COL} \cdot \sum_{|I|} \Big[\Pr\{R_{c,init}^{UE0} = i\} \cdot \Pr\{R_{c,init}^{UE0} < R_c^{UE1} | R_{c,init}^{UE0} = i\}\Big], \end{aligned} \tag{2.15}$$

where $i \in I = \{5, 6, ..., 15\}$ which is the set of all $R_{c,init}$ states, and $\Pr\{R_{c,init}^{UE0} < R_c^{UE1}\}$ can be obtained according to Fig. 3.12. Then, the probability that Collision Event 2 happens due to $E2$ is thereby derived as

$$P_{COL,2}^{E2} = \Pr\{\text{Collision}|E2\} \cdot \Pr\{E2\}, \tag{2.16}$$

where $\Pr\{\text{Collision}|E2\} = p_k$.

- $E3 = \Big\{\text{Collision during } [T_1, T_1{+}T_{RRI}], \text{and } R_{c,init}^{UE0} > R_c^{UE1} \text{ at } T = T_1{+}T_{RRI}\Big\}$, shown in Fig. 2.10(c). Then $R_c^{UE1} = 0$ and UE 1 does not perform reselection[7] (with probability $= p_k$) before UE 0's current selection window. Afterward, $R_c^{UE0} = 0$ while $R_c^{UE1} > 0$ at the beginning of UE 0's current selection window, and the collision will continue if UE 0 does not perform reselection (with probability $= p_k$). Then the probability that E_3 happens is given by:

  $$\begin{aligned}&\Pr\{E3\} = P_{COL} \cdot \Pr\{R_{c,init}^{UE0} > R_c^{UE1}\} = \\ &P_{COL} \cdot \sum_{|I|} \Big[\Pr\{R_{c,init}^{UE0} = i\} \cdot \Pr\{R_{c,init}^{UE0} > R_c^{UE1} | R_{c,init}^{UE0} = i\}\Big],\end{aligned} \tag{2.17}$$

  where $i \in I = \{5, 6, ..., 15\}$, and $\Pr\{R_{c,init}^{UE0} > R_c^{UE1}\}$ can be obtained according to Fig. 3.12. The probability that Collision Event 2 happens due to $E3$ is thereby derived as

  $$P_{COL,2}^{E3} = \Pr\{\text{Collision}|E3\} \cdot \Pr\{E3\}, \tag{2.18}$$

  where $\Pr\{\text{Collision}|E3\} = p_k^2$.

As $P_{COL,2}^{E1}$, $P_{COL,2}^{E2}$ and $P_{COL,2}^{E3}$ are mutually exclusive, $P_{COL,2}$ can be thereby finalized as:

$$P_{COL,2} = P_{COL,2}^{E1} + P_{COL,2}^{E2} + P_{COL,2}^{E3}. \tag{2.19}$$

---

[7] We ignore the second-order events and always assume that $R_{c,init}^{UE1} > R_c^{UE0}$ at the end of UE 1's selection window.

2.3.4 Performance Analysis - Packet Reception

The closed-form of MAC collision probability P_{COL}, is obtained by substituting Eq. (2.12) and (2.19) into (2.2), where P_{COL} can be numerically calculated by solving Eq. (3.7) and (2.20) simultaneously.

$$P_{COL} = \frac{(1-p_k)\left(1-\left(1-\frac{2\pi_0(1-p_k)}{N_a}\right)^{N_{UE}}\right)}{1-\left(2\pi_0 p_k^2+p_k \Pr\{R_{c,init}^{UE0}<R_c^{UE1}\}+p_k^2 \Pr\{R_{c,init}^{UE0}>R_c^{UE1}\}\right)}, \tag{2.20}$$

where the calculation of $\Pr\{R_{c,init}^{UE0} < R_c^{UE1}\}$ and $\Pr\{R_{c,init}^{UE0} > R_c^{UE1}\}$ are shown in Appendix 2.6.1 and 2.6.2, respectively. We further derive PRR - the probability that a packet is received successfully - which is determined by

- *MAC collision errors*, i.e., Two (or more) UEs transmit packets in the same PRB, and all receive UEs fail to decode those packets; this occurs with probability P_{COL};

- *Half-duplex (HD) errors.* These occur because UEs are assumed to be half-duplex devices, incapable of transmitting and receiving simultaneously. Thus, if a transmitter UE and a receiver UE transmit their packets in the same slot, the receiver UE cannot decode the packet from the transmitting UE. The probability that HD errors happen depends on the number of slots in each RRI, given by $P_{HD} = \frac{t_s}{T_{RRI}}$.

If a packet is successfully received, neither MAC collision errors nor HD errors must occur. Thus PRR is given by

$$PRR = (1 - P_{COL})(1 - P_{HD}). \tag{2.21}$$

2.4 Model Extension

2.4.1 Multiple Layer-2 Packet Transmissions per RRI

To improve the reliability of SL communication, the Packet Data Convergence Protocol (PDCP) duplication mechanism has been standardized in 3GPP [62], whereby a PDCP

$$P_{COL,1}(N_{Se},X) = (1-p_k)\left\{\left[1-\left(1+2\pi_0(1-p_k)\left(\left(1-\frac{1}{\overline{N_a}(N_{Se})}\right)^{N_{Se}}-1\right)\right)^{N_{UE}}\right]\cdot\frac{\overline{N_a}(N_{Se})}{XN_r}+1\cdot\frac{XN_r-\overline{N_a}(N_{Se})}{XN_r}\right\}, \tag{2.24}$$

$$P_{COL}(N_{Se},X) = \begin{cases} P_{COL}(N_{Se}) & \text{for } \overline{N_a}(N_{Se}) \geq XN_r, \\ \dfrac{(1-p_k)\left\{\left[1-\left(1+2\pi_0(1-p_k)\left(\left(1-\frac{1}{\overline{N_a}(N_{Se})}\right)^{N_{Se}}-1\right)\right)^{N_{UE}}\right]\cdot\frac{\overline{N_a}(N_{Se})}{XN_r}+1\cdot\frac{XN_r-\overline{N_a}(N_{Se})}{XN_r}\right\}}{1-\left(2\pi_0 p_k^2+p_k\Pr\{R_{c,init}^{UE0}<R_c^{UE1}\}+p_k^2\Pr\{R_{c,init}^{UE0}>R_c^{UE1}\}\right)} & \text{for } \overline{N_a}(N_{Se}) < XN_r. \end{cases} \tag{2.25}$$

Packet Data Unit (PDU) is duplicated into two (or more) instances and transmitted on two (or more) PRBs. In this section, we investigate the impact of multiple Layer-2 packet transmissions per RRI.

Since each UE now uses N_{Se} PRBs to transmit N_{Se} identical copies of the PDCP PDU in each RRI, N_{UE} UEs will require $N_{UE}N_{Se}$ PRBs in each RRI as the initial resource pool. Following the logic leading to Eq. (2.7), the resulting average number of occupied PRBs in the selection window $\overline{N_o}(N_{Se})$, becomes

$$\begin{aligned} &\overline{N_o}(N_{Se}) \\ &= N_{UE}N_{Se} - P_{COL}(N_{Se})N_{UE}N_{Se} + \frac{P_{COL}(N_{Se})N_{UE}N_{Se}}{\overline{N_c}(N_{Se})}. \end{aligned} \tag{2.22}$$

Then the average number of available (unoccupied) PRBs in the selection window, $\overline{N_a}(N_{Se})$, is given by

$$\begin{aligned} \overline{N_a}(N_{Se}) &= N_r - \overline{N_o}(N_{Se}) \\ &= N_r - N_{UE}N_{Se} + \frac{(\overline{N_c}(N_{Se})-1)P_{COL}(N_{Se})N_{UE}N_{Se}}{\overline{N_c}(N_{Se})}. \end{aligned} \tag{2.23}$$

In Collision Event 1, the probability that n-fold collision happens (i.e., at least one of nN_{Se} packets occupy the same PRB as UE 0) given that n UEs participate in reselection is

$$P_r(n,N_{se}) = 1-\left(1-\frac{1}{\overline{N_a}(N_{Se})}\right)^{nN_{Se}}. \tag{2.26}$$

Substitute Eq. (3.6) and (2.26) into (3.9), yielding:

$$\begin{aligned}&\Pr\{\text{Collision}|\text{UE } 0\ R_c = 0, \text{ Reselection}\}\\ &= 1 - \left(1 + 2\pi_0(1-p_k)\left(\left(1 - \frac{1}{\overline{N_a}}\right)^{N_{Se}} - 1\right)\right)^{N_{UE}}.\end{aligned} \tag{2.27}$$

From Eq. (2.2) and (2.27), $P_{COL,1}$ in terms of N_{Se} is expressed as

$$\begin{aligned}&P_{COL,1}(N_{Se}) =\\ &(1-p_k)\left[1 - \left(1 + 2\pi_0(1-p_k)\left(\left(1 - \frac{1}{\overline{N_a}(N_{Se})}\right)^{N_{Se}} - 1\right)\right)^{N_{UE}}\right],\end{aligned} \tag{2.28}$$

where $\overline{N_a}(N_{Se})$ is expressed in Eq. (2.23). Accordingly, $P_{COL,2}$ expressed in Eq. (2.19) is modified as follows

$$\begin{aligned}&P_{COL,2}(N_{Se}) = P_{COL}(N_{Se})\Big\{2\pi_0 p_k^2 + p_k \Pr\{R_{c,init}^{UE0} < R_c^{UE1}\} +\\ &p_k^2 \Pr\{R_{c,init}^{UE0} > R_c^{UE1}\}\Big\}.\end{aligned} \tag{2.29}$$

Then, the closed form of $P_{COL}(N_{Se})$ can be obtained by substituting Eq. (2.28) and (2.29) into Eq. (2.2):

$$P_{COL}(N_{Se}) = \frac{(1-p_k)\left[1 - \left(1 + 2\pi_0(1-p_k)\left(\left(1 - \frac{1}{\overline{N_a}(N_{Se})}\right)^{N_{Se}} - 1\right)\right)^{N_{UE}}\right]}{1 - \left(2\pi_0 p_k^2 + p_k \Pr\{R_{c,init}^{UE0} < R_c^{UE1}\} + p_k^2 \Pr\{R_{c,init}^{UE0} > R_c^{UE1}\}\right)}. \tag{2.30}$$

When $N_{Se} > 1$, a packet transmission is successful if at least one of N_{Se} duplicate packets is correctly decoded. Thus PRR in terms of N_{Se} is given by

$$PRR(N_{Se}) = 1 - \left[1 - \Big(1 - P_{COL}(N_{Se})\Big)(1 - P_{HD})\right]^{N_{Se}}. \tag{2.31}$$

where for $N_{Se} = 1$, $P_{COL}(1)$ in Eq. (2.30) and $PRR(1)$ in Eq. (2.31) defaults to P_{COL} in Eq. (2.20) and PRR in Eq. (2.21), as expected.

2.4.2 Proportion of available PRBs for reselection

Another option that possibly improves the SL communication reliability is increasing the minimum proportion of available PRBs for reselection characterized by the parameter X, whose range has been standardized in 3GPP [63,64]. In the previous sections, the proportion of available (unoccupied) PRBs for reselection was fixed at the lower limit, $X = 0.2$. In this section, we investigate the impact of (higher) X on $P_{COL}(X, N_{Se})$. We show that $P_{COL}(X, N_{Se})$ does not benefit from increasing X, although the number of available PRBs for reselection increases.

In the selection window, the number of available PRBs used for reselection must be first greater than a threshold (i.e., XN_r), which is the required minimum number of PRBs. UE randomly reselects among available PRBs for packet transmissions. In the previous sections, since X is set to a small value (e.g., $X = 0.2$), $\overline{N_a}(N_{Se})$, that represents the number of unoccupied PRBs (referred to as the available PRBs in the previous sections), satisfies $\overline{N_a}(N_{Se}) > XN_r$ in the under-saturated condition. However, $\overline{N_a}(N_{Se}) > XN_r$ may not hold if X is increased significantly: UE has to increase $\overline{N_a}(N_{Se})$ to XN_r by including $XN_r - \overline{N_a}(N_{Se})$ occupied PRBs in order to satisfy the minimum number requirement of total XN_r available PRBs for reselection. Thus, the XN_r available PRBs now include $\overline{N_a}(N_{Se})$ unoccupied PRBs and $XN_r - \overline{N_a}(N_{Se})$ occupied PRBs. In Collision Event 1, if $\overline{N_a}(N_{Se}) < XN_r$, two collision cases happen given that UE 0 performs reselection in the selection window:

- *Case 1*: UE 0 selects one of the $\overline{N_a}(N_{Se})$ unoccupied PRBs among XN_r available PRBs, and a collision happens if another UE reselects the same unoccupied PRB as UE 0;

- *Case 2*: Collision happens if UE 0 selects one of the $XN_r - \overline{N_a}(N_{Se})$ occupied PRBs among XN_r available PRBs.

Regarding Case 1, the probability that UE 0 selects one of the unoccupied PRBs among XN_r available PRBs is $\frac{\overline{N_a}(N_{Se})}{XN_r}$. Meanwhile, the probability that collision happens is expressed in Eq. (2.27); Regarding Case 2, the probability that UE 0 selects one of the occupied PRBs among XN_r PRBs is $\frac{XN_r - \overline{N_a}(N_{Se})}{XN_r}$, and the probability that collision happens is 1. Thus $P_{COL,1}(X, N_{Se})$ under $\overline{N_a}(N_{Se}) < XN_r$ is given by Eq. (2.24), where $\overline{N_a}(N_{Se})$ (that denotes the number of unoccupied PRBs in the selection window) is expressed in Eq. (2.23). Then, the closed form of $P_{COL}(N_{Se}, X)$ under $\overline{N_a}(N_{Se}) < XN_r$ can be obtained by substituting Eq. (2.24) and (2.29) into Eq. (2.2); meanwhile, $P_{COL}(N_{Se}, X) = P_{COL}(N_{Se})$ under $\overline{N_a}(N_{Se}) \geq XN_r$, where $P_{COL}(N_{Se})$ is given by Eq. (2.30). As a result, $P_{COL}(N_{Se}, X)$ is expressed in Eq. (2.25), where $\overline{N_a}(N_{Se})$ is expressed in Eq. (2.23). Accordingly, the PRR in terms of X is given by

$$PRR(N_{Se}, X) = 1 - \Big[1 - \Big(1 - P_{COL}(N_{Se}, X)\Big)(1 - P_{HD})\Big]^{N_{Se}}. \tag{2.32}$$

Meanwhile, the average number of available PRBs in the selection window, $\overline{N_a}(N_{Se}, X)$, is given by

$$\overline{N_a}(N_{Se}, X) = \begin{cases} \overline{N_a}(N_{Se}) & \text{for } \overline{N_a}(N_{Se}) \geq XN_r, \\ XN_r & \text{for } \overline{N_a}(N_{Se}) < XN_r, \end{cases} \tag{2.33}$$

where $\overline{N_a}(N_{Se})$ is given by Eq. (2.23).

2.5 Model Validation

2.5.1 Simulation Description

To validate the predicted performance for the asynchronous R_c decrementation based on our model, we resort to simulations using ns-3[8] by building off the 5G-LENA module as a base [30, 43][9]. The main parameters used during the ns-3 simulation can be found in Table 2.1.

Simulations were conducted for a linear topology with N_{UE} UEs in a single row separated by 1 meter, allowing them to transmit periodic safety messages according to the V2X mode

---

[8] Open source network simulator, available @ www.nsnam.org.

[9] All code used to generate both modeled and simulated curves can be found at https://github.com/CollinBrady1993/Code-for-NR-C-V2X-Tutorial.

Table 2.1: Main ns-3 Simulation Parameters

Parameter	**Value**	**Parameter**	**Value**
N_{sc}	2	P_t	23 dBm
t_s	1 ms	T_{RRI}	100 ms
γ_{SPS}	-110 dBm	N_{UE}	[20, 200]
p_k	[0, 0.8]	X	[0.2, 0.5]

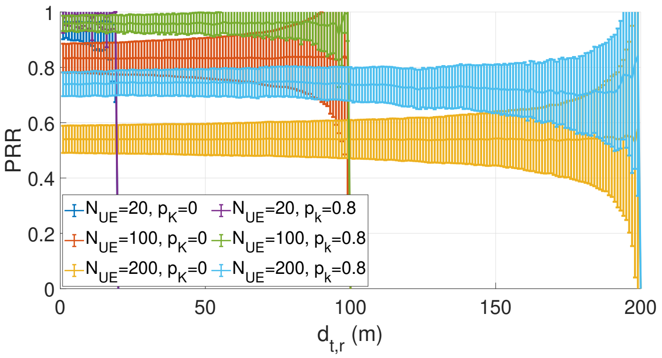

Figure 2.11: Simulated $PRR(d_{t,r})$ in the Fully Connected Network.

2 algorithm. Each simulation took place over the course of 100 seconds, the first 40 of which were excised to eliminate initialization effects for a total of 60 seconds of data. Each parameter set was repeated once with a new seed to ensure sufficient samples were taken to report data with high confidence. The only source of randomness in the simulation is the choice of PRB; thus a single, long simulation is sufficient to capture that randomness. ns-3 simulation runs produce traces of Physical Sidelink Control Channel (PSCCH) and Physical Sidelink Shared Channel (PSSCH) transmissions and receptions by all UEs (over slot and sub-channel used), that are post-processed to derive simulation estimates of P_{COL} and associated sub-events. This is achieved by observing instances of UEs using identical PRBs and tracing the channel's history to determine the type of collision. N_C is determined simultaneously as P_{COL} by counting the number of PSCCH/PSSCH transmissions in the

PRB during collisions. The PRR is derived by counting the number of successfully decoded PSSCH[10] transmissions. In the case of $N_{Se} > 1$, more than one successful duplicate PSSCH decode counts as one for the PRR calculation. N_a is derived from a separate trace from the SPS algorithm, which measures N_a directly during each reselection event for each UE. In addition to the previously mentioned metrics, we tested the PRR as a function of distance up to the largest N_{UE} tested (200 UEs result in 200 meters) to ensure the network was fully connected. Fig. 2.11 proves that PRR is uniform over all possible distances; thus, there is no dependence on distance. The ns-3 simulation was conducted on a PC running Ubuntu 20.04 with AMD Ryzen 9 3900X 12-Core Processor 3.79 GHz while the data processing and analytical models were implemented using Matlab R2023b.

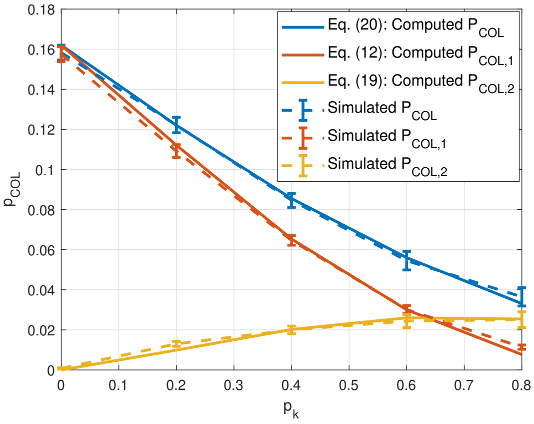

Figure 2.12: P_{COL} in terms of p_k: $N_{UE} = 100$.

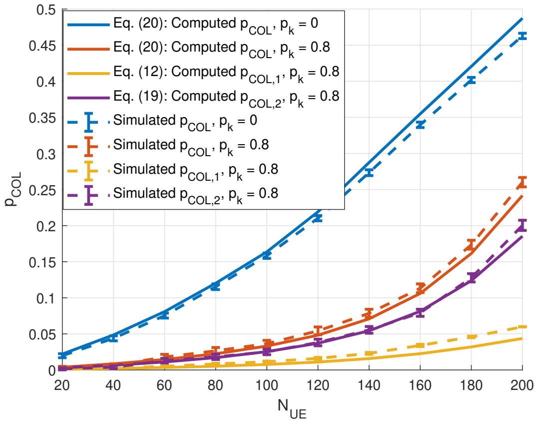

Figure 2.13: P_{COL} in terms of N_{UE}: $p_k = 0/0.8$.

2.5.2 *Validation Results*

P_{COL} vs p_k, fixed N_{UE} (Fig. 2.12): We observe that both P_{COL} and $P_{COL,1}$ monotonically decreases with p_k while $P_{COL,2}$ is monotonic increasing. The decrease of $P_{COL,1}$ can be

---

[10] In ns-3, a successful PSSCH decode requires the corresponding PSCCH to be decoded as well.

explained by Eq. (2.12): when p_k increases, UE 0 performs reselection less frequently in the selection window; meanwhile, the term $1-\left(1-\frac{2\pi_0(1-p_k)}{\overline{N_a}}\right)^{N_{UE}}$ also decreases, indicating that UE 0 is less likely to collide with other UEs given that UE 0 performs reselection in the selection window. Both effects cause $P_{COL,1}$ to decrease. The increase of $P_{COL,2}$ with p_k can be explained as follows: when p_k increases, UE 0 does not reselect more frequently in the selection window; meanwhile, if UE 0 collides with another UE in the selection window, their consecutive collisions last longer because they are more likely to stick with the previously reserved PRB. Since the decrease of $P_{COL,1}$ is much more significant than the increase of $P_{COL,2}$, P_{COL} thereby increases with p_k. Note that the cross-over point between $P_{COL,1}$ and $P_{COL,2}$ occurs at $p_k \approx 0.64$, it follows that Collision Event 1 happens more frequently than Collision Event 2 in most p_k cases (i.e., $p_k \in [0, 0.64]$). We conclude by remarking that the proposed models for P_{COL}, $P_{COL,1}$ and $P_{COL,2}$ matches well the ns-3 simulation results for a typical scenario ($N_{UE} = 100$).

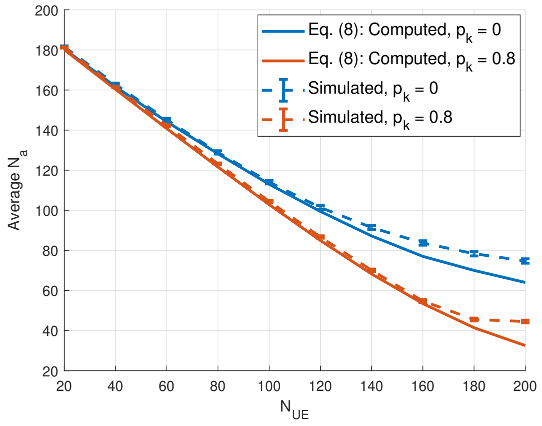

Figure 2.14: $\overline{N_a}$ in terms of N_{UE}: $p_k = 0/0.8$.

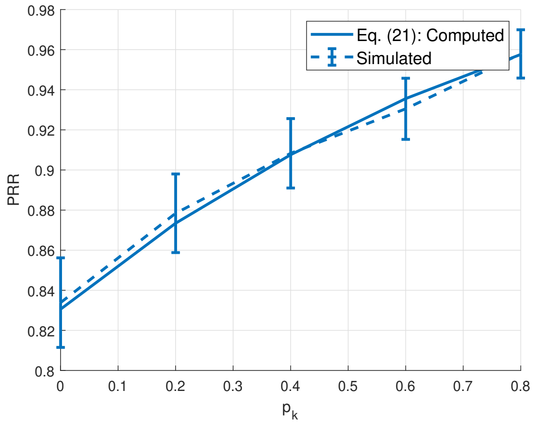

Figure 2.15: PRR in terms of p_K: $N_{UE} = 100$.

P_{COL} vs N_{UE}, varied p_k (Fig. 2.13): Next, the computed P_{COL}, $P_{COL,1}$ and $P_{COL,2}$ overall matches the simulated ones at different N_{UE}. Note that when $p_k = 0$, only Collision Event 1 happens, thus $P_{COL} = P_{COL,1}$. When N_{UE} goes up, both P_{COL} under two p_k go up. For $p_k = 0$, with increasing N_{UE}, more UEs participate in reselection, which leads P_{COL} to increase. Hence for $p_k = 0.8$ and higher N_{UE}, likelihood of Collision Event 2 (which dominates P_{COL}) is higher, which leads P_{COL} to increase. Compared with the simulation results, the analytical model subtly overestimates P_{COL} with $p_k = 0$ at $N_{UE} \geq 160$. This gap can be explained by the $\overline{N_a}$ difference shown in Fig. 2.14. The computed $\overline{N_a}$ is very close to the simulated values at low N_{UE}, however, the computed $\overline{N_a}$ deviates from the simulated one around $N_{UE} \geq 160$. The lower $\overline{N_a}$ indicates that each UE has fewer available PRBs for reselection, and two UEs are more likely to re-select the same available PRB. Therefore, the computed P_{COL} is overestimated compared to the simulated P_{COL} at high N_{UE}. Note that the total number of PRBs in each RRI is $N_r = 200$ while the channel moves to saturation for $N_{UE} \geq 160$. Thus, the proposed analytical model can accurately predict P_{COL} and $\overline{N_a}$ in an under-saturated condition while it becomes less accurate in a saturated condition ($N_{UE} \approx N_r$). This is due to PHY issues that must be incorporated into the analysis for better accuracy under the saturated condition. For instance, large numbers of UEs in a dense local network imply that their respective RSRPs at a receiver are closer in value. As a result, when the RSRP threshold is increased to include more available PRBs for reselection, the actual $\overline{N_a}$ might be higher than the computed $\overline{N_a}$ in a saturated condition, rendering the pure MAC analysis less accurate. Note that saturated channel assumption is impractical for SL communications operationally, because the significant PRR decrease will not satisfy the desired Quality of Service (QoS) requirements for critical BSMs or status messages.

$\underline{PRR \text{ vs } p_k\text{, fixed } N_{UE} \text{ (Fig. 2.15)}}$: At $N_{UE} = 100$ (an under-saturated case), the computed PRR matches quite well with the simulated one under different p_k, and PRR increases as p_k increases. $\underline{PRR \text{ vs } N_{UE}\text{, varied } p_k \text{ (Fig. 2.16)}}$: Meanwhile, the computed PRR also matches with the simulated one at different N_{UE}. Note that the computed PRR with $p_k = 0$ at high N_{UE} is subtly lower than the simulated one because the computed P_{COL} with $p_k = 0$ is overestimated at high N_{UE}.

$\underline{P_{COL}(N_{Se}) \text{ vs } N_{UE}\text{, fixed } p_k \text{ (Fig. 2.17)}}$: The computed $P_{COL}(N_{Se})$ overall matches with the simulated $P_{COL}(N_{Se})$ at different N_{UE}, especially in the under-saturated condition. As

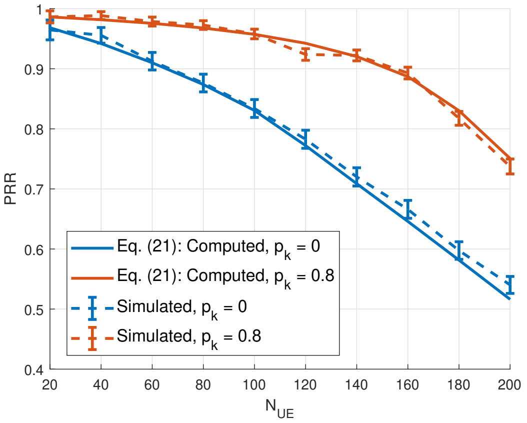

Figure 2.16: PRR in terms of N_{UE}: $p_k = 0/0.8$.

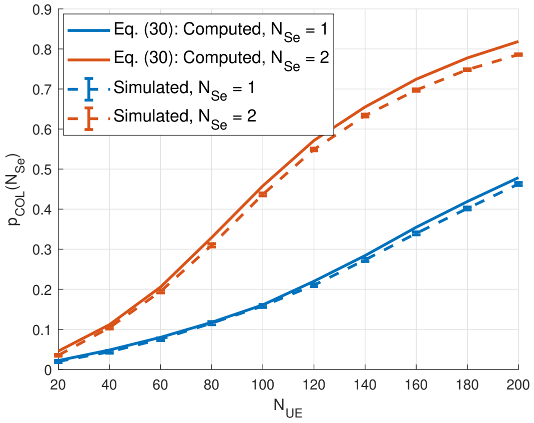

Figure 2.17: $P_{COL}(N_{Se})$ in terms of N_{UE}: $p_k = 0$.

expected, for a given P_{COL} (e.g., $P_{COL} = 0.1$), $N_{UE} \approx 80$ for $N_{Se} = 1$ is almost twice of $N_{UE} \approx 40$ for $N_{Se} = 2$. Meanwhile, at the lower N_{UE} (e.g., $N_{UE} = 60$), $P_{COL}(2)$ (≈ 0.2) is almost twice of $P_{COL}(1)$ (≈ 0.1). Also, it is clear that $P_{COL}(2)$ is always higher than $P_{COL}(1)$ for all N_{UE}.

$\underline{PRR(N_{Se}) \text{ vs } N_{UE}, \text{ fixed } p_k \text{ (Fig. 2.18)}}$: However, the $PRR(N_{Se})$ does not always follow the behavior of $P_{COL}(N_{Se})$ vs N_{UE}. For under-saturated condition, e.g., $N_{UE} \leq 80$, $PRR(2)$ is always higher than $PRR(1)$. Note that per Eq. (2.31), $PRR(N_{Se})$ is proportional to $1 - \Big(P_{COL}(N_{Se})\Big)^{N_{Se}}$ if P_{HD} is neglected (N_{Se} does not affect P_{HD}), where $\Big(P_{COL}(N_{Se})\Big)^{N_{Se}}$ represents the probability that all N_{Se} packets are not decoded. In the under-saturated condition, $N_{Se} = 2$ improves the packet reception gain because $P_{COL}(1) > \Big(P_{COL}(2)\Big)^2$. However, when $N_{UE} \geq 100$ (saturated scenario), $PRR(2)$ significantly dominates $PRR(1)$. Thus $PRR(N_{Se} = 2)$ degrades significantly due to $P_{COL}(1) < \Big(P_{COL}(2)\Big)^2$. Note that the cross-over value $(N^*_{UE}, PRR(N_{Se}, N^*_{UE}))$ represents the performance boundary in terms of N_{UE} and N_{Se}: $PRR(N_{Se}, N_{UE})$ benefits from the larger N_{Se} if $N_{UE} < N^*_{UE}$, and degrades if $N_{UE} > N^*_{UE}$. N^*_{UE} can be determined by solving $PRR(1, N^*_{UE}) = PRR(2, N^*_{UE})$.

$\underline{\overline{N_a}(N_{Se}) \text{ vs } N_{UE}, \text{ fixed } p_k \text{ (Fig. 2.19)}}$: The computed $\overline{N_a}(1)$ is close to the simulated

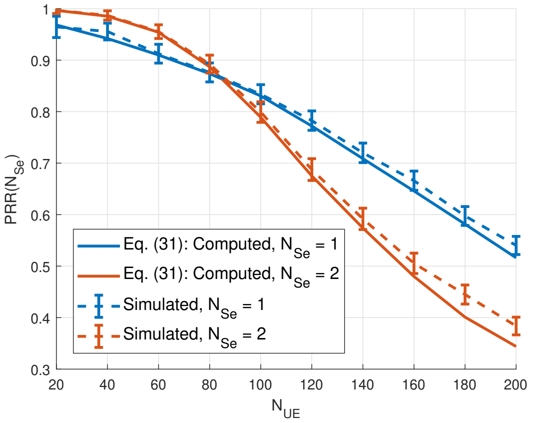

Figure 2.18: $PRR(N_{Se})$ in terms of N_{UE}: $p_k = 0$.

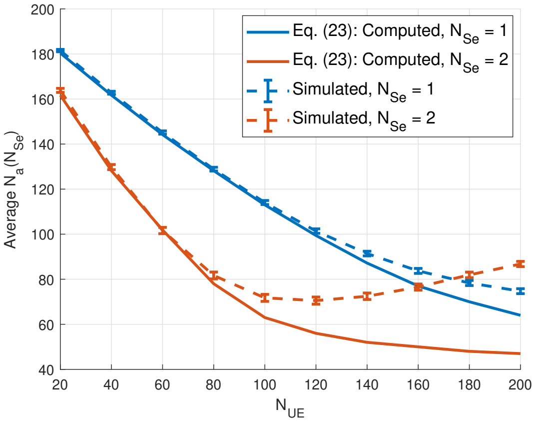

Figure 2.19: $\overline{N_a}(N_{Se})$ in terms of N_{UE}: $p_k = 0$.

value when $N_{UE} < 160$ while $\overline{N_a}(2)$ matches with the simulated when $N_{UE} < 100$ representing the under-saturated condition ($N_{UE} \leq 160$ for $N_{Se} = 1$ and $N_{UE} \leq 100$ for $N_{Se} = 2$). Thus, computed $\overline{N_a}(N_{Se})$ is accurately in the under-saturated condition. In addition, the $\overline{N_a}(N_{Se})$ difference for $N_{Se} = 2$ becomes quite large in the saturated condition. For instance, when $N_{UE} = 200$ and $N_{Se} = 2$, the number of packets transmitted in each RRI is $N_{UE}N_{Se} = 400$, which is twice the total number of PRBs in each RRI $N_r = 200$. It should be noted that the simulated $\overline{N_a}(N_{Se})$ goes up as N_{UE} increases in the saturated condition. This behavior occurs because the measured RSRP of each PRB becomes very close in the saturated condition, and some of the available PRBs for reselection become occupied. Increasing the RSRP threshold (e.g., 3dB granularity is increased each time) will include a burst of PRBs: the more the packets are transmitted in the saturated condition, the more the PRBs are included within each 3 dB granularity, and the higher the $\overline{N_a}(N_{Se})$ in the simulation is, which contradicts the fact in the model that more transmitted packets lead to the lower $\overline{N_a}(N_{Se})$. Thus, the pure MAC analysis becomes less accurate regarding $P_{COL}(N_{Se})$ and $PRR(N_{Se})$ in the saturated condition.

$\underline{P_{COL}(1, X) \text{ and } PRR(1, X) \text{ vs } N_{UE}, \text{ fixed } p_k \text{ (Fig. 2.20 and}}$

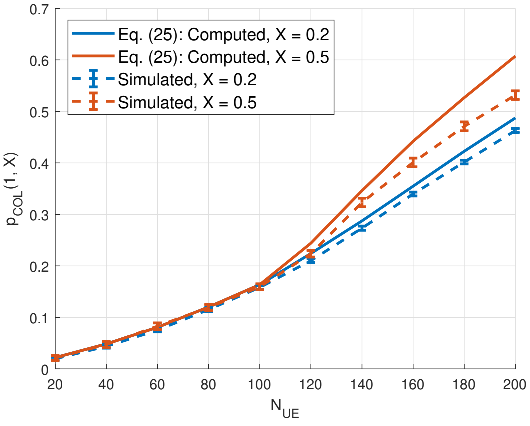

Figure 2.20: $P_{COL}(1, X)$ in terms of N_{UE}: $p_k = 0$.

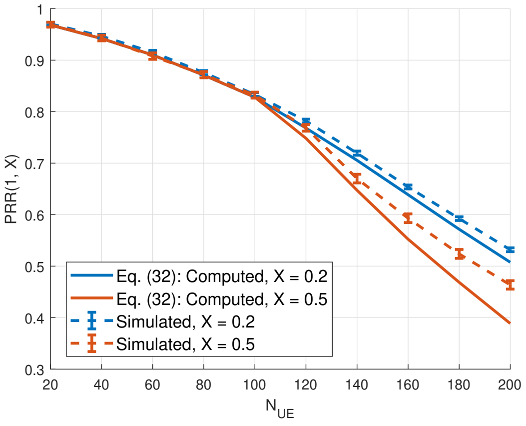

Figure 2.21: $PRR(1, X)$ in terms of N_{UE}: $p_k = 0$.

2.21): The computed $P_{COL}(1, X)$ and $PRR(1, X)$ are validated to predict well based on the simulated ones in the under-saturated channel condition. Meanwhile, $\overline{N_a}(1, X)$ in terms of N_{UE} is validated in Fig. 2.22. Note that, according to Eq. (2.33), the minimum $\overline{N_a}(1, 0.2) = 0.2 \cdot 200 = 40$ while the minimum $\overline{N_a}(1, 0.5) = 0.5 \cdot 200 = 100$. $\overline{N_a}(1)$ in both cases (only including unoccupied PRBs in available PRBs) must be the same if $\overline{N_a}(1) \geq 100$. Therefore, when $N_{UE} \leq 100$, indicating that $\overline{N_a}(1) \geq 100$, $P_{COL}(1, 0.5)$ (or $PRR(1, 0.5)$) should be the same as $P_{COL}(1, 0.2)$ (or $PRR(1, 0.2)$), which is validated in Fig. 2.20 (or Fig. 2.21). As N_{UE} further increases, meaning that $\overline{N_a}(1) < 100$, $\overline{N_a}(1, 0.5) = 100$ (including both unoccupied and occupied PRBs in available PRBs) remains fixed. By contrast, $\overline{N_a}(1, 0.2)$ keeps decreasing because $\overline{N_a}(1) > 40$ still holds (only including unoccupied PRBs in available PRBs). As a result, $P_{COL}(1, 0.5)$ (or $PRR(1, 0.5)$) is no longer the same as $P_{COL}(1, 0.2)$ (or $PRR(1, 0.2)$) in such cases.

2.6 Summary

In this chapter, we developed novel MAC collision models to thoroughly investigate the performance of the SPS protocol for 5G NR SL. Particularly, we defined the MAC collision

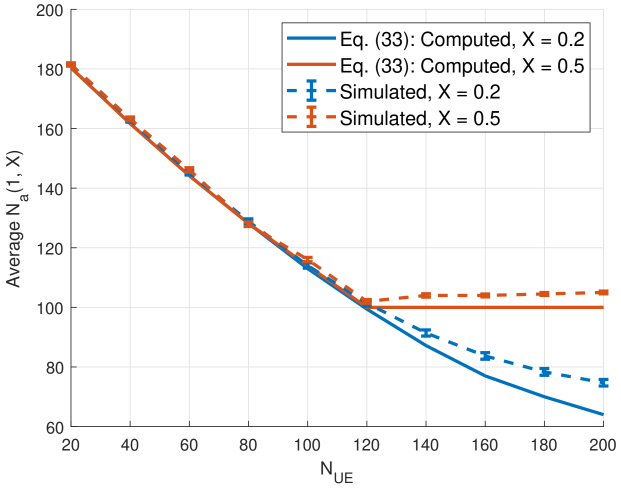

Figure 2.22: $\overline{N_a}(1, X)$ in terms of N_{UE}: $p_k = 0$.

events that accurately characterized the essence of MAC-based SPS. We also showed how the key SPS features relate to and further determine the MAC collision performance. The computed results were validated via simulations using the 5G-LENA module in ns-3. Through the extended analytical models, we illustrated that the MAC PRR benefits from the new feature - multiple Layer-2 packet transmission (N_{Se}) only in the under-saturated channel condition. Meanwhile, setting another feature - the minimum proportion of available PRBs for reselection (X) greater than 0.2 for the safety-related messages provides no benefit in any channel condition. Hence, we recommend that network engineers always set X to the minimum allowable value and 3GPP consider lowering the current lower limit of $X = 0.2$ for SL reliability enhancement.

As the proposed pure MAC-based model does not work well in the saturated channel condition due to PHY issues, future work will adapt the current model by incorporating relevant PHY parameters to address the above problem. In addition, it would be interesting to validate if the proposed NR mode 2 MAC PRR model is also compatible with the LTE mode 4 under the same SPS configurations.

Appendices

2.6.1 $Pr\{R_{c,init}^{UE0} < R_c^{UE1}\}$ *calculation*

According to Fig. 3.12 and Eq. (2.15),

$$
\begin{aligned}
&\Pr\{R_{c,init}^{UE0} < R_c^{UE1}\} \\
&= \sum_{|I|} \Pr\{R_{c,init}^{UE0} = i\} \cdot \Pr\{R_{c,init}^{UE0} < R_c^{UE1} | R_{c,init}^{UE0} = i\} \\
&= \Pr\{R_c^{UE1} = 0 | R_c^{UE0} = 0 \text{ during UE 0 most recent selection window}\} \\
&\cdot \Pr\{\ R_{c,init}^{UE1} > R_{c,init}^{UE0} \text{ during UE 0 most recent selection window}\} + \\
&\Pr\{R_c^{UE1} \neq 0 | R_c^{UE0} = 0 \text{ during UE 0 most recent selection window}\} \\
&\cdot \Pr\{\ R_{c,init}^{UE1} > R_{c,init}^{UE0} \text{ during UE 0 most recent selection window}\} \\
&= 2\pi_0 \frac{5}{11} + (1 - 2\pi_0)\Big(\frac{1}{11} \cdot \frac{5}{11} + \frac{1}{11} \cdot \frac{45}{121} + \frac{1}{11} \cdot \frac{36}{121} \frac{1}{11} \cdot \frac{28}{121} + \\
&\frac{1}{11} \cdot \frac{21}{121} + \frac{1}{11} \cdot \frac{15}{121} + \frac{1}{11} \cdot \frac{10}{121} \frac{1}{11} \cdot \frac{6}{121} + \frac{1}{11} \cdot \frac{3}{121} + \frac{1}{11} \cdot \frac{1}{121} + \\
&\frac{1}{11} \cdot \frac{0}{121}\Big) \\
&= 0.2892 \cdot 2\pi_0 + 0.1653.
\end{aligned}
\tag{2.34}
$$

2.6.2 $Pr\{R_{c,init}^{UE0} > R_c^{UE1}\}$ *calculation*

According to Fig. 3.12 and Eq. (2.17),

$$
\begin{aligned}
&\Pr\{R_{c,init}^{UE0} > R_c^{UE1}\} \\
&= \sum_{|I|} \Pr\{R_{c,init}^{UE0} = i\} \cdot \Pr\{R_{c,init}^{UE0} > R_c^{UE1} | R_{c,init}^{UE0} = i\} \\
&= \Pr\{R_c^{UE1} = 0 | R_c^{UE0} = 0 \text{ during UE 0's most recent selection window}\} \\
&\cdot \Pr\{\ R_{c,init}^{UE1} < R_{c,init}^{UE0} \text{ during UE 0's most recent selection window}\} + \\
&\Pr\{R_c^{UE1} \neq 0 | R_c^{UE0} = 0 \text{ during UE 0's most recent selection window}\} \\
&\cdot \Pr\{\ R_{c,init}^{UE1} < R_{c,init}^{UE0} \text{ during UE 0's most recent selection window}\} \\
&= 2\pi_0 \frac{5}{11} + (1 - 2\pi_0)\Big(\frac{1}{11} \cdot \frac{5}{11} + \frac{1}{11} \cdot \frac{6}{11} + \frac{1}{11} \cdot \frac{76}{121} + \frac{1}{11} \cdot \frac{85}{121} + \\
&\frac{1}{11} \cdot \frac{93}{121} + \frac{1}{11} \cdot \frac{100}{121} + \frac{1}{11} \cdot \frac{106}{121} + \frac{1}{11} \cdot \frac{111}{121} + \frac{1}{11} \cdot \frac{115}{121} + \frac{1}{11} \cdot \frac{118}{121} + \\
&\frac{1}{11} \cdot \frac{120}{121}\Big) \\
&= 0.7851 - 0.3306 \cdot 2\pi_0.
\end{aligned}
\tag{2.35}
$$

Chapter 3

RESOURCE ALLOCATION IN 5G PLATOON COMMUNICATION: MODELING, ANALYSIS AND OPTIMIZATION

3.1 Motivation

3.1.1 Related work

A comprehensive description of the NR V2X use cases and requirements is presented in the current 3GPP standard [65]. The use cases are divided into four groups: Vehicles Platooning, Advanced Driving, Extended Sensors, and Remote Driving. For each use case, 3GPP further distinguishes different degrees of automation following the SAE automation levels [66] ranging from 0 (no automation) to 5 (full automation). Typically, the higher the automation levels of a use case, the more stringent the NR V2X Quality of Service (QoS) requirements are. Particularly, vehicle platooning is one group of use cases that demands high QoS and reliability requirements. This group includes use cases for the dynamic formation and management of groups of vehicles in platoons.

Two potential technologies, i.e., dedicated short-range communications (DSRC) and cellular V2X (C-V2X) technologies, can be employed to enable inter-vehicle communications in vehicle platooning [67, 68]. The DSRC technology uses the IEEE 802.11p amendment of the legacy WiFi standard [69]. Due to its low cost, the DSRC technology has been well investigated for platoon communications [70–77]. Recently, much attention has been paid to the feasibility of utilizing the C-V2X technology for enabling inter-vehicle communications [78–84]. Cellular networks provide an off-the-shelf potential solution for inter-vehicle communications, which can make use of a high capacity, extensive cell coverage range, and widely deployed infrastructure [67]. However, the resource allocation algorithms in these works only apply to LTE-V2X, where the broadcast is regarded as the single vehicular communication type. With the introduction of new features supported by NR-V2X, the existing resource allocation algorithms aimed at vehicular communications may not fulfill the reliability requirement of platoon communication.

A set of recent studies investigated reliability enhancement for platoon communication. The authors in [85] proposed the sub-channel allocation and power control mechanism for LTE-based inter-vehicle communications to satisfy the requirement for the timely and successful delivery of inter-vehicle information within multi-platoons. In [86], the authors investigated a two-step sub-channel allocation strategy by which the base station and each platoon leader allocate the resources to improve multi-platoon cooperation. The literature [87] developed a group scheduling mechanism to overcome the cell border issues where the different base stations serve members of a long platoon. A joint systematic design of platoon communication and control was presented in [88] to reduce position errors of consecutive vehicles as well as improve platoon safety. However, most existing work focus on platoon communication within BS coverage for LTE; meanwhile, there is an insufficient study on the performance of platoon communication in the environment that the NR new feature supports.

Current literature [61,89–92] has presented many challenging aspects related to the standardized resource allocation algorithm aimed at the autonomous mode (i.e., Mode 2) in NR-V2X. In particular, due to decentralized behavior, the collision problem is one of the most stringent problems in the autonomous mode, which has been detected by many literature [26, 89, 93–96]. The autonomous mode is based on the sensing of the channel for the resource selection procedure. However, imperfect sensing can lead to the choice of radio resources already used by another vehicle, which can lead to packet collisions. Even if many existing proposals in the literature [93–96] tried to solve the collision problem in LTE-V2X, new efficient proposals are still needed. This challenge becomes more prominent in NR-V2X, prompting new features that LTE-V2X does not characterize. In addition, resource allocation efficiency is another challenge in NR-V2X in order to meet different V2X service requirements. However, there is a lack of research investigating resource allocation algorithms' efficiency on different V2X service requirements. It should be noted that the current 3GPP standard does not specify any specific resource allocation algorithm for platoon communication. With the coexistence of multiple vehicular communication types, if platoon communication still adopts the current standardized resource allocation algorithm, its performance may severely degrade due to interference from other vehicular communication types under the autonomous mode, which cannot meet the reliability requirement of platoon communication. Thus an efficient resource allocation algorithm is quite necessary to guarantee the basic service requirement of vehicle platooning in NR-V2X.

3.1.2 Contributions and Organization

This chapter investigates novel resource allocation approaches for platoon communication in the SPS-based broadcast environment without the assistance of a base station. The major contributions are summarized as follows.

- **We analyze the baseline resource allocation approaches (Semi-persistent scheduling (SPS) described in 3GPP and Random Selection (RS)) for platoon communication**, and determine that RS cannot outperform SPS no matter the resource keeping probability set in the SPS-based broadcast environment.

- **Thereafter, we propose an improved random selection (IRS)** and find that IRS significantly mitigates packet collision from hidden terminal effects.

- **We finally propose to employ a deep reinforcement learning algorithm, i.e., Deep Deterministic Policy Gradient (DDPG), to explore the impact of inter-vehicle collaboration further to decrease the collision probability based on local information**. Our work reveals that DDPG is less sensitive than the IRS in terms of the change of resource keeping probability in the environment, and the average scheduled delay with DDPG is also reduced compared with the IRS.

This chapter is organized as follows: Section 3.2 analyzes the performance of two baseline approaches and the proposed IRS scheme in terms of the overall collision probability. In Section 3.3, a Deep Deterministic Policy Gradient framework is proposed to solve this resource allocation problem. Section 3.4 verifies the analytical models of the baselines as well as the IRS scheme and then compares the performance between the baselines and the proposed algorithms from different perspectives. Finally, Section 3.5 draws the conclusions.

3.2 System model

3.2.1 Resource allocation in NR sidelink: Brief Recap

NR Rel-16 sidelink uses Cyclic-Prefix Orthogonal Frequency-Division Multiplexing (CP-OFDM) with scalable numerology to operate on frequency range 1 (FR1) - up to 6 GHz - or FR2 (24.25 - 52.6 GHz) [97–100].

The OFDM subcarrier spacing (SCS) varies with the numerology value μ [**?**] as shown in Fig. 3.1, given by $2^{\mu} \times 15$ kHz[1]. A slot is the smallest unit for scheduling sidelink transmissions, and the number of slots in a subframe (1 ms) varies accordingly with the slot duration given by $2^{-\mu}$ ms. In addition, the bandwidth part (BWP) concept has been introduced for NR-V2X [62], defined as a contiguous portion of resources in the frequency domain where single numerology is employed for all vehicles. The BWP thus consists of a set of physical resource blocks (PRBs) with the same SCS, determined by the numerology.

A subset of the available sidelink resources - called a resource pool [62]- is pre-configured for all vehicular communication types. A resource pool consists of slots (time resources) and BWP using common PRBs (frequency resources) for sidelink operation. In the frequency domain, the resource pool consists of several contiguous subchannels[2]. A subchannel represents the smallest frequency resource unit for transmission/reception, consisting of a group of consecutive PRBs in a slot that forms a resource block group (RBG), as shown in Fig.

---

[1] For NR V2X, μ can be set to 0, 1, 2 or 3 such that the SCS equals 15, 30, 60 or 120 kHz. In FR1, 15 kHz, 30 kHz, and 60 kHz are supported, while 60 kHz and 120 kHz are supported for the SCS in FR2.

[2] In NR-V2X sidelink, the subchannel size can be equal to 10, 12, 15, 20, 25, 50, 75, or 100 PRBs.

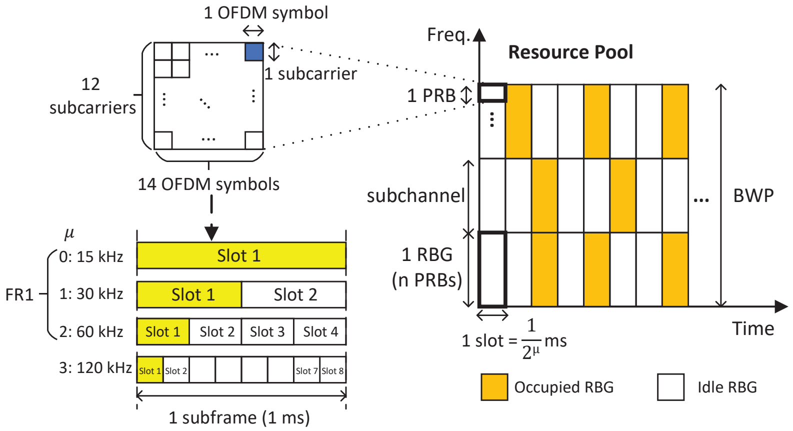

Figure 3.1: Resource pool for NR sidelink.

3.1. Note that each RBG can support a low-payload packet transmission [3].

In sidelink Mode 2, the vehicle autonomously selects resources from the pre-configured resource pool for transmission. The transmitter selects a suitable RBG with the help of sensing that monitors Sidelink Control Information (SCI) from all nearby transmitting UEs. Two-stage SCI was introduced in NR-V2X, whereby the content of the SCI payload is separated into two stages [62]. The 1st-stage SCI is mainly used for sensing, which contains information related to QoS priority of data, occupied resource blocks, resource reservation interval, etc. The 2nd-stage SCI transmission carries decoding information for the packet transmitted in Physical Sidelink Shared Channel (PSSCH).

3.2.2 Sensing-based Semi-Persistent Scheduling

Broadcast in NR sidelink Mode 2 adopts a distributed scheduling algorithm - sensing-based Semi-Persistent Scheduling (SPS) scheme [63, 64] - for collision avoidance. Each broadcast

---

[3] In this paper, the low-payload packet can be a Basic Safety Message (BSM) with the size of 190 or 300 bytes used for broadcast communication or the packet with a size of 50-500 bytes used in platoon communication.

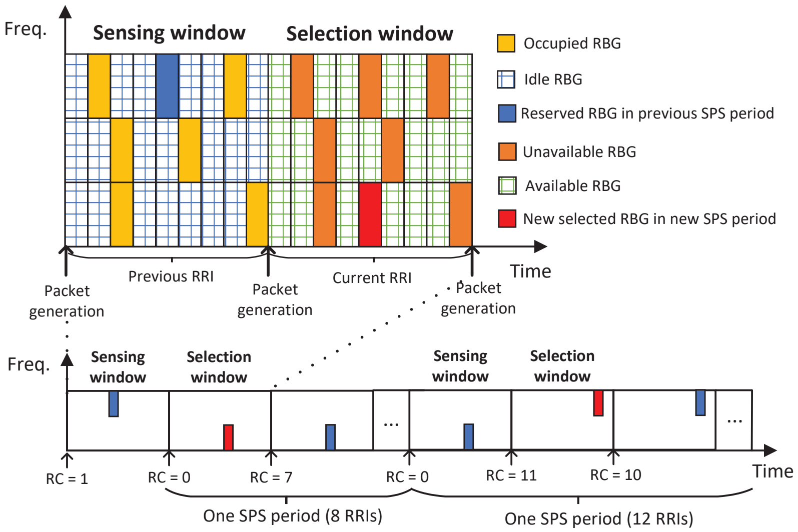

Figure 3.2: The general procedure of SPS scheme for broadcast communication.

vehicle is assumed to periodically generate a packet for transmission where the packet generation rate is the reciprocal of *Resource Reservation Interval (RRI)*. The general procedure of SPS is shown in Fig. 3.2. A vehicle randomly selects an available RBG within the selection window according to the results from the (prior) sensing window; it then reserves that RBG for a certain duration (one SPS period) for consecutive packet transmissions. Both the sensing and selection window start right after the packet generation instant, each with a duration of one RRI. Available RBGs in the selection window correspond to the RBGs determined idle in the sensing window [4]. The idle RBGs in the sensing window are determined as follows: 1) the first SCI whereby the vehicle learns which RBGs are occupied in the sensing window, and 2) the average Reference Signal Received Power (RSRP) of each RBG less than an RSRP threshold. The number of consecutive packet transmissions in an SPS period is determined by the *Re-selection Counter (RC)* randomly selected from 5 to 15, e.g., $RC = 8$ in Fig. 3.2. Each time a packet is transmitted using the reserved RBG, Re-selection

---

[4] The RBG which is reserved in the previous SPS period is also unavailable in the selection window.

Counter is decremented by 1. When Re-selection Counter expires (= 0), the vehicle enters the (next) sensing window cycle, and the Re-selection Counter is reset by selecting a new random value (e.g., $RC = 12$).

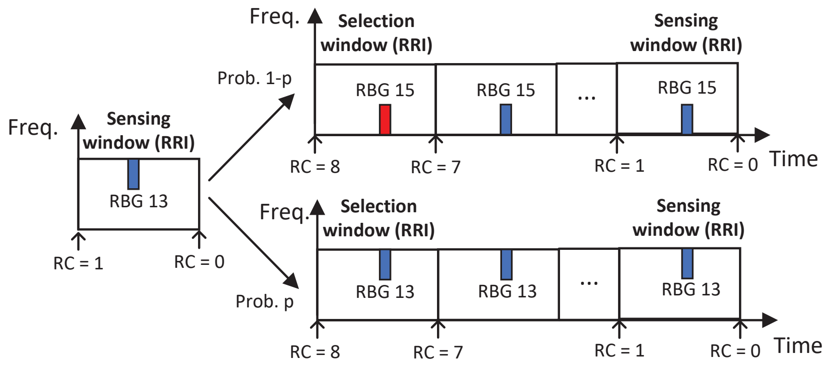

Figure 3.3: The choice of RBG in the selection window.

As Fig. 3.3 shows, each time the vehicle starts a new SPS period, it has two options for RBG selection within the selection window, depending on a resource keeping probability[5]. The vehicle randomly selects one of the available RBGs (e.g., RBG 15) within the selection window with probability $1 - p$; otherwise, it sticks with the previously reserved RBG (e.g., RBG 13). The vehicle then reserves the selected RBG for a whole SPS period containing the initial value of the Re-selection Counter's RRIs. The main notations and acronyms in this paper are summarized in Table 3.1 and 3.2, respectively.

3.2.3 System Architecture

Fig. 3.4 shows a finite length highway with M lanes consisting of a platoon system with length L_p (km) and other broadcast vehicles that share the same resource pool. Vehicles are assumed to be uniformly distributed in each lane with linear density ρ (vehicles/km). Since the width of each lane is much smaller than the vehicular communication range, the

---

[5] The value of resource keeping probability $p \in [0, 0.8]$ is not specified in the current standard.

Table 3.1: List of Key Notations

Notation	Definition
p	Resource keeping probability
π_0	Probability that a broadcast vehicle enters the selection window
P_c^B	Collision probability of broadcast communication
P_{rs}^{PL}	Collision probability due to PL's resource selection
P_{ht}^{PL}	Collision probability due to PL's hidden terminal effects under baselines
$P_{c,RS}^{PL}$	Overall collision probability of platoon communication under RS
$P_{c,SPS}^{PL}$	Overall collision probability of platoon communication under SPS
$P_{rs,IRS}^{PL}$	Collision probability due to PL's resource selection under IRS
$P_{ht,IRS}^{PL}$	Collision probability due to PL's hidden terminal effects under IRS
$P_{c,IRS}^{PL}$	Overall collision probability of platoon communication under IRS

2-dimensional scenario can be effectively modeled as (multiple) 1-dimensional lines with vehicles as point sources/destinations. All vehicles are pre-configured to have the same synchronized RRI duration. Meanwhile, the PL participates both in the platoon and non-platoon broadcast communication that are not coordinated. In addition, the number of RBGs in the resource pool has been pre-configured to be large enough so that those RBGs cannot be all occupied even under high vehicle density [6].

Following the guidelines in [2], the propagation channel for a vehicle (potential source-destination) pair can be classified as either a) Line-of-Sight (LOS) or b) Vehicle Non-Line-of-Sight (NLOS). The link pathloss is implemented by following the 3GPP specifications [2], given by

$$PL(d) = 32.4 + 20 \cdot \log_{10} d + 20 \cdot \log_{10} f_c [dB], \tag{3.1}$$

where d is the distance in meters and f_c is the center frequency in GHz. The expected radius

---

[6] Otherwise, none of the packets from broadcast vehicles or the PL can be successfully delivered whichever resource scheduling algorithm is applied because of no available (idle) RBG for selection. Such a case would be meaningless in a real V2X system.

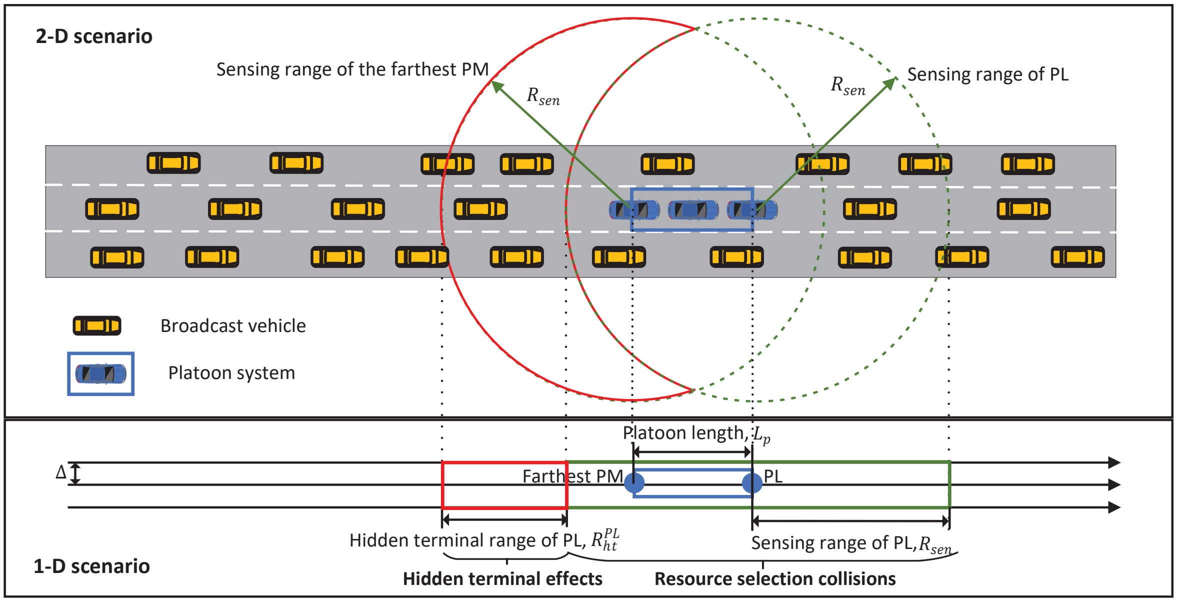

Figure 3.4: The 2-D to 1-D mapping for multi-lane highway scenario where multiple vehicular communication types coexist.

of sensing range [7] of each vehicle, R_{sen}, can be determined by [101]

$$R_{sen} = \frac{PL^{-1}(P_{TX} - SH - P_{sen})}{1000}, \tag{3.2}$$

where R_{sen} is expressed in kilometers. P_{TX} [8] is the transmit power of the transmitter (TX) vehicles, SH is the shadowing loss of the V2V link, and P_{sen} is the link sensitivity power level [9] and $PL^{-1}(\cdot)$ is the inverse function of Eq. (3.1). As Fig. 3.4 shows, the PL is able to detect a packet from the broadcast vehicle within the sensing range of the PL. In the 1-dimensional scenario, each lane is modeled by its center line separated from the next lane by distance delta Δ, i.e., the number of lanes within R_{sen} is approximately equal to R_{sen}/Δ,

---

[7] The sensing range is the maximum separation distance whereby a (receiving) vehicle is able to detect a packet from a (source) vehicle.

[8] The standard [101] specifies the maximum transmit power as 23dBm.

[9] The minimum power threshold or receiver sensitivity level specified in the standard is -91 dBm.

Table 3.2: List of Main Acronyms

RRI	Resource Reservation Interval
RBG	Resource Block Group
RC	Re-selection Counter
PL	Platoon Leader
PM	Platoon Member
SPS	Semi-Persistent Scheduling
RS	Random Selection
IRS	Improved Random Selection

where $\Delta << R_{sen}$. Since the number of lanes M is typically $<< R_{sen}/\Delta$, the sensing range for any lane is (approximately) the same. Thus the expected number of broadcast vehicles within the sensing range of PL with M lanes is given by

$$N_{sen}^{PL} = 2R_{sen}M\rho, \tag{3.3}$$

where ρ is the vehicle density (per unit kilometer.) in each lane.

The hidden terminal range of PL depends on the platoon length L_p [10], as depicted in Fig. 3.4. For the lane where the platoon is located, the expected hidden terminal range of PL, R_{ht}^{PL}, should equal the platoon length, i.e., $R_{ht}^{PL} = L_p$. Due to the small Δ in the 1-D scenario, the hidden terminal range of PL in neighboring lanes is assumed to be the same as the platoon lane. Hence the expected number of the hidden terminal (vehicles) for PL transmission to the end PM of the platoon is equal to

$$N_{ht}^{PL} = R_{ht}^{PL}M\rho = L_pM\rho. \tag{3.4}$$

We seek to model resource scheduling for platoon communication between the PL and PMs. Fig. 3.5 shows the RBG occupancy in PL's selection window and the corresponding

---

[10] We assume a platoon length which is close to R_{sen} for the analysis; for small platoon length, the MAC collision model is less accurate since a PM may still receive the packet from PL even in the event of simultaneous transmissions.

RBG occupancy from one of the PMs. Only the first six RBGs (indexed in PL's selection window) are used to investigate how PL's resource scheduling impacts the success of platoon broadcast communication. The factors leading to packet collision for platoon broadcast communication include the **resource selection induced collisions** and any **hidden terminal effects**. The **resource selection collisions** occur when at least one broadcast vehicle within the sensing range of PL selects the same available RBG as the PL [11]. Thus packet decoding failure is assumed to result at a PM that is within range of both PL and the broadcast vehicle due to simultaneous transmission using the same RBG - representing a MAC layer collision model.

The **hidden terminal effects** occur when at least one broadcast vehicle in the hidden terminal region of PL uses the same RBG as the PL. To investigate the hidden terminal effects, it suffices to consider the farthest PM (worst case) in the platoon as the intended receiver. For example, if one hidden vehicle has reserved RBG 1 for broadcast communication, if the PL also selects RBG 1 for platoon communication, the farthest PM cannot correctly receive the packets from both vehicles, resulting in a PHY collision. The hidden terminal collision can happen at any RRI of PL and is not limited to PL's selection window because neither the PL nor the hidden vehicles know their respective RBG selection. A successful delivery happens only if neither of the above conditions leading to packet collision are met, e.g., the PL selects RBG 2 in the selection window [12].

After each packet transmission from the PL for platoon communication, the PL waits for feedback from all PMs, consisting of an acknowledgment (ACK) or negative acknowledgment (NACK) if reception was successful(unsuccessful). This paper explores one-shot packet transmission from the PL to PMs, under the standard assumption that feedback is 100% reliable.

---

[11] For instance, both PL and another broadcast vehicle select RBG 5 simultaneously in the example in Fig. 3.5.

[12] Successful packet delivery for platoon communication is defined as a packet from PL being successfully broadcast to *all* PMs through groupcast mode.

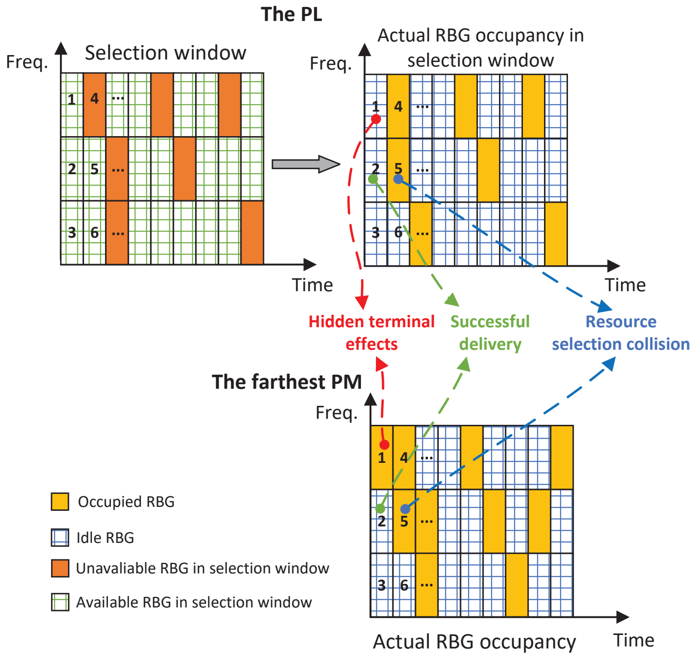

Figure 3.5: The actual RBG occupancy in PL's selection window.

3.2.4 Performance analysis of baseline schemes

In this section, we investigated two resource allocation baselines in terms of overall collision probability: 1) the 3GPP defined SPS scheme; 2) the random selection (RS) scheme, which also adopts the principle of randomness originated from the SPS scheme. Although the investigated baselines fully/partially follow the current standardized V2X scheduling algorithm aimed for broadcast communication, they have not been standardized for the platoon communication in the NR-V2X supported scenario.

We first decoupled the collision impacts due to the resource selection algorithm itself and collisions due to hidden terminal effects to provide an overall (combined) collision probability for each scheme. The key assumptions underlying the analytical model follow.

- Assumption 1: For the resource selection collisions, if at least one broadcast vehicle in the sensing range of the PL selects the same available RBG as the PL, some PMs cannot correctly receive packets from both vehicles.

- Assumption 2: For the hidden terminal effects, if at least one hidden vehicle selects the same RBG as the PL, the farthest in-platoon PM cannot correctly receive packets from both vehicles.

As a result of the above, each PM is the intended receiver for the PL messages and other broadcast sources (platoon and non-platoon). All packets, irrespective of source, have the same priority, i.e., each PM cannot distinguish the packets from broadcast vehicles or the PL when both packets are received at the same RBG.

Consider that both broadcast vehicles and the PL periodically generate packets every RRI ms. The resource pool is divided into a (pre-)configured number n_s of contiguous subchannels in the frequency domain, i.e., n_s RBGs in each slot. Each RBG is (pre-)configured to contain the same number of PRBs for low-payload packet transmission. Thus, the maximum number of available RBGs that PL (as well as broadcast vehicles) can select within the selection window is

$$N_r = \frac{RRI \cdot n_s}{t_s}, \tag{3.5}$$

where t_s is the slot duration which is determined by NR numerology, and n_s is the number of RBGs in each slot.

We first analyze the collision probability due to PL's resource selection. All broadcast vehicles within the sensing range of PL can sense the PL and all other vehicles within the sensing range. As a result, collision due to PL's resource selection can be modeled as a fully connected linear network, where N_{sen}^{PL} broadcast vehicles and the PL are within the sensing range of each other [13]. Under Assumption 3, some broadcast vehicles may enter

---

[13] Note that this assumption does not reflect the exact RBG distribution of the selection window for vehicles in the sensing range of the PL. However, due to the randomness in available RBG selection, this assumption captures the expected number of available RBGs in the selection window, determining the collision probability due to PL's resource selection.

the same selection window (Re-selection Counter = 0) as the PL. Here, a Markov chain of Re-selection Counter value is employed to derive the probability (π_0) that a broadcast vehicle reaches the state Re-selection Counter = 0; see Appendix 3.5.1. When a broadcast source enters the selection window, it will select an available RBG with probability $1-p$; as a result, the probability that a broadcast vehicle selects an available RBG within the same selection window as the PL is $\pi_0(1-p)$. As the Re-selection Counter of each broadcast vehicle are independent and identically distributed (i.i.d.) random variables, the probability that n $(1 \leq n \leq N_{sen}^{PL})$ out of N_{sen}^{PL} broadcast vehicles select available RBGs within the same selection window as the PL can be expressed as

$$P_s(n) = \begin{pmatrix} N_{sen}^{PL} \\ n \end{pmatrix} (\pi_0(1-p))^n \, (1-\pi_0(1-p))^{N_{sen}^{PL}-n}\,, \tag{3.6}$$

where $P_s(n)$ is a function of n. In the fully connected network, all vehicles have the same available RBGs in the selection window. Given N_r, the expected number of available RBGs depends on N_{sen}^{PL} and packet collision among broadcast vehicles. Since the collision among more than two broadcast vehicles in one RBG is an extremely low probability event, it may be ignored to 1st-order. The expected number of available RBGs in the selection window is thus given by

$$N_a = N_r - N_{sen}^{PL} + \frac{P_c^B N_{sen}^{PL}}{2}, \tag{3.7}$$

where P_c^B is the collision probability of broadcast communication. When at least one of n broadcast vehicles selects the same available RBG as the PL, a collision happens between N_a available RBGs. Since the probability that each broadcast vehicle selects the same available RBG as the PL is $1/N_a$, and given that n broadcast vehicles need to select available RBGs within the same selection window as the PL, the collision probability due to PL's resource selection is given by

$$P_r(n) = 1 - \left(1 - \frac{1}{N_a}\right)^n, \tag{3.8}$$

where $P_r(n)$ is a function of n. As a result, the probability that n out of N_{sen}^{Pl} broadcast vehicles collide with the PL is $P_s(n)P_r(n)$. Considering all cases of n, the collision probability due to PL's resource selection is thereby given by

$$P_{rs}^{PL} = \sum_{n=1}^{N_{sen}^{PL}} P_s(n)P_r(n). \tag{3.9}$$

Substituting equation (3.6) and (3.8) into (3.9), yields the following equation:

$$P_{rs}^{PL} = 1 - \left[1 - \frac{\pi_0(1-p)}{N_a}\right]^{N_{sen}^{PL}}, \tag{3.10}$$

where N_a is expressed in Eq. (3.7) containing an unsolved parameter, P_c^B. In order to determine P_{rs}^{PL}, a closed-form expression for P_c^B should be determined first. As Fig. 3.3 shows, with probability $1-p$, the tagged broadcast vehicle randomly selects an available RBG, and a collision happens when another broadcast vehicle selects the same RBG with probability $P_{c,1-p}^B$. Here, Eq. (3.6) - (3.10) still hold for the calculation of $P_{c,1-p}^B$, i.e., $P_{c,1-p}^B = P_{rs}^{PL}$, because the underlying events - of randomly selecting an available RBG by the tagged broadcast vehicle - is the same as the PL's random selection. On the other hand, with probability p, the tagged broadcast vehicle, which collided with another broadcast vehicle in the previous SPS period, still sticks with the previous reserved RBG; a collision happens when the vehicle which collided with the tagged vehicle in the previous SPS period also sticks with the previous reserved RBG with probability $P_{c,p}^B = pP_c^B$. P_c^B can be thereby expressed as

$$P_c^B = (1-p)P_{c,1-p}^B + pP_{c,p}^B. \tag{3.11}$$

Plugging $P_{c,1-p}^B$ and $P_{c,p}^B$ into Eq. (3.11), we obtain

$$P_c^B = \frac{1}{1+p}\left[1 - \left(1 - \frac{\pi_0(1-p)}{N_a}\right)^{N_{sen}^{PL}}\right]. \tag{3.12}$$

The value of N_a is found by solving Eq. (3.12) and Eq. (3.7). P_{rs}^{PL} and P_c^B can be further obtained through Eq. (3.10) and Eq. (3.12), respectively. Based on the above results, the collision probability due to PL's resource selection under the two baseline schemes are derived as follows:

- Random Selection (RS): The PL needs to select an available RBG in each RRI based on the corresponding prior sensing window, i.e., each RRI becomes a selection window of PL. As P_{rs}^{PL} in Eq. (3.10) is analyzed based on any single RRI, the collision probability due to PL's resource selection under the RS scheme should equal P_{rs}^{PL}.

- Semi-Persistent Scheduling (SPS): The behavior of PL for platoon broadcast is now configured to be the same as the broadcast vehicles, indicating that the collision probability due to PL's resource selection under the SPS scheme equals the collision probability of broadcast communication, i.e., P_c^B.

We then consider the collision from the hidden terminal effects under baseline schemes. Each hidden vehicle never senses PL's RBG selection, indicating that 1) the PL should suffer the same hidden terminal effects under both baseline schemes; 2) the Re-selection Counter value of a hidden vehicle can be any value other than 0 when it starts colliding with the PL. Then we can analyze the impact of each hidden vehicle on the PL separately. As Fig.3.4 illustrates, the overlapping range between the sensing range of the 1^{st} nearest hidden vehicle (of the PL) and the PL is approximately equal to R_{sen}. Thus, the 1^{st} nearest hidden vehicle can sense at most (on average) $N_{sen}^{PL}/2$ broadcast vehicles in the sensing range of PL. Then the $m^{th}(1 \leq m \leq N_{ht}^{PL})$ nearest hidden vehicle (of the PL) can sense at most (on average) $N_{sen}^{PL}/2 - m$ vehicles in the sensing range of PL, randomly selecting one of the remaining $N_r - (N_{sen}^{PL}/2 - m)$ available RBGs. Therefore, the probability that the m^{th} nearest hidden vehicle collides with the PL is $1/(N_r - (N_{sen}^{PL}/2 - m))$. Given N_{ht}^{PL} hidden vehicles, the probability that at least one of the hidden vehicles collide with the PL under both baseline schemes is

$$P_{ht}^{PL} = 1 - \prod_{m=1}^{N_{ht}^{PL}} \left[1 - \frac{1}{N_r - (N_{sen}^{PL}/2 - m)} \right]. \tag{3.13}$$

As stated in the prior subsection, a packet collision for platoon broadcast happens if either the resource selection collisions or the hidden terminal effects. Under the RS scheme, the collision probability due to PL's resource selection is P_{rs}^{PL} while the collision probability due to hidden terminal effects is P_{ht}^{PL}. The overall collision probability under the RS scheme is thus given by

$$P_{c,RS}^{PL} = 1 - (1 - P_{rs}^{PL})(1 - P_{ht}^{PL}). \tag{3.14}$$

Similarly, under the SPS scheme, the collision probability due to PL's resource selection is P_c^B while the collision probability due to hidden terminal effects is P_{ht}^{PL}. The overall collision probability under the SPS scheme can be written as

$$P_{c,SPS}^{PL} = 1 - (1 - P_c^B)(1 - P_{ht}^{PL}). \tag{3.15}$$

Proposition 1 *$P_{c,RS}^{PL} \geq P_{c,SPS}^{PL}$ as a function of the resource keeping probability $p \in (0, 0.8]$. This can be straightforwardly proved by comparing P_{rs}^{PL} and P_c^B given by Eq. (3.10) and Eq. (3.12), respectively. We further obtain $P_c^B = \frac{1}{1+p} P_{rs}^{PL}$.*

Proposition 1 indicates that the SPS scheme mitigates the collision impact under the SPS-based broadcast environment by decreasing PL's resource selection frequency compared with the RS scheme. Notice that the PL reserves an RBG for at least one SPS period under the SPS scheme while reserving an RBG for each RRI under the RS scheme.

Remark 1 *According to Proposition 1, $P_{c,RS}^{PL} = P_{c,SPS}^{PL}$ if $p = 0$ as $P_c^B = P_{rs}^{PL}$. This indicates that decreasing the resource selection frequency no longer takes advantage of collision avoidance. In such a case, even with the same overall collision probability, RS is more practical than SPS for the latency-sensitive based platoon communication because SPS cannot overcome consecutive collision issues.*

3.2.5 Performance analysis of IRS scheme

As indicated in the previous section, the investigated baselines cannot meet platoon communication's latency and reliability requirements. Specifically, SPS cannot avoid consecutive collision issues, while RS cannot reduce the impact of resource selection collisions. This section thereby introduces an improved random selection (IRS) scheme to overcome the above

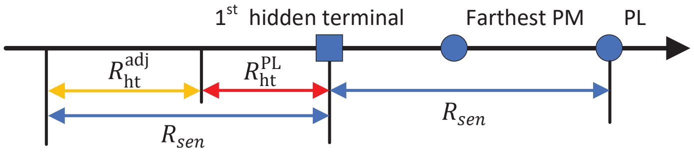

Figure 3.6: The adjacent range of PL's hidden terminal range.

issues. We also employ two-state Markov chains to illustrate the reason why IRS performs better than the baselines in terms of overall collision probability.

Under the IRS scheme, the PL first randomly selects an available RBG in the selection window. If a collision does not happen in the selection window, the PL will stick with that RBG until the collision happens again. The PL randomly re-selects an available RBG in the selection window right after the prior RRI in which the collision happened and then repeats the previous process. Note that the collision probability due to PL's resource selection under the IRS scheme, $P_{rs,IRS}^{PL}$, still satisfies $P_{rs,IRS}^{PL} = P_{rs}^{PL}$ which is expressed in Eq. (3.10).

We then consider the collision probability due to the hidden terminal effects. The vehicles in the adjacent range of PL's hidden terminal range also impact the RBG selections of PL's hidden vehicles, as is shown in Fig. (3.6). Since those vehicles are in the sensing range of the 1^{st} hidden vehicle, which is the nearest hidden vehicle of the PL, if at least one broadcast vehicle in the adjacent range has selected the same RBG as the PL, the hidden vehicles cannot select the same RBG as the PL when they need to select an available RBG based on the sensing results. Note that the average number of vehicles in this range is

$$N_{ht}^{adj} = M\rho(R_{sen} - R_{ht}^{PL}), \tag{3.16}$$

where R_{sen} is the sensing range, and R_{ht}^{PL} is the hidden terminal range of PL. We assume that each vehicle in this range can sense at most N_{ht}^{adj} RBGs occupied by the vehicles in the sensing range of PL and then randomly selects one of the remaining $N_r - N_{ht}^{adj}$ RBGs. Therefore, the probability that none of vehicles in this range has selected the same available

RBG as the PL is

$$P_{ht}^{adj} = \left[1 - \frac{\pi_0(1-p)}{N_r - N_{ht}^{adj}}\right]^{N_{ht}^{adj}}. \tag{3.17}$$

Note that if the vehicles in this range select the same available RBG as the PL, a packet collision doesn't happen between them because those vehicles and the PL are out of the sensing range of each other. Similarly, we assume that each hidden terminal vehicle can not only sense at most (on average) $N_{sen}^{PL}/2$ RBGs occupied by the vehicles in the sensing range of PL but also sense at most N_{ht}^{adj} RBGs occupied by the vehicles in its own sensing range. Each of hidden terminal vehicle then randomly selects one of the remaining $N_r - N_{ht}^{adj} - N_{sen}^{PL}/2$ RBGs. Thus, the probability that at least one broadcast vehicle in the hidden terminal range collides with the PL is

$$P_{ht,IRS}^{PL} = 1 - \left[1 - \frac{\pi_0(1-p)P_{ht}^{adj}}{\left(N_r - N_{ht}^{adj} - N_{sen}^{PL}/2\right)}\right]^{N_{ht}^{PL}}, \tag{3.18}$$

where N_{ht}^{PL} and N_{sen}^{PL} are the average number of broadcast vehicles in the hidden terminal range and the sensing range of PL, respectively.

Remark 2 *Due to the characteristics of IRS scheme, the probability that the platoon leader collides with a broadcast vehicle in the hidden terminal range of platoon leader is scaled by* $\pi_0(1-p)$*, which remarkably mitigates the hidden terminal effects compared with the SPS and the RS scheme.*

The overall collision probability in each RRI in the IRS scheme follows the two-state Markov chain, which is shown in Fig. 3.7. If a packet is successfully delivered in the prior RRI, in the current RRI, the packet collision is only determined by the hidden terminal effects. This is because the broadcast vehicles in the sensing range of PL have sensed the RBG occupied by the PL over the previous several RRIs, and they no longer select the same RBG as the PL in the current RRI. However, if a packet collision happened in the prior RRI, the PL must randomly select an available RBG in the current RRI (selection window). The

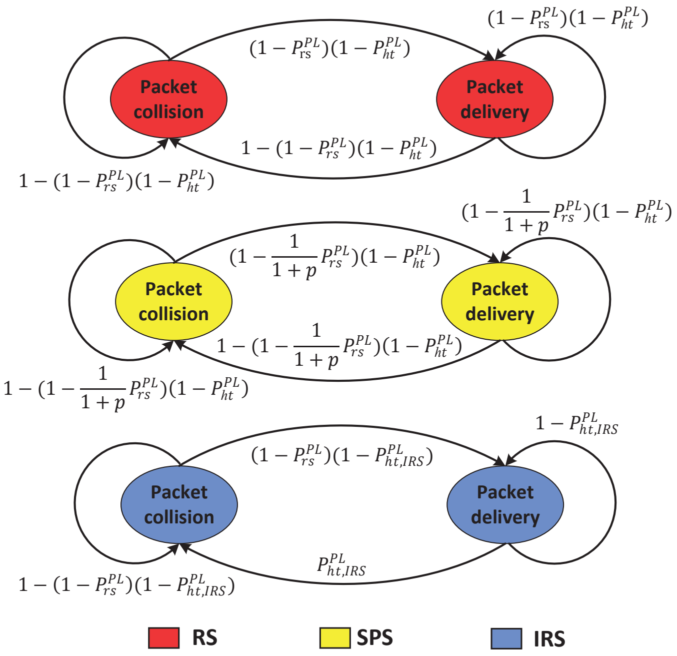

Figure 3.7: Two-state Markov chain comparison between the baselines and the IRS scheme.

collision may happen again due to resource selection collisions or the hidden terminal effects. According to the two-state Markov chain, the overall collision probability satisfies

$$\begin{aligned} P_{c,IRS}^{PL} =& (1-P_{c,IRS}^{PL})P_{ht,IRS}^{PL} \\ &+ P_{c,IRS}^{PL}\left[1-(1-P_{ht,IRS}^{PL})(1-P_{rs,IRS}^{PL})\right]. \end{aligned} \tag{3.19}$$

Rearrange Eq. (3.19), $P_{c,IRS}^{PL}$ is expressed as

$$P_{c,IRS}^{PL} = \frac{P_{ht,IRS}^{PL}}{1-P_{rs,IRS}^{PL}+P_{ht,IRS}^{PL}P_{rs,IRS}^{PL}}. \tag{3.20}$$

Fig.7 illustrates the Markov chains of the IRS and baselines to compare their state transitions. One main difference between the baselines and the IRS scheme is the state transition which is from packet delivery to packet collision. Under the baselines, given that a packet is successfully delivered in the current RRI, the occurrence of packet collision in the next

RRI is impacted by the resource selection collisions as well as the hidden terminal effects. By contrast, the corresponding state transition under the IRS scheme is only triggered by the mitigated hidden terminal effects. Once the PL succeeds in occupying an RBG at the beginning, IRS then reduces the overall collision probability by 1) preventing the resource selection collisions from happening, i.e., forcing the P_{rs}^{PL} term to be 0; and 2) mitigating the hidden terminal effects, i.e., scaling the P_{ht}^{PL} term into a lower value. When a collision happens in the current RRI, the PL under the IRS is required to occupy a new RBG in the next RRI. It should be noted that a collision may happen in the next RRI, and the possible collision types would be the same as the ones under the baselines. However, since the collision probability due to hidden terminal effects under the IRS (i.e., $P_{ht,IRS}^{PL}$) is much lower than the one under the baselines (i.e., P_{ht}^{PL}), the probability that a collision happens again in the next RRI given that the collision happens in the current RRI (i.e., the transition probability from packet collision to packet collision, indicated by $1-(1-P_{rs}^{PL})(1-P_{ht,IRS}^{PL})$), is much lower than the corresponding ones under the baselines.

3.3 *Deep Deterministic Policy Gradient*

As the previous section indicates, the proposed IRS scheme following the specific procedures can significantly improve the performance compared with the baselines. Notice that IRS, as well as the baselines, are all provided with the model-based analysis rigorously. Since the channel changes dynamically due to the resource-keeping probability, meanwhile, the feedback mechanism exists in the platoon communication, the platoon leader may be able to learn from the dynamic channel environment with the potential pattern. Therefore, a model-less deep reinforcement learning (DRL)-driven scheme can also be considered as an option to optimize the resource allocation for platoon communication in the NR-V2X supported scenario.

In this section, we explore whether the DRL-driven algorithm [68, 102–113] can be also effective. In particular, it would be interesting to see whether or how far the designed algorithm can improve the performance compared with the baselines as well as the IRS. We propose a Deep Deterministic Policy Gradient (DDPG) framework, which is quite suitable for solving the discussed resource allocation problem. DDPG is a deep reinforcement learning approach to solve the continuous problem that exists the high dependency with each action every time [114–122], e.g., the action (RBG selection) keeps the same in consecutive RRIs to avoid the packet collision from either resource selection or hidden terminal effects. Under the continuous characteristic of the real-time status and the action items described in the next, it is suitable to analyze the optimization problem of resource allocation for platoon communication by DDPG. With effective action and reward design, the PL learns favorable decisions to mitigate the collision effects by interacting with the broadcast vehicles. Meanwhile, the DDPG algorithm also helps improve the learning efficiency compared with traditional deep reinforcement learning algorithms such as Deep Q-Networks (DQNs), which makes it possible to meet the reliability requirement of platoon communication in a short period.

3.3.1 Markov Decision Process

As shown in Fig. 3.5, in the n^{th} RRI (i.e., $n = 1, 2, ...$), the PL selects an action $a_n \in \mathcal{A}_{n-1} \subseteq \mathcal{A}$, where $\mathcal{A}$ is the action set of all RBGs in one RRI while $\mathcal{A}_{n-1}$ is the action set of the available RBGs in the $(n-1)^{th}$ RRI. If we denote the fixed set $\mathcal{A} = \{RBG_1, RBG_2, ..., RBG_{N_r}\}$, where each RBG in a RRI is indexed, and $\mathbb{1}_{idle}(m)$ indicates whether RBG_m is available. Thus $\mathcal{A}_{n-1}$ can be described as

$$\mathcal{A}_{n-1} = \{RBG_m | RBG_m \in \mathcal{A} \ and \ \mathbb{1}_{idle}(m) = 1\}. \tag{3.21}$$

Note that $\mathcal{A}_{n-1}$ is a dynamic set due to the resource keeping probability in the broadcast environment. The PL then observes the received feedback from the PMs, $o_n \in \{ACK, NACK\}$ before the end of this RRI, and utilizes the historical observations and its own past actions, to select the next action $a_{n+1} \in \mathcal{A}_n$ in the next RRI, i.e., $(n+1)^{th}$ RRI.

Next, we denote the action-observation tuple of the PL in the n^{th} RRI as $c_n = \{a_n, o_n\}$. Denote the environment history of the PL as the state in the n^{th} RRI, $s_n = [c_{n-M+1}, ..., c_{n-1}, c_n]$

which is a combination of historical selected RBGs as well as its observed feedback over previous M RRIs. Based on s_n, the PL takes an action a_n and the state s_n transfers to s_{n+1} with reward r_n. The reward in our framework is designed to meet both reliability (lower collision probability) and latency (lower scheduled delay) constraints for each packet transmission. The scheduled delay of a packet is defined as the interval between the packet generation time and the instant when this packet starts transmission. The reward function r_n for each successful packet transmission is calculated as the following equation:

$$r_n = 1 + \beta_1 \left[1 - \frac{1}{1 + \exp(-\beta_2 (t_n^r / (RRI - t_s) - \beta_3))} \right], \tag{3.22}$$

where the first additive term (i.e., 1) is the reliability component while the second additive term is the latency component. For the latency component, $\beta_1 \in (0, 1)$ emphasizes the importance of latency constraint for successful transmission. $t_n^r \in [0, RRI - t_s]$ is the real-time scheduled delay in the n^{th} RRI, where t_s is the slot duration. We use $t_n^r/(RRI - t_s)$ to scale the real-time scheduled delay into the range of [0,1]. $\beta_2 > 50$ and $\beta_3 \in (0, 1)$ control the shape of the delay-related reward curve so that more reward will be assigned when a lower real-time scheduled delay happens for successful packet transmission. Otherwise, if a packet collision happens for the platoon communication in the n^{th} RRI, the reward will be assigned 0, i.e., $r_n = 0$. As illustrated above, the state s_{n+1} only depends on s_n after the PL takes action a_{n+1}. The state description of the PL can be used to construct a *Markov Decision Process (MDP)* formulation.

3.3.2 DDPG Framework

The goal of the PL under DDPG is to seek a policy that maximizes the expected long-term number of successful packet transmissions. The cumulative reward of the PL from a state s_n can be expressed as

$$R_n = \sum_{k=n}^{\infty} \gamma^{((k-n)} r_n(s_n, a_n), \tag{3.23}$$

where $\gamma \in (0, 1]$ is a discounting factor to avoid the accumulated reward being infinity, and $r_n(s_n, a_n)$ is the reward by taking action a_t at state s_t. Reinforcement learning problems that depend only on the current state of the environment are said to comply with the *MDP*. The dynamics of resource allocation for platoon communication are therefore defined by the probability of reaching from a state s to a state s‘ by means of action a:

$$p(s'|s,a) = P(s_{n+1} = s'|s_n = s, a_n = a). \tag{3.24}$$

The action-value function of the PL, $Q^{\pi}(s,a)$, is defined as the expected sum of the discounted reward received starting from the state s, taking action a and then following a policy π thereafter, which can be formally expressed as

$$Q^{\pi}(s,a) = \mathbf{E}[R_n|s_n = s, a_n = a; \pi]. \tag{3.25}$$

If we denote $Q^{\pi^*}(s,a)$ as the action-value with initial state s and action a and then following the optimal policy π^*, the optimal policy π^* can be derived as

$$\pi^*(s) = \arg\ \max_a Q^{\pi^*}(s,a), \forall s, \tag{3.26}$$

where $Q^{\pi^*}(s,a)$ can be obtained by letting the PL update $Q(s_n, a_n)$ in each RRI. The update rule of $Q(s_n, a_n)$ is given as follows:

$$\begin{aligned} Q(s_n, a_n) \leftarrow\ & Q(s_n, a_n) \\ & + \alpha \left[r_{n+1} + \gamma \max_{a_{n+1}} Q(s_{n+1}, a_{n+1}) - Q(s_n, a_n) \right], \end{aligned} \tag{3.27}$$

where $\alpha \in (0,1]$ denotes the learning rate.

As introduced beforehand, in the n^{th} RRI, the action a_n transfers the state s_n to s_{n+1} which gives the reward r_n. At the end of this RRI, the PL can also obtain the information about $\mathcal{A}_n$, which is the set of available actions for the next RRI as the PL has experienced the whole current RRI. Thus, the above information, $(s_n, a_n, r_n, s_{n+1}, \mathcal{A}_n)$, forms a single batch of the training set for Deep Q-network (DQN). Given the reward information r_n, DQN can be trained by minimizing the mean squared error (MSE). More specifically, the prediction loss function of DQN is given by

$$L(\boldsymbol{\theta}) = \mathbf{E}\left[(y(r_n, s_{n+1}, \mathcal{A}_n; \boldsymbol{\theta}^-) - Q(s_n, a_n; \boldsymbol{\theta}))^2 \right], \tag{3.28}$$

where $Q(s_n, a_n; \boldsymbol{\theta})$, defined as the predicted value function, is the output of DQN, and the target value function is defined as

$$y(r_n, s_{n+1}, \mathcal{A}_n) = r_n + \gamma \max_{a_{n+1} \in \mathcal{A}_n} Q(s_{n+1}, a_{n+1}; \boldsymbol{\theta}^{-}), \tag{3.29}$$

where the second term $\max Q(s_{n+1}, a_{n+1}; \boldsymbol{\theta}^{-})$ is obtained by searching the maximum output of DQN with respect to the selection of available action a_{n+1} given s_{n+1}, and $\boldsymbol{\theta}^{-}$ are the parameters of neural network (NN) from the previous iterations. $\boldsymbol{\theta}$ are the parameters of NN, which can be trained through the gradient direction of Eq. (3.28):

$$\nabla_{\boldsymbol{\theta}} L(\boldsymbol{\theta}) = \mathbf{E}\left[(y(r_n, s_{n+1}, \mathcal{A}_n; \boldsymbol{\theta}^{-}) - Q(s_n, a_n; \boldsymbol{\theta})) \nabla_{\boldsymbol{\theta}} Q \right]. \tag{3.30}$$

Note that the fundamental concept of DDPG is to integrate DNN into Deterministic Policy Gradient (DPG) algorithm to improve the learning efficiency compared with DQN. The original formulation of the policy gradient algorithm was proposed in [123], which proved the policy gradient theorem for a stochastic policy $\pi(s, a; \theta)$:

Theorem 1 ***(Policy Gradient theorem from [123])***

For any MDP, if the parameters θ of the policy are updated proportionally to the gradient of its performance Ψ, θ can be then assured to converge to a locally optimal policy in Ψ, being the gradient computed as,

$$\nabla \theta \approx \alpha \frac{\partial \Psi}{\partial \theta} = \alpha \sum_s d^{\pi}(s) \sum_a \frac{\partial \pi(s, a)}{\partial \theta} Q^{\pi}(s, a) \tag{3.31}$$

with α being a positive step size and where d^{π} is defined as the discounted weighting of states encountered starting at s_0 and then following π: $d^{\pi}(s) = \sum_{n=0}^{\infty} \gamma^n P(s_n = s | s_0, \pi)$ [124].

This theorem is further extended for the case where an approximation function f is used in place of the policy π. In this condition, the theorem holds valid as long as the weights of the approximation tend to be zero upon convergence. The deterministic policy can be approximated by a NN actor $\pi(s; \theta^{\pi})$ that depends on the state s and has weights θ^{π}, and another separate network critic $Q(s, a; \theta^Q)$ of which the predicted target value function now becomes:

$$y(r_n, s_{n+1}, \mathcal{A}_n) = r_n + \gamma Q(s_{n+1}, \pi(s_{n+1}; \boldsymbol{\theta^\pi}); \boldsymbol{\theta^Q}). \tag{3.32}$$

The actor is updated by following the applying the chain rule to the loss function expressed in Eq. (3.28) and updating the weights θ^π by following the gradient of the loss with respect to them:

$$\begin{aligned} \nabla_{\boldsymbol{\theta^\pi}} L(\boldsymbol{\theta^\pi}) &\approx \mathbf{E}\left[\nabla_{\boldsymbol{\theta^\pi}} Q\left(s, \pi(s; \boldsymbol{\theta^\pi}); \boldsymbol{\theta^Q}\right)\right] \\ &= \mathbf{E}\left[\nabla_a Q\left(s, a; \boldsymbol{\theta^Q}\right)|_{a=\pi(s;\boldsymbol{\theta^\pi})} \nabla_{\boldsymbol{\theta^\pi}} \pi(s; \boldsymbol{\theta^\pi})\right], \end{aligned} \tag{3.33}$$

where an exploration policy π can be constructed by adding noise sampled from a noise process N to the actor policy [114] as follows

$$\pi_{s_n} = \pi(s_n; \boldsymbol{\theta^\pi_n}) + N. \tag{3.34}$$

3.4 Simulation

In this section, we present the analytical results and simulations for the baselines (SPS and RS) as well as the IRS, comparing their packet collision probabilities in terms of vehicle density and the resource keeping probability. We further compare the performance between DDPG and IRS from the perspective of reliability and latency

3.4.1 Simulation Setup

The simulations were implemented using MATLAB R2021a on a CPU (Intel Core i9-9700k) server and a GPU (NVIDIA GeForce GTX 2080Ti). We conduct Monte-Carlo simulations of C-V2X networks introduced in [125], where Table 3.3 lists the main system parameters. We repeated 50 trials for each vehicle density and resource keeping probabilities of producing averages for the relevant results. Vehicle location is a uniformly distributed random variable over the maximum segment length in each trial.

Table 3.3: Main simulation parameters

Parameters	**Value**
Center frequency f_c (GHz)	6
Numerology μ	0
Bandwidth part, BWP (MHz)	40
Number of subchannels per slot n_s	3
Number of PRBs per subchannel	50
Transmit power P_{TX} (dBm)	20
Sensitivity power level P_{sen} (dBm)	-91
Shadowing of V2V link SH (dB)	3
Noise Figure NF (dB)	9
Noise PSD P_N (dBm/Hz)	-174
Highway length (km)	5
Vehicle density per lane ρ (vehicles/km)	{20,40,...,100}
Number of lanes M	3
Lane width Δ (m)	4
Platoon length L_p (km)	0.2
RRI duration (ms)	100
Resource keeping probability	{0.1, 0.3, 0.5, 0.7}
Re-selection counter	[5, 15]

3.4.2 Baseline schemes

In this section, we first compare the collision probability between the two baseline schemes for platoon communication. As Fig. 3.8(a) shows, the simulations of two baselines are consistent with their corresponding analytical results in terms of vehicle density and resource keeping probability. For the same resource keeping probability, the collision probability under both SPS and RS decreases as the vehicle density increases as expected. Meanwhile, the collision probability under both baselines decreases with the same vehicle density decreases as the resource keeping probability decreases. With lower resource keeping probability, each broadcast vehicle selects available RBGs more frequently, more likely to select the same available RBG as the PL. Notably, the collision probability under the SPS is always lower than the RS in terms of vehicle density with the same resource keeping probability. In

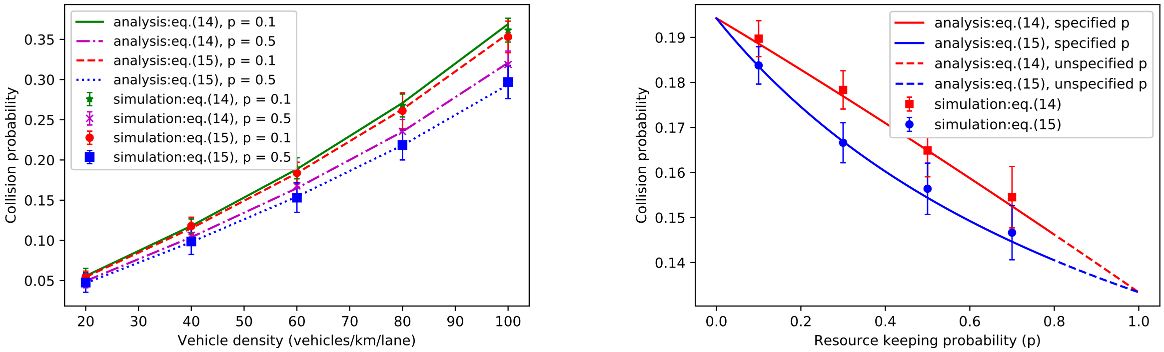

(a) Overall collision probability with respect to vehicle density.

(b) Overall collision probability regarding the resource keeping probability under 60 vehicle/km/lane.

Figure 3.8: Overall collision probability between SPS and RS.

particular, with $p = 0.1$, the collision probability under the RS is pretty close to the one under the SPS.

We also explore the performance of two baseline schemes in the range of resource keeping probability. Fig. 3.8(b) shows how the overall collision probability changes regarding the specified/unspecified resource keeping probability under a specific vehicle density. For both baseline schemes, the collision probability decreases with the increasing resource keeping probability. Thus, a high resource keeping probability set in an SPS-based broadcast environment helps to improve PL's resource scheduling performance. Proposition 1 states that the overall collision probability with RS is greater than or equal to the collision probability with SPS in the specified resource keeping probability range $p \in [0, 0.8]$. In particular, when $p = 0$, the overall collision probability under both schemes is equal. Since both schemes impact Platoon broadcasts with the same hidden terminal effects, the overall collision probability difference is mainly caused by the resource selection collisions. We can see that the SPS scheme effectively mitigates the collision impact on platoon broadcast due to resource selection.

In addition, we provide the overall collision probability for the unspecified resource keeping probability range, i.e., $p \in (0.8, 1]$. Note that when $p = 1$ (each broadcast vehicle initially selects an available RBG reserved for all following RRIs), the overall collision probability under both schemes is the lowest over resource keeping probability range, respectively. However, in such a scenario, the PL suffers differently even though both schemes have the same collision probability. Under the RS scheme, the PL selects an available RBG in each RRI; the collision probability can reflect the actual collision condition for platoon communication in the long run. By contrast, under the SPS scheme, the collision probability is only determined by PL's first RBG selection, e.g., if another broadcast vehicle initially selects the same available RBG as the PL, collision will happen in all following RRIs; otherwise, collision will never happen. Hence, high resource keeping probability in the range is infeasible under the SPS scheme because it causes long-term consecutive collisions.

3.4.3 IRS scheme

We further show the performance of the IRS and compare it with the baseline schemes. Fig. 3.9(a) illustrates the overall collision probability between baselines and IRS with respect to vehicle density. Under the IRS scheme, the analytical model prediction matches well with the simulation results. IRS significantly decreases the overall collision probability compared with the baselines. Remarkably, the overall collision probability with IRS is at least 25% lower than that with baseline algorithms for up to 100 vehicles/km/lane. With the PMs' feedback, IRS can mitigate the resource selection collisions by reserving one RBG until a collision happens on that RBG.

Meanwhile, IRS also significantly mitigates the hidden terminal effects. Fig. 3.9(b) shows the collision probability due to the hidden terminal effects in terms of vehicle density. The PL suffers the same hidden terminal effects under the baselines while being less impacted under IRS. Since the probability that each hidden vehicle collides with the PL is scaled by $\pi_0(1-p) = 0.05$, each hidden vehicle is less likely to select the RBG that the PL has reserved

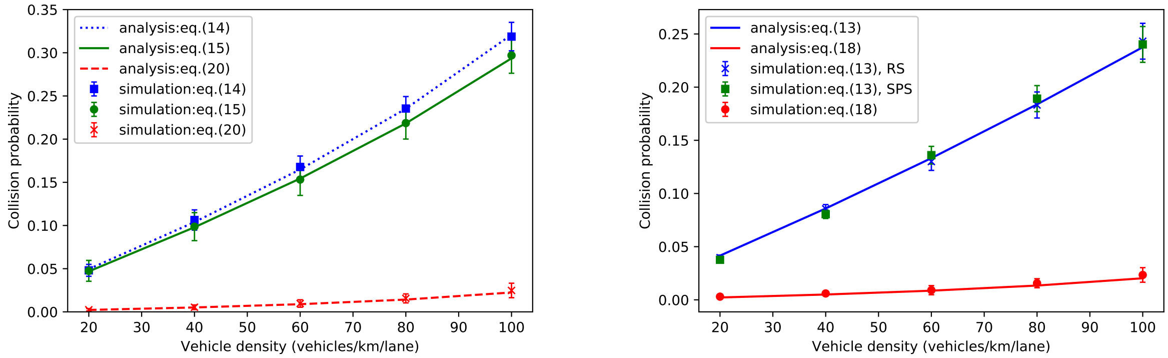

(a) Overall collision probability with respect to vehicle density.

(b) Collision probability due to hidden terminal effects.

Figure 3.9: Overall collision probability between baselines and IRS with $p = 0.5$.

for platoon broadcast. Since the hidden terminal effects dominate the overall collision on platoon communication, this leads to a lower proportion of resource selection collisions.

3.4.4 DDPG algorithm

We next propose to use the DDPG algorithm introduced in Section 3.3 within the same simulation architecture. In each RRI, the PL collects the historical actions, i.e., the selected RBGs, and the historical observations, i.e., the received feedback from PMs, over the previous 16 RRIs to construct the state, and then the deep neural network outputs an RBG index which corresponds to one of the available RBGs in an RRI.

We construct a five-layer deep DDPG, with two 1-dimensional convolution layers and three fully connected layers. For the system model detailed in Section 3.2, the state dimension and input data are relatively small in the examples simulated, and we thus chose a five-layer DDPG which is not too deep in order for the model weight to be controlled. Table 3.4 lists the hyperparameters of the DDPG neural network.

The overall collision probability comparison between IRS and DDPG is shown in Fig.

Table 3.4: Hyper-Parameters of DRL

Parameters	**Value**
State size	32
Batch size	1
Action size	300
Learning rate	0.01
γ in Eq. (3.29)	0.9
Memory size	1000

3.10. For the same resource keeping probability, DDPG consistently outperforms IRS for different vehicle densities. Since the DDPG algorithm learns by constructing the network state, including the historical actions and observations, it always outperforms the IRS under the same environment (the same resource keeping probability). Regarding the change of resource keeping probability, the DDPG is less sensitive than IRS because it maintains a memory size of each state, training the neural network from memory. Thus, the PL can learn the broadcast environment's status and is less likely to be impacted by the change in the resource keeping probability.

Compared to the IRS, DDPG improves reliability and reduces the latency for each successful packet transmission. Fig. 3.11 illustrates the average scheduled delay [14] between the DDPG and IRS under $p = 0.5$. For the IRS scheme (also for the baseline schemes), since the PL randomly selects an available RBG in the selection window of which the duration is 100 ms, the average scheduled delay is around 50 ms in each vehicle density. In contrast, the average scheduled delay in DDPG is reduced by assigning a higher reward for a successful packet transmission with a lower scheduled delay. Note that the average scheduled delay with DDPG will increase as the vehicle density increases. With a higher vehicle density, more RBGs are occupied by broadcast communication. Thus it becomes more difficult for

---

[14] Under one vehicle density, we first calculate the mean of the scheduled delay over all RRIs in each trial and then average the mean scheduled delay of all trials.

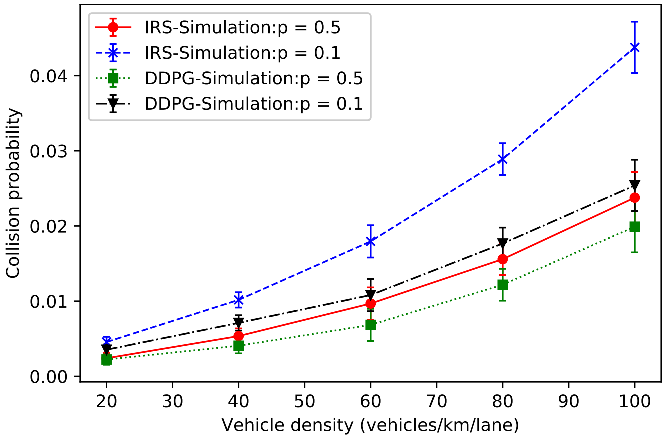

Figure 3.10: Overall collision probability between IRS and DDPG.

the PL to reach the same scheduled delay to deliver a packet successfully. Nevertheless, the average scheduled delay with DDPG is still lower than that with IRS in each vehicle density. It should be noted that the PL under the DDPG also follows the principle of randomly selecting one of the idle RBGs in an RRI in the exploration stage. This indicates that the average scheduled delay under DDPG cannot outperform that under IRS.

Under the IRS scheme, the PL only relies on its sensing results and the PMs' feedback to perform the resource selection directly. Hence, compared with baselines, IRS significantly improves its performance without sacrificing any additional resources. By contrast, the PL under DDPG has to collect the historical information over previous RRIs and apply the constructed neural network to output a RBG index for the next resource selection. However, running the DDPG algorithm in a real system, the PL, requires much more resources than the IRS in the following aspects: 1) **storage resources:** PL has to store the selected RBGs as well as its observed feedback over previous RRIs; 2) **computation resources:** In each RRI, the PL needs to update the historical information and then train the DDPG network to output the best action. It should be noted that the duration of each RRI is quite short (e.g., 100 ms). Thus PL requires enough computing capability to train the DDPG network

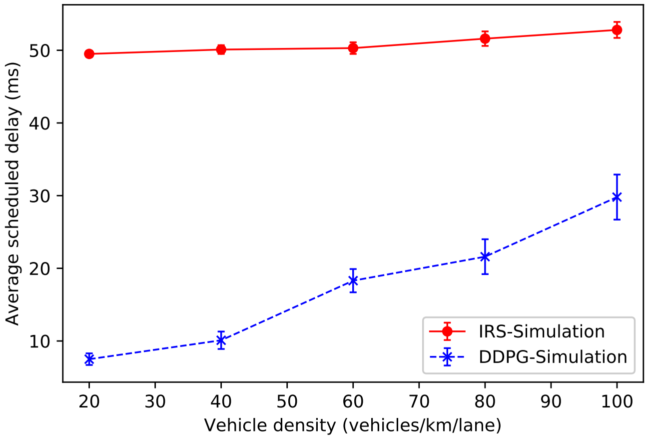

Figure 3.11: Average scheduled delay between IRS and DDPG with $p = 0.5$.

to output a reliable action during this period. Meanwhile, due to the dynamic broadcast environment, the PL is required to keep training the DDPG network all the time. As a result, the PL needs quite a large computation resource under DDPG.

Although DDPG generally performs better than IRS in terms of the overall collision probability, as is shown in Fig. 10, such a difference is subtle, especially in the case of the low vehicle density or high resource keeping probability. Therefore, IRS should be a better option in these cases. In addition, as Fig. 11 shows, the average scheduled delay difference becomes close between IRS and DDPG in the high vehicle density. Thus if the reliability and the latency are both taken into account, it would be more reasonable to choose IRS for a platoon system being in an environment with high vehicle density and high resource keeping probability.

3.5 Summary

In this chapter, novel resource allocation approaches were proposed for platoon communication under the SPS-based broadcast environment, which characterized the new feature brought by NR-V2X. The newly designed approaches aimed to improve the intercommunication performance of vehicle platooning which was significantly impacted by other vehicular communication types outside of the platoon. We analyzed the baseline resource allocation schemes and then proposed the Improved Random Selection (IRS) scheme which effectively eliminated the issues that originated from the baselines. Afterward, we proposed to employ Deep Deterministic Policy Gradient (DDPG) algorithm, to let the PL explore the inter-vehicle collaboration impacted by the environment, further optimizing the reliability and the latency based on local information. Via the simulation, numerical results show that IRS performs better than the baseline approaches in mitigating packet collisions by the hidden terminal effects. Meanwhile, DDPG outperforms IRS in terms of the overall collision probability as well as average scheduled delay and is more robust to the change of the broadcast environment that the new feature supports.

Appendices

3.5.1 Derivation for π_0

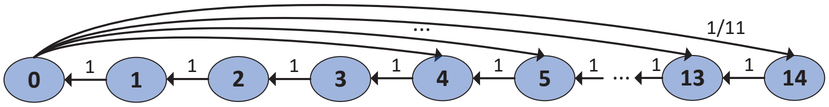

Figure 3.12: Markov chain of Re-selection Counter value.

Fig. 3.12 shows the Markov Chain of Re-selection Counter value under the SPS scheme. Denote π_i is the probability that Re-selection Counter $= i$ where $0 \leq i \leq 14$ at the end of the n^{th} RRI (also indicating the beginning of the $(n+1)^{th}$ RRI). In particular, π_0 is the probability that a broadcast vehicle enters the selection window (i.e., Re-selection Counter $= 0$). As a result, π_0 satisfies

$$\pi_i = \begin{cases} \pi_0, & 0 \le i \le 3 \\ \frac{1}{11}\pi_0 + \pi_{i+1}, & 4 \le i \le 13 \\ \frac{1}{11}\pi_0, & i = 14 \end{cases} \tag{3.35}$$

In addition, all π_i satisfy

$$\sum_{i=0}^{14} \pi_i = 1 \tag{3.36}$$

By substituting Eq. (3.35) into Eq. (3.36), we can obtain $\pi_0 = 0.1$.

Chapter 4

REVISITING MULTI-USER DOWNLINK IN IEEE 802.11AX: A DESIGNERS GUIDE TO MU-MIMO

4.1 Motivation

Despite the promise of MU-MIMO for improved network capacity via simultaneous transmission to multiple users on downlink[1], real-world user testing has revealed significant challenges [126–128]. A noticeable discrepancy exists between the theoretical speeds advertised by manufacturers who incorporate DL MU-MIMO and the actual throughput measured in specific conditions [14–16, 129–131]. An industry test report [132] showed that turning on MU-MIMO resulted in 58% aggregate throughput *loss* compared to SU-MIMO when pairing 4 x 4 Broadcom-based router with 2 x 2 Qualcomm-based STAs. An earlier research study [133] demonstrated that DL SU-MIMO achieves 16.8% to 42% higher aggregated throughput MU-MIMO based on a test of a commercial 4 x 4 MU-MIMO-capable 802.11ac 5 GHz radio with 1 x 1 Xiaomi Mi 4i smartphones. Such variation in results is attributable to various factors at play, including the complex interplay of channel state information (CSI) overhead, device capabilities and environmental (propagation) conditions as a function of user location. In this article, we chose the IEEE 802.11ax indoor channel model [134], widely used by the industry and academia, for a foundational exploration of DL SU/MU-MIMO throughput. Specifically, as the selected sub-set of clients for MU-MIMO on downlink are closer to each other in dense networks, increased spatial correlation will lead to significant inter-user and inter-stream interference in DL MU-MIMO. Thus overall network throughput degrades unless counteracted by a combination of inter-user interference cancellation and user selection algo-

---

[1] There exists an analogous feature for the uplink: trigger-based OFDMA whereby a 20 MHz channel may be shared synchronously by multiple users. However, consideration of UL OFDMA is beyond the scope of this article.

rithms [135–137]. Moreover, CSI overhead affects both SU and MU aggregate throughput; in particular, CSI overhead increases significantly with the dimensionality of MU-MIMO. In turn, this implies that any MU-MIMO design must carefully consider the issue of (optimal) channel sounding periodicity when confronted with channel time variations[2].

The lack of a sufficiently deep understanding of the interplay between the various underlying factors discussed has resulted in AP vendors turning off the DL MU-MIMO feature as default setting in their products, reflecting the current ambivalence surrounding DL MU-MIMO. The primary purpose of this article is therefore to provide *new insights underlying the fundamental question*: "**when should DL MU-MIMO be turned on/off**" as a function of the operational scenario. By a combination of analysis and computation/simulation, we attempt to answer the above question by

- Identifying set of conditions where DL SU-MIMO outperforms MU-MIMO and vice-versa;
- Provide broad 'rules of thumb' regarding use of DL MU-MIMO in current/future Wi-Fi systems.

The rest of this chapter is organized as follows. Section 4.2 introduces the impact of DL SU and MU CSI overhead differences on their effective channel capacity; In Section 4.3, we explore the impact of spatial correlation on the MU channel capacity under the IEEE 802.11ax indoor channel model. In Section 4.4, a design guideline table for DL MU-MIMO is proposed by unifying the factors discussed in Section 4.2 and 4.3. Finally, Section **??** concludes this chapter.

4.2 Factor 1: CSI Overhead

In 802.11ax DL transmission, AP is the transmitter which is called the beamformer, while a STA is the receiver which is called the beamformee. Beamforming depends on chan-

---

[2] Further consideration of this topic is beyond the scope of this article.

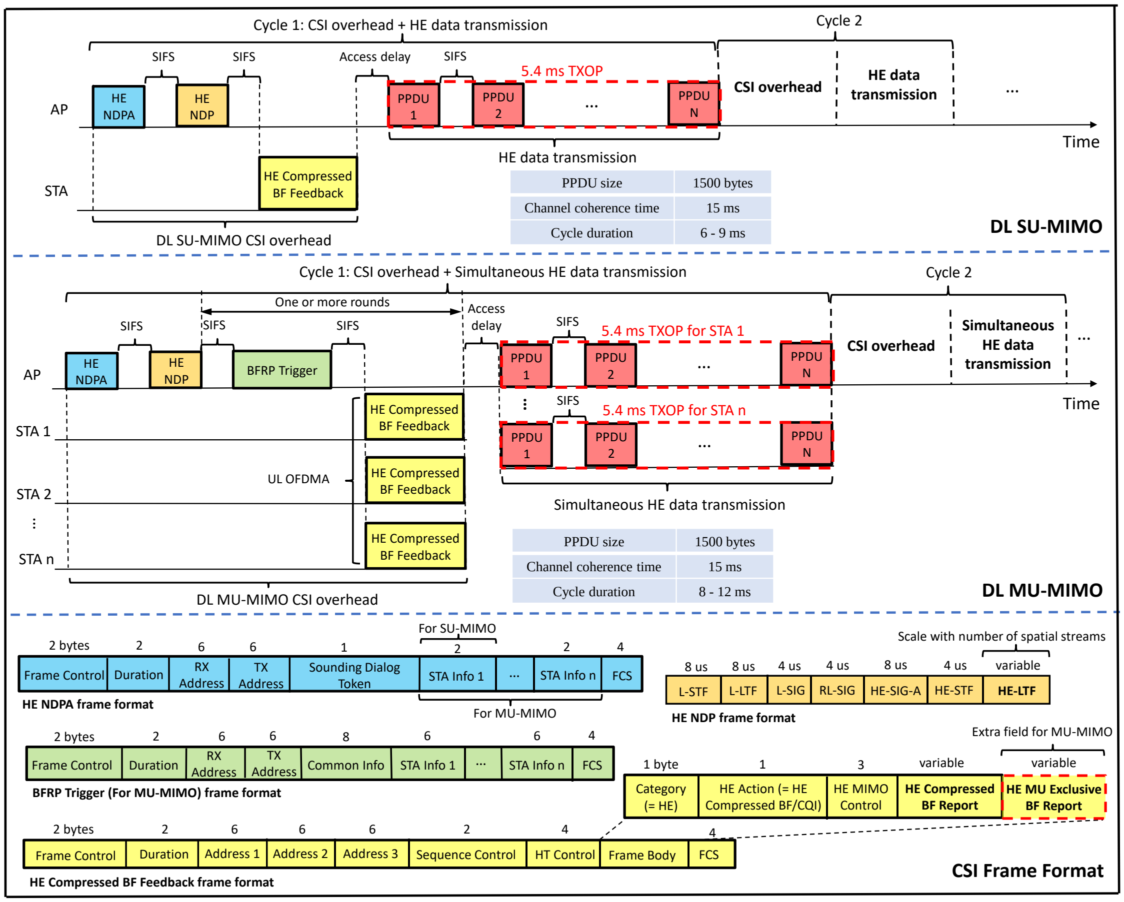

Figure 4.1: IEEE 802.11ax Channel Sounding followed by High-Efficiency (HE) Data Transmission.

nel calibration procedures, called channel sounding in the 802.11ax standard. The channel sounding allows the beamformer to gather the beamforming report(s) that characterize the beamformee location(s) and to transmit the streams toward the precise direction of the beamformee(s).

4.2.1 DL SU/MU-MIMO channel sounding

DL SU-MIMO is indicated by codebook info 0 in the High-Efficiency (HE) MIMO control field. As Fig. 4.1 shows, its channel sounding process consists of four major steps:

- The beamformer begins the process by broadcasting a Null Data Packet Announcement (NDPA) frame, which is used to gain control of the channel and identify the intended beamformee.

- The beamformer next transmits a Null Data Packet (NDP) to beamformee after a Short Interframe Space (SIFS). NDP is an empty frame that only contains the Physical Layer Protocol Data Unit (PPDU) header. The received NDP is used for channel estimation by analyzing the OFDM training symbols, called HE-LTF, whose length is a variable that depends on the number of spatial streams.

- Following receipt of the NDP, the beamformee responds with a BF feedback matrix in a compressed form. The BF feedback matrix instructs how the beamformer should steer the data frame to the beamformee with higher energy. Codebook information in the HE MIMO Control field provides the resolution schemes for compressing the BF feedback matrix.

- The beamformer receives and recovers the compressed feedback matrix that is further used as the steering matrix to direct HE data transmissions toward the beamformee.

By contrast, DL MU-MIMO, indicated by codebook info 1 in the HE MIMO control field, follows the similar channel sounding protocols as the SU-MIMO, however, several **major** differences exist:

- NDPA frame format: A HE NDPA frame in MU-MIMO includes multiple STA Info fields, one for each beamformee, while the NDPA frame in SU-MIMO only carries a single STA Info field.

- BF Report Poll (BFRP) trigger frame: The compressed BF feedback in SU-MIMO comes right after the NDP. However, the beamformer in DL MU-MIMO must use a control frame - BFRP Trigger frame that instructs each beamformees to transmit the

BF feedback simultaneously. The AP may transmit other BFRP Trigger frames to gather more feedbacks if necessary.

- Compressed BF feedback frame format: The HE MU Exclusive BF report is an extra field at the end of the frame for MU-MIMO, which thereby introduce extra CSI overhead;
- BF Feedback transmission: The BF feedback in SU-MIMO is transmitted over the UL OFDM while they are transmitted over the UL OFDMA in MU-MIMO.

4.2.2 CSI Overhead Comparison

CSI overhead in DL SU/MU-MIMO can be calculated based on the CSI frame format indicating each sub-field size, as shown in Fig. 4.1. In particular, CSI overhead is dominated by HE compressed BF feedback that contains the *HE compressed BF report* (as well as the extra sub-field - *HE MU Exclusive BF report* in MU-MIMO). The compressed BF report contains the compressed CSI for each sub-carrier, i.e., the **V-matrix** or steering/precoding matrix[3] used for digital beamforming. V-matrix is obtained by a) applying the singular value decomposition (SVD) to the full CSI, and b) compressing it to specific *Givens rotation angles* to reduce the amount of required bits. The compressed size of the V-matrix depends on the total number of Givens rotation angles as well as the number of bits used to quantize each angle, as defined in IEEE 802.11ax specification. In general, the larger the V-matrix dimension, the more the number of angles. Meanwhile, the number of bits to quantize each angle is indicated by the sub-field of codebook information choice with 1 bit in the *HE MIMO Control field.* Thus both SU- and MU- have two codebook information choices [9], however, MU-MIMO uses more bits than SU-MIMO to quantize a single angle

---

[3] The Null-steering step based on zero-forcing (ZF) and minimum mean square error (MMSE) approaches [135,138], used for precoding in DL MU-MIMO are not implemented in real AP products [15,133] because those can be implemented only if the full CSI is obtained, whereas the feedback V-matrix provides only partial CSI. Besides, null-steering step incurs additional computational complexity and thus chipset cost for the AP.

by using the same codebook information. For instance, if codebook information bit is set to 0, the number of bits to quantize an angle in SU-MIMO is 4 or 2 while they are 7 or 5 in MU-MIMO [9], implying that the compressed V-matrix in MU-MIMO has larger overhead compared to SU-MIMO. In addition, the HE compressed BF report size also scales with the number of spatial streams and the number of sub-carriers. The MU-Exclusive BF report in MU-MIMO contains the delta SNR per sub-carrier, which represents the difference from the average SNR. The MU-Exclusive BF report represents the spatial characteristics for each sub-carrier caused by the environment, the size of which scales with the number of subcarriers. Since the 802.11ax specification does not detail how this information is exploited in the design of the beamformer, its implementation is chip vendor dependent.

As discussed, channel sounding procedures introduce a significant cost in airtime because the sounding exchange must be completed before a beamformed data transmission can occur. Therefore, if the MU-MIMO BF gain is not sufficient to offset the airtime consumed by the sounding exchange, MU-MIMO throughput can be lower than the SU-MIMO in some operational scenarios.

As Fig. 4.1 shows, a cycle of CSI overhead and HE data transmission is repeated in both DL SU and MU-MIMO. In each cycle, the transmitted data for each STA is filled in one Transmit opportunity (TXOP) comprised of multiple back-to-back PPDUs (e.g., 1500 bytes) in SIFS burst mode. Thus the data transmission duration is the maximum TXOP limit (5.4 ms) compared to which the duration of access delay is negligible (typically less than a few hundred microseconds), as long as the number of STAs is not excessively large. If we assume STA's walking speed equal to 2 mph, the resulting channel coherence time [4] (15 ms) will be greater than any one cycle duration. Hence, it is reasonable to assume a block fading channel for each cycle, i.e., channel capacity is fixed in a cycle while varying across different cycles. We will use the *effective channel capacity* C_{eff} to compare the SU and MU- performance as a function of CSI overhead - defined as the average channel capacity

---

[4] Channel coherence time is defined as the time duration over which the channel is considered to be not varying.

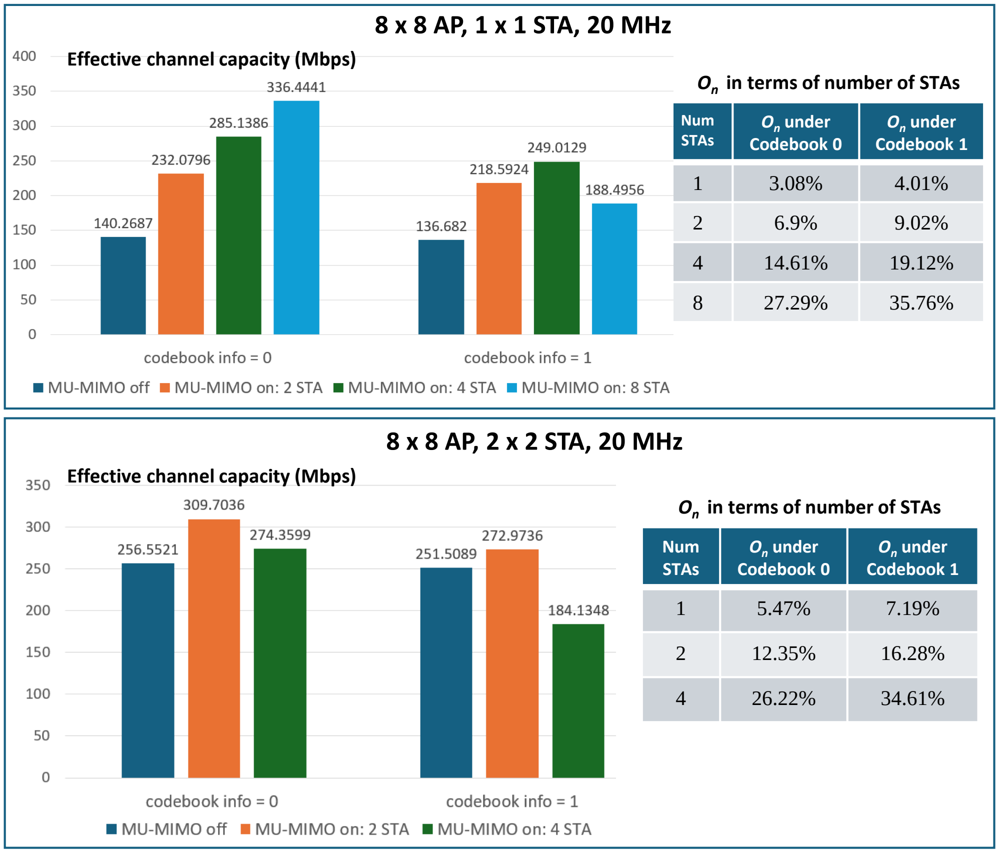

O_n in terms of number of STAs

Num STAs	O_n under Codebook 0	O_n under Codebook 1
1	3.08%	4.01%
2	6.9%	9.02%
4	14.61%	19.12%
8	27.29%	35.76%

O_n in terms of number of STAs

Num STAs	O_n under Codebook 0	O_n under Codebook 1
1	5.47%	7.19%
2	12.35%	16.28%
4	26.22%	34.61%

Figure 4.2: Effective Channel Capacity impacted by CSI Overhead. Average 25 dB SNR at the single STA in SU-MIMO.

over both CSI overhead (zero channel capacity) duration and HE data transmission duration (non-zero channel capacity), given by

$$C_{\text{eff}} = \frac{1}{N}\sum_{n,k}(1 - O_n) \cdot C_{n,k}, \tag{4.1}$$

where N denotes the total number of cycles, $C_{n,k}$ denotes the Shannon channel capacity [138] of the k-th STA in the n-th cycle, assumed to be constant due to the block fading channel. O_n is the ratio of CSI overhead airtime to the cycle duration for the n-th cycle. Eq. (4.1) applies to DL SU-MIMO when the size of k is 1. Note that $C_{n,k}$ varies across n due to time-varying channels[5], but O_n is independent of n in our model since we assume a specific setup (i.e., MIMO dimension, codebook information, and the number of selected STAs, TXOP duration).

Assuming an 8 x 8 AP, 1 x 1 STA(s), and 20 MHz channel bandwidth as in Fig. 4.2, the effective channel capacity does *not* grow linearly with the number of STAs. In particular, the effective channel capacity under codebook info 1 is greatly reduced when the number of STAs reaches 8. This can be explained by following reasons:

- CSI overhead proportion O_n shown in Fig. 4.2 grows exponentially with the number of STAs. This is because, on the one hand, an extra field - HE MU Exclusive BF report as a function of the number of sub-carriers and spatial streams - is included in HE compressed BF feedback, incurring extra CSI overhead; On the other hand, the bandwidth is shared using UL OFDMA leads to the lower UL data rate for HE compressed BF feedback transmission per STA; Thus, the DL MU-MIMO CSI overhead becomes significantly higher than SU-MIMO for a large number of STAs;

- AP transmit power is divided equally for each STA in DL MU-MIMO. As a result, $C_{n,k}$ in Eq. (4.1) will drop with increasing number of STAs due to the lower transmit power per STA.

The same phenomenon repeats for the 8 x 8 AP, 2 x 2 STA, and 20 MHz cases in Fig. 4.2; the effective channel capacity is reduced when the number of STAs reaches 4. However, this does not indicate that AP shall not support more STAs due to the lower effective channel capacity. However, inspite of this result, AP vendors may choose to support greater number of STAs on simultaneous DL as that may be independently desirable [10]. It is noteworthy that codebook info 1 (i.e., using more bits to quantize the V-matrix) always has lower effective

---

[5] For the pure analysis of CSI overhead in this section, the inter-user interference determined by spatial correlation is assumed to be zero. Thus $C_{n,k}$ in terms of n changes only due to the channel gain variations rather than variations in inter-user interference. Then, C_{eff} shown in Fig. 4.2 is the maximum effective channel capacity that DL MU-MIMO can reach.

channel capacity performance than codebook info 0 in Fig 4.2. This is because we assume the perfect channel estimation which does not produce channel estimation error under both Codebook info 0 and 1. Thus codebook info 1 with larger CSI overhead always suffers more than codebook info 0.

4.3 Factor 2: Spatial correlation

In this section, we investigate the impact of spatial correlation on the SU and MU performance in practical environmental conditions. The spatial correlation among user's is characterized by two key factors: user separation, and distance between AP and STAs. We use the Shannon channel capacity (without CSI overhead) as the metric to investigate the SU and MU throughput as a function of spatial correlation next.

4.3.1 Clustered-based multi-path channel model

We use the class of *cluster-based multipath fading channels* to model the practical environmental conditions for indoor Wi-Fi downlink operation. Such models were introduced by Saleh and Valenzuela, and extended/elaborated upon by many other researchers [138]. In particular, IEEE 802.11ax indoor channel model [134] is a typical cluster-based channel model that we have adapted by incorporating a parameter for user separation, as shown in Fig. 4.3. IEEE 802.11ax indoor channel model represents the propagation environment as a collection of scatterers grouped into clusters, where each cluster represents objects in the vicinity that act as a forward scattering source of rays that reach the receiver. Such clusters are typically represented via spatial-temporal models that capture the spatial characteristics of the environment, such as the transmit/receive antenna correlation and the distribution of objects, etc.

A particular impact on our results arises from distinction between Line-of-sight (LoS) and Non-line-of-sight (NLoS) scenarios as defined by 11ax channel model specification, depending

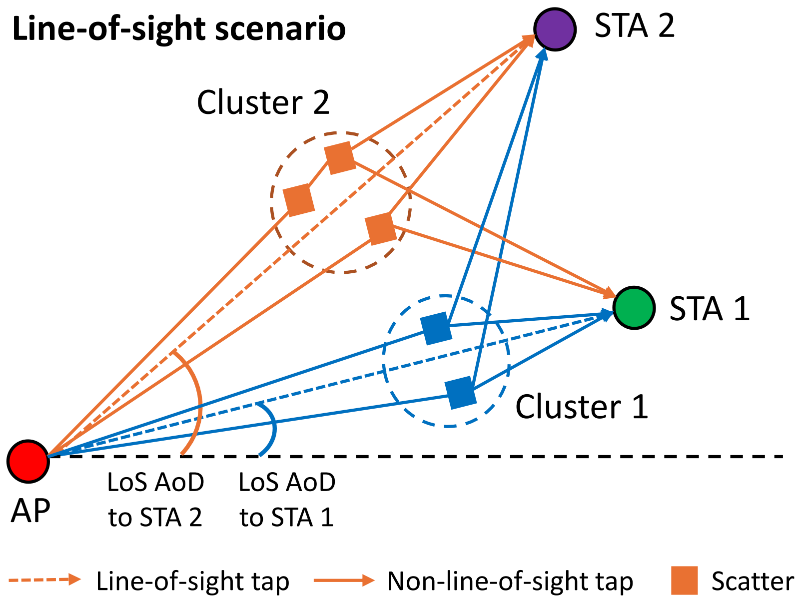

Figure 4.3: Modified IEEE 802.11ax Indoor Channel Model: DL SU (STA 1) and MU (STA 1 + 2) in Line-of-sight Scenario.

on the relationship between the breakpoint distance [6] and the distance between AP and STA(s) [134]:

- *LoS scenario* (Fig. 4.3) occurs if the distance between AP and STAs is smaller than the breakpoint distance. The received signal at each STA include a LoS component and multiple multipath-induced NLoS components within a tapped delay-line model. This results in Rician fading multipath models where the first tap (corresponding to earliest arrival at each STA) is the LoS component. Therefore, the CSI obtained at each STA in such cases includes both LoS component and NLoS components with spatial characteristics [134]; LoS CSI component depends on the transmit/receive steering vector parameterized by LoS angle of departure (AoD)/angle of arrival (AoA). Each NLoS CSI component depends on transmit/receive antenna correlation parameterized

---

[6] The breakpoint distance is defined as the distance that separates LoS and NLoS scenarios by characterizing different path loss exponents.

by NLoS mean AoD/AoA along with angular spread, and the spatial distribution of random scatterers within the cluster. The mathematical expression for LoS/NLoS CSI components can be found at [139]. Since the first LoS tap signal is typically significantly stronger than NLoS signals, the LoS CSI component dominates the CSI obtained at each STA.

- *NLoS scenario* occurs if the distance between AP and STAs is greater than the breakpoint distance; then the LoS tap signal at each STA in Fig. 4.3 is blocked. Thus, the received signals at each STA are all NLoS (hence Rayleigh fading) and the first NLoS tap signal's power is close to that of the other NLoS taps.

4.3.2 Spatial Correlation

Fig. 4.3 includes an 8 x 8 uniform linear array (ULA)-based AP whose ULA antenna spacing is half wavelength as well as two 1 x 1 STAs. The sake of using a 2-user example here is to provide key insights for readers. Extending to a larger user number will be discussed in the next section. Thus AP transmits to STA 1 if MU-MIMO is turned off and to both STA 1 and STA 2 if MU-MIMO is turned on. The spatial geometry of STAs is characterized by their angle of departure (AoD), i.e., LoS AoD to STA 1 and LoS AoD to STA 2. The user separation between STA 1 and 2 is defined as the difference between LoS AoD to STA 2 and STA 1, respectively. To investigate the impact of user separation, we fix the angular geometry of cluster 1[7] and STA 1, i.e., LoS AoD to STA 1 is set to 0^o, and the LoS AoD to STA 2 varied between 0^o and 180^o, thus the user separation between STA 1 and 2 ranges between 0^o and 180^o.

---

[7] Cluster 1's NLoS mean AoD equals the LoS AoD to STA 1; Cluster 2's NLoS mean AoD equals the LoS AoD to STA 2.

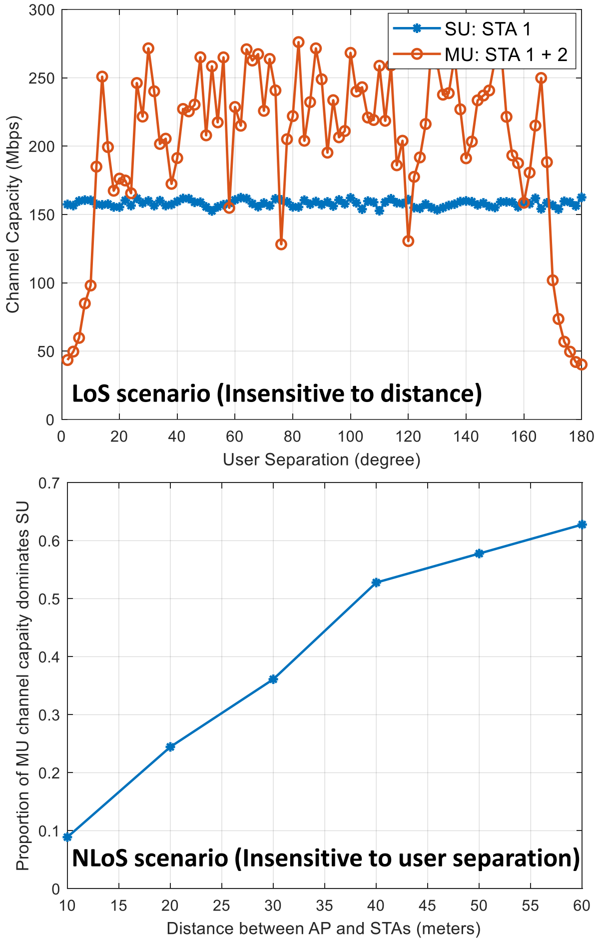

Figure 4.4: Channel Capacity impacted by Spatial Correlation. 20 dBm Transmit Power, 20 MHz Bandwidth, -174 dBm/Hz Noise Power Spectrum Density.

Dominant feature in the LoS scenario - User separation

Due to the small breakpoint distance, e.g., 10 meters, spatial correlation in the LoS scenario is not sensitive to the distance variation. Thus user separation is the single dominant feature that we explore in the LoS scenario, which is shown in Fig. 4.4. Consider a set of LoS scenarios where the distance is 8 meters and the granularity of user separation is 2^o, resulting in a total of 90 user separation scenarios. DL SU channel capacity dominates MU in 14% scenarios of which 12% scenarios lie in $0 - 12^o$ and $168 - 180^o$ user separation regions. Note that DL MU-MIMO channel capacity over $0 - 180^o$ user separation exhibits a symmetric channel capacity pattern, that can be attributed to the ULA characteristics where the LoS transmit/receive steering vectors of two STAs are identical at 0^o or 180^o user separation. Then, their dominant LoS CSI component determined by LoS transmit/receive steering vectors are also close for user separation regions close to 0^o or 180^o. As a result, the corresponding V-matrices become highly correlated, incurring significantly higher inter-user interference than other user separation regions.

Dominant feature in the NLoS scenario - Distance between AP and STAs

In the NLoS scenario, the obtained CSI includes only NLoS components, and each NLoS component (corresponding to a NLoS tap) is determined by the transmit/receive antenna correlation as well as the characteristics of scatterers. Since the latter such as their distributions, shapes and properties of materials are random, each NLoS tap consists of superposition of multiple independent individual path components leading to the complex Gaussian assumption [134]. As a result, the inter-user/inter-steam interference can vary significantly as a function of STA distance in such cases (and is insensitive to user angular separation).

The spatial correlation as a function of distance in NLoS is shown Fig. 4.4 for scenarios where the granularity of distance is 10 meters; the maximum distance for DL MU-MIMO operation with sufficiently high SNR at the STA is 60 meters. For each distance, 60 equally spaced user separations is used to calculate the proportion of scenarios in which MU channel capacity dominates SU. As shown, the proportion increases when distance increases, indicating that DL MU-MIMO benefits more than SU-MIMO at larger distance. In particular, MU becomes dominant over 50% scenarios for distances greater than 38 meters. The larger the distance is, the more the multiple scattering, reflection, and diffraction paths that decorrelate the signals received by different users. Hence, the inter-user interference is effectively reduced with the increasing distance.

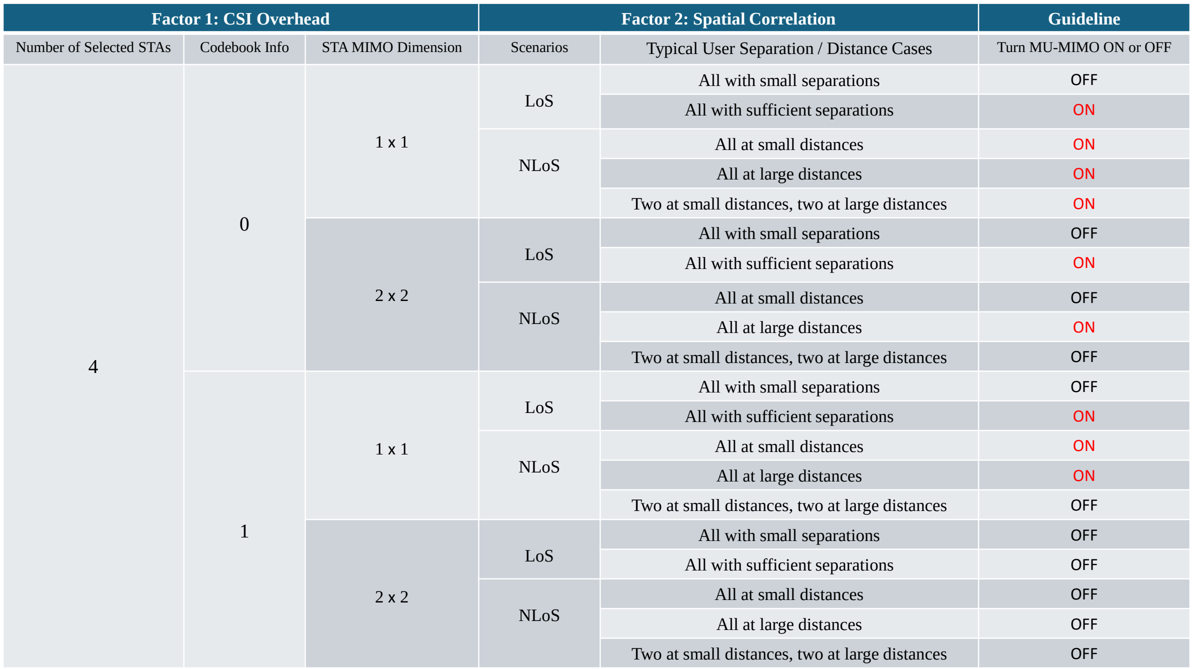

Factor 1: CSI Overhead			Factor 2: Spatial Correlation		Guideline
Number of Selected STAs	Codebook Info	STA MIMO Dimension	Scenarios	Typical User Separation / Distance Cases	Turn MU-MIMO ON or OFF
4	0	1 x 1	LoS	All with small separations	OFF
				All with sufficient separations	ON
			NLoS	All at small distances	ON
				All at large distances	ON
				Two at small distances, two at large distances	ON
		2 x 2	LoS	All with small separations	OFF
				All with sufficient separations	ON
			NLoS	All at small distances	OFF
				All at large distances	ON
				Two at small distances, two at large distances	OFF
	1	1 x 1	LoS	All with small separations	OFF
				All with sufficient separations	ON
			NLoS	All at small distances	ON
				All at large distances	ON
				Two at small distances, two at large distances	OFF
		2 x 2	LoS	All with small separations	OFF
				All with sufficient separations	OFF
			NLoS	All at small distances	OFF
				All at large distances	OFF
				Two at small distances, two at large distances	OFF

Figure 4.5: A 4-user Guideline Table for 8 x 8 AP under Modified IEEE 802.11ax Channel Model.

4.4 *Design Guideline for DL MU-MIMO*

This section provides practical design guidelines that unify the underlying factors discussed in Section 4.2 and 4.3. For the same setup as Fig. 4.4 used to obtain the channel capacity is now modified to derive the *effective* channel capacity as in Fig. 4.2. Meanwhile, We extend to a 4-user MU-MIMO operation, i,e, the user sub-set selection size is 4, indicating that upto 4 out of $X \geq 4$ STAs are selected if MU-MIMO is turned on. As the 4-user spatial correlation (where each is characterized by LoS/NLoS, user separation, and distance) results in a large set of scenario combinations, we thereby provide some typical scenarios due to the page limit. It should also be noted that real indoor channels might differ from the used channel model, that is, the exact spatial correlation threshold, such as 12^o user separation and 38 meter distance in Section 4.3, used for turning on/off MU-MIMO might be different.

However, real channels should have the same guideline trend as the used channel model under each operational scenario (without specifying specific thresholds) defined in Fig. 4.5. All results were implemented in Matlab using indoor MIMO WLAN channel models created by Schumacher et al, [139].

As the main features regarding CSI overhead are codebook information for BF compression (i.e., codebook info 0 and 1) and STA MIMO dimensions (i.e., 1 x 1 and 2 x 2 STA), there are a total of 4 operational scenarios regarding CSI overhead. Meanwhile, we provide 5 typical operational scenarios (i.e., 2 LoS and 3 NLoS scenarios [8]) regarding spatial correlation. As a result, we provide guidelines for 20 scenarios unifying both CSI overhead and spatial correlation, as shown in Fig. 4.5. Our conclusion for the 2-user case is that among these 20 scenarios, DL MU-MIMO can be turned on in 9 (45%). According to the guideline table, **DL MU-MIMO can be turned on in the following scenarios:**

- **1 x 1 STAs with sufficient user separation in LoS;**
- **2 x 2 STAs with codebook info 0 and sufficient user separation in LoS;**
- **1 x 1 STAs in NLoS;**
- **2 x 2 STAs with codebook info 0 and large distances in NLoS.**

Otherwise, DL MU-MIMO is suggested to be turned off, i.e., switch to DL SU-MIMO. Note that the condition for turning on DL MU-MIMO is more stringent for the 2 x 2 STA case, compared to the 1 x 1 STA case. This is because each spatial stream in the 2 x 2 STA case suffers more from interfering streams (self-interference from another stream for the same STA and/or streams from another STA) than the 1 x 1 STA case (only one interfering stream from another STA). Thus compared to the 1 x 1 STA case, MU-MIMO effective channel capacity is less likely to exceed SU-MIMO in the 2 x 2 STA case.

---

[8] For the operational scenario of two at small distances and two at large distances, AP is assumed to serve one of the STAs at small distances if MU-MIMO is turned off.

4.5 Summary

This chapter provides new insights about the key underlying factors (i.e., CSI overhead and spatial correlation) that have resulted in AP vendors turning off the DL MU-MIMO feature as the default setting in their products. Based on our study and analysis, guidelines as a function of operational scenarios is provided to address the fundamental question “when DL MU-MIMO should be turned on/off” for current/next-generation Wi-Fi systems.

Chapter 5

CONCLUSION & FUTURE WORK

5.1 Conclusion

In this thesis, we have investigated the resource allocation of two emerging wireless networks in the 5G/B5G era: NR sidelink mode 2 and Wi-Fi 6, with the unifying theme of the fundamentals and the performance enhancement of wireless networks by emphasizing various communication protocols across three distinct chapters. By addressing different network scenarios and developing novel approaches and algorithms tailored to these specific cases, we provide a comprehensive framework for optimizing resource allocation policies for NR sidelink mode 2 and Wi-Fi 6.

In Chapter 2, we develop a complete analytical model for MAC collision events for C-V2X mode 2, which is used to derive the PRR. Our model accounts for all key MAC parameters present in V2X mode 2, including the resource-keeping probability, the number of duplicate transmissions, and the proportion of available PRBs for reselection. We investigate the effects of these MAC parameters on PRR and on a set of intermediate performance metrics such as the probability of collision or the number of available resources. To validate our model, we provide results based on ns-3-based V2X simulation that corroborates our analysis. In Chapter 3, we analyze the baseline resource allocation approaches (Semi-persistent scheduling (SPS) described in 3GPP and Random Selection (RS)) for platoon communication, and determine that RS cannot outperform SPS no matter the resource-keeping probability set in the SPS-based broadcast environment. Thereafter, we propose an improved random selection (IRS) and find that IRS significantly mitigates packet collision from hidden terminal effects. We finally propose to employ a deep reinforcement learning algorithm, i.e., Deep Deterministic Policy Gradient (DDPG), to explore the impact of inter-vehicle collaboration further to decrease the collision probability based on local information. Our work reveals that DDPG is less sensitive than the IRS in terms of the change of resource-keeping probability in the environment, and the average scheduled delay with DDPG is also reduced compared with the IRS. In Chapter 4, we provide new insights about the key underlying factors (i.e., CSI overhead and spatial correlation) that have resulted in AP vendors turning off the DL MU-MIMO feature as the default setting in their products. Based on our study and analysis, guidelines as a function of operational scenarios is provided to address the fundamental question "when DL MU-MIMO should be turned on/off" for current/next-generation Wi-Fi systems. By a combination of analysis and computation/simulation, we attempt to answer the above question by (1) Identifying set of conditions where DL SU-MIMO outperforms MU-MIMO and vice-versa; and (2) Providing broad 'rules of thumb' regarding use of DL MU-MIMO in current/future Wi-Fi systems.

The results and contributions of this thesis demonstrate the fundamentals of resource allocation algorithms as well as the effectiveness of the proposed resource allocation algorithms in improving network performance and efficiency across a range of wireless network scenarios. By building upon the unifying theme of optimizing wireless networks with different emphasis on various communication protocols, this thesis offers valuable insights and solutions for improving the sidelink mode 2 and Wi-Fi 7 in the upcoming 6G stage.

5.2 Future Work

Future work will focus on the resource allocation optimization in Wi-Fi 7. We will consider a more realistic problem for the next-generation Wi-Fi for higher throughput, which has not been unsolved yet. That is, how often should CSI be estimated in Wi-Fi 7 under time-varying channels? This problem is driven by the fact that the estimated CSI becomes gradually outdated under time-varying channels. Thus there exists a trade-off: If the channel is estimated too frequently, large CSI overhead significantly impacts the average throughput; However, if the channel is estimated less frequently, the CSI mismatch results in the degraded SNR that further decreases the average throughput. We plan to explore an optimal channel-sounding strategy that maximizes the Wi-Fi 7 throughput.

This work will include a two-fold algorithm to enhance Wi-Fi 7 throughput performance under time-varying channels via: 1) channel sounding interval optimization; and 2) beamforming matrix prediction. We will first formulate an optimal channel-sounding interval problem as a function of CSI overhead and CSI staleness to maximize the effective link throughput, which can be solved by the proposed binary search method. Then, we plan to propose a deep learning-based beamforming matrix prediction framework to mitigate the impact of CSI staleness without incurring extra CSI overhead, which further improves the effective link throughput.

BIBLIOGRAPHY

[1] V. Weerackody, K. Benson, and S. Roy, “Who Needs Basestations When We Have Sidelinks?” *Global Communications*, vol. 2023, 2023.

[2] 3GPP, “Study on NR Vehicle-to-Everything (V2X),” The 3rd Generation Partnership Project (3GPP), Tech. Rep. TR37.885, Mar 2019.

[3] ——, “Evolved universal terrestrial radio access (E-UTRA) and evolved universal terrestrial radio access network (E-UTRAN),” The 3rd Generation Partnership Project (3GPP), Tech. Rep. TR36.300, Jun 2017.

[4] ——, “Study on enhancement of 3GPP support for 5G V2X services,” The 3rd Generation Partnership Project (3GPP), Tech. Rep. TR22.886, Dec 2018.

[5] G. Naik, B. Choudhury, and J.-M. Park, “IEEE 802.11 bd & 5G NR V2X: Evolution of radio access technologies for V2X communications,” *IEEE Access*, vol. 7, pp. 70 169–70 184, 2019.

[6] G. Giambene, M. S. Rahman, and A. Vinel, “Analysis of V2V sidelink communications for platoon applications,” in *ICC 2020-2020 IEEE International Conference on Communications (ICC).* IEEE, 2020, pp. 1–6.

[7] 3GPP, “Study on NR Vehicle-to-Everything (V2X),” The 3rd Generation Partnership Project (3GPP), Tech. Rep. TR38.885, Mar 2019.

[8] K. Ganesan, P. B. Mallick, J. Löhr, D. Karampatsis, and A. Kunz, “5G V2X architecture and radio aspects,” in *2019 IEEE Conference on Standards for Communications and Networking (CSCN).* IEEE, 2019, pp. 1–6.

[9] “IEEE Standard for Information Technology–Telecommunications and Information Exchange between Systems Local and Metropolitan Area Networks–Specific Requirements Part 11: Wireless LAN Medium Access Control (MAC) and Physical Layer (PHY) Specifications Amendment 1: Enhancements for High-Efficiency WLAN,” *IEEE Std 802.11ax-2021 (Amendment to IEEE Std 802.11-2020)*, pp. 1–767, 2021.

[10] Cisco Meraki, “Wi-Fi 6 (802.11ax) Technical Guide,” 2023.

[11] Qualcomm, "802.11ac MU-MIMO: Bridging the MIMO Gap in Wi-Fi," 2015.

[12] Signals Research Group, "MU-MIMO and the user experience," 2016.

[13] Arista Networks, "Multi-User MIMO in WiFi 6 technical white paper," 2013.

[14] Cambium Networks, "802.11ax white paper 2020 vision on 802.11ax," 2020.

[15] H. Choi, T. Gong, J. Kim, J. Shin, and S.-J. Lee, "Use MU-MIMO at your own risk—Why we don't get Gb/s Wi-Fi," *Ad Hoc Networks*, vol. 83, pp. 78–90, 2019.

[16] Extreme Networks, "Does the number of spatial streams in 802.11ax really matter?" 2017.

[17] L. Cao, S. Roy, and C. Brady, "Semi-persistent scheduling in nr sidelink mode 2: Mac packet reception ratio model and validation," *arXiv preprint arXiv:2309.16680*, 2023.

[18] L. Cao, S. Roy, and H. Yin, "Resource allocation in 5g platoon communication: Modeling, analysis and optimization," *IEEE Transactions on Vehicular Technology*, vol. 72, no. 4, pp. 5035–5048, 2022.

[19] L. Cao, L. Zhang, S. Roy, and S. Jin, "Revisiting multi-user downlink in ieee 802.11 ax: A designers guide to mu-mimo," *arXiv preprint arXiv:2406.05913*, 2024.

[20] L. Cao, H. Yin, J. Hu, and L. Zhang, "Performance analysis and improvement on dsrc application for v2v communication," in *2020 IEEE 92nd Vehicular Technology Conference (VTC2020-Fall)*. IEEE, 2020, pp. 1–6.

[21] H. Yin, P. Liu, K. Liu, L. Cao, L. Zhang, Y. Gao, and X. Hei, "ns3-ai: Fostering artificial intelligence algorithms for networking research," in *Proceedings of the 2020 Workshop on ns-3*, 2020, pp. 57–64.

[22] L. Cao and H. Yin, "Resource allocation for vehicle platooning in 5g nr-v2x via deep reinforcement learning," in *2021 IEEE International Black Sea Conference on Communications and Networking (BlackSeaCom)*. IEEE, 2021, pp. 1–7.

[23] H. Yin, Y. Zhou, L. Cao, and Y. Xu, "Channel prediction with liquid time-constant networks: an online and adaptive approach," in *2021 IEEE 94th Vehicular Technology Conference (VTC2021-Fall)*. IEEE, 2021, pp. 1–6.

[24] H. Yin, L. Cao, and X. Deng, "Scheduling and resource allocation for multi-hop urllc network in 5g sidelink," in *2021 IEEE 94th Vehicular Technology Conference (VTC2021-Fall)*. IEEE, 2021, pp. 1–7.

[25] L. Cao and H. Yin, “A blockchain-empowered platoon communication scheme for vehicular safety applications,” in *2021 IEEE 94th Vehicular Technology Conference (VTC2021-Fall).* IEEE, 2021, pp. 1–6.

[26] L. Cao, H. Yin, R. Wei, and L. Zhang, “Optimize semi-persistent scheduling in NR-V2X: An age-of-information perspective,” in *2022 IEEE Wireless Communications and Networking Conference (WCNC).* IEEE, 2022, pp. 2053–2058.

[27] L. Zhang, H. Yin, S. Roy, and L. Cao, “Multiaccess point coordination for next-gen wi-fi networks aided by deep reinforcement learning,” *IEEE Systems Journal*, vol. 17, no. 1, pp. 904–915, 2022.

[28] H. Yin, S. Roy, and L. Cao, “Routing and resource allocation for iab multi-hop network in 5g advanced,” *IEEE Transactions on Communications*, vol. 70, no. 10, pp. 6704–6717, 2022.

[29] L. Zhang, S. Roy, and L. Cao, “Architecture-algorithmic trade-offs in multi-path channel estimation for mmwave systems,” *arXiv preprint arXiv:2209.02944*, 2022.

[30] C. Brady, L. Cao, and S. Roy, “Modeling of NR C-V2X Mode 2 Throughput,” in *2022 IEEE International Workshop Technical Committee on Communications Quality and Reliability (CQR).* IEEE, 2022, pp. 19–24.

[31] P. Liu, C. Shen, C. Liu, F. J. Cintrón, L. Zhang, L. Cao, R. Rouil, and S. Roy, “5g new radio sidelink link-level simulator and performance analysis,” in *Proceedings of the 25th International ACM Conference on Modeling Analysis and Simulation of Wireless and Mobile Systems*, 2022, pp. 75–84.

[32] L. Cao, A. Kiani, A. Xiang, K. John, and T. Saboorian, “Latency-aware end-to-end multi-path data transmission for urllc services,” *arXiv preprint arXiv:2210.13740*, 2022.

[33] L. Cao, L. Zhang, S. Jin, and S. Roy, “Efficient mimo phy abstraction with imperfect csi for fast simulations,” *IEEE Wireless Communications Letters*, vol. 12, no. 3, pp. 530–534, 2023.

[34] L. Cao, L. Zhang, and S. Roy, “Efficient phy layer abstraction for 5g nr sidelink in ns-3,” in *Proceedings of the 2023 Workshop on ns-3*, 2023, pp. 115–120.

[35] P. Liu, C. Shen, C. Liu, F. J. Cintrón, L. Zhang, L. Cao, R. Rouil, and S. Roy, “Towards 5G new radio sidelink communications: A versatile link-level simulator and performance evaluation,” *Computer Communications*, 2023.

[36] L. Cao, Y. Shabara, and P. Cheraghi, "Codebook-based uplink transmission enhancement in 5g advanced: Sub-band precoding," in *2023 IEEE Virtual Conference on Communications (VCC)*. IEEE, 2023, pp. 236–240.

[37] D. Wei, L. Cao, L. Zhang, X. Gao, and H. Yin, "Non-primary channel access in ieee 802.11 uhr: Comprehensive analysis and evaluation," *arXiv preprint arXiv:2403.11300*, 2024.

[38] L. Zhang, H. Yin, S. Roy, L. Cao, X. Gao, and V. Sathya, "Ieee 802.11 be network throughput optimization with multi-link operation and ap controller," *IEEE Internet of Things Journal*, 2024.

[39] D. Wei, L. Cao, L. Zhang, X. Gao, and H. Yin, "Optimized non-primary channel access design in ieee 802.11 bn," *arXiv preprint arXiv:2405.00227*, 2024.

[40] A. Nabil, K. Kaur, C. Dietrich, and V. Marojevic, "Performance analysis of sensing-based semi-persistent scheduling in C-V2X networks," in *2018 IEEE 88th vehicular technology conference (VTC-Fall)*. IEEE, 2018, pp. 1–5.

[41] G. Cecchini, A. Bazzi, B. M. Masini, and A. Zanella, "LTEV2Vsim: An LTE-V2V simulator for the investigation of resource allocation for cooperative awareness," in *2017 5th IEEE International Conference on Models and Technologies for Intelligent Transportation Systems (MT-ITS)*. IEEE, 2017, pp. 80–85.

[42] B. McCarthy and A. O'Driscoll, "OpenCV2X mode 4: A simulation extension for cellular vehicular communication networks," in *2019 IEEE 24th International Workshop on Computer Aided Modeling and Design of Communication Links and Networks (CAMAD)*. IEEE, 2019, pp. 1–6.

[43] Z. Ali, S. Lagén, L. Giupponi, and R. Rouil, "3GPP NR V2X mode 2: overview, models and system-level evaluation," *IEEE Access*, vol. 9, pp. 89 554–89 579, 2021.

[44] C. Campolo, A. Molinaro, F. Romeo, A. Bazzi, and A. O. Berthet, "5G NR V2X: On the impact of a flexible numerology on the autonomous sidelink mode," in *2019 IEEE 2nd 5G World Forum (5GWF)*. IEEE, 2019, pp. 102–107.

[45] A. Bazzi, G. Cecchini, A. Zanella, and B. M. Masini, "Study of the impact of PHY and MAC parameters in 3GPP C-V2V mode 4," *IEEE Access*, vol. 6, pp. 71 685–71 698, 2018.

[46] M. Chen, R. Chai, H. Hu, W. Jiang, and L. He, "Performance evaluation of C-V2X mode 4 communications," in *2021 IEEE Wireless Communications and Networking Conference (WCNC)*. IEEE, 2021, pp. 1–6.

[47] Y. Mao, S. Deb, S. B. Venkatakrishnan, S. Kannan, and K. Srinivasan, “Perigee: Efficient peer-to-peer network design for blockchains,” in *Proceedings of the 39th Symposium on Principles of Distributed Computing*, 2020, pp. 428–437.

[48] A. Bakshi, Y. Mao, K. Srinivasan, and S. Parthasarathy, “Fast and efficient cross band channel prediction using machine learning,” in *The 25th Annual International Conference on Mobile Computing and Networking*, 2019, pp. 1–16.

[49] Y. Mao and S. B. Venkatakrishnan, “Less is more: Understanding network bias in proof-of-work blockchains,” *Mathematics*, vol. 11, no. 23, p. 4741, 2023.

[50] B. Xue, Y. Mao, S. B. Venkatakrishnan, and S. Kannan, “Goldfish: Peer selection using matrix completion in unstructured p2p network,” in *2023 IEEE International Conference on Blockchain and Cryptocurrency (ICBC)*. IEEE, 2023, pp. 1–9.

[51] O. Zhang, Z. Qian, Y. Mao, K. Srinivasan, and N. B. Shroff, “Erscc: Enable efficient and reliable screen-camera communication,” in *Proceedings of the Twentieth ACM International Symposium on Mobile Ad Hoc Networking and Computing*, 2019, pp. 281–290.

[52] V. Weerackody, H. Yin, and S. Roy, “Nr sidelink mode 2 in unlicensed bands: Throughput model & validation,” *IEEE Transactions on Communications*, 2024.

[53] A. Rehman, P. Di Marco, R. Valentini, and F. Santucci, “Analytical modeling of multiple access interference in C-V2X sidelink communications,” in *2022 IEEE International Mediterranean Conference on Communications and Networking (MeditCom)*. IEEE, 2022, pp. 215–220.

[54] A. Rehman, R. Valentini, E. Cinque, P. Di Marco, and F. Santucci, “On the impact of multiple access interference in LTE-V2X and NR-V2X sidelink communications,” *Sensors*, vol. 23, no. 10, p. 4901, 2023.

[55] M. Gonzalez-Martín, M. Sepulcre, R. Molina-Masegosa, and J. Gozalvez, “Analytical models of the performance of C-V2X mode 4 vehicular communications,” *IEEE Transactions on Vehicular Technology*, vol. 68, no. 2, pp. 1155–1166, 2018.

[56] X. Gu, J. Peng, Y. Cheng, X. Zhang, W. Liu, Z. Huang, and L. Cai, “Performance analysis on access collision in semi-persistent scheduling of C-V2X mode 4,” in *2021 IEEE 94th Vehicular Technology Conference (VTC2021-Fall)*. IEEE, 2021, pp. 1–5.

[57] X. Gu, J. Peng, L. Cai, Y. Cheng, X. Zhang, W. Liu, and Z. Huang, “Performance Analysis and Optimization for Semi-Persistent Scheduling in C-V2X,” *IEEE Transactions on Vehicular Technology*, vol. 72, no. 4, pp. 4628–4642, 2022.

[58] Y. Mao, M. Zhang, S. B. Venkatakrishnan, and Z. Lin, "Flashback: Enhancing proposer-builder design with future-block auctions in proof-of-stake ethereum," *arXiv preprint arXiv:2405.09465*, 2024.

[59] Y. Mao, "Efficient peer-to-peer network design for decentralized applications," Ph.D. dissertation, The Ohio State University, 2024.

[60] G. P. W. NBA, J. Haapola, and T. Samarasinghe, "A discrete-time Markov chain based comparison of the MAC layer performance of C-V2X mode 4 and IEEE 802.11 p," *IEEE Transactions on Communications*, vol. 69, no. 4, pp. 2505–2517, 2020.

[61] M. H. C. Garcia, A. Molina-Galan, M. Boban, J. Gozalvez, B. Coll-Perales, T. Şahin, and A. Kousaridas, "A tutorial on 5G NR V2X communications," *IEEE Communications Surveys & Tutorials*, vol. 23, no. 3, pp. 1972–2026, 2021.

[62] 3GPP, "Overall description of radio access network (RAN) aspects for vehicle-to-everything (V2X) based on LTE and NR," The 3rd Generation Partnership Project (3GPP), Tech. Rep. TR37.985, Jul 2020.

[63] ——, "Evolved Universal Terrestrial Radio Access (E-UTRA); Physical layer procedures," The 3rd Generation Partnership Project (3GPP), Tech. Rep. TR36.213, Dec 2020.

[64] ——, "Evolved universal terrestrial radio access (E-UTRA); medium access control (MAC) protocol specification," The 3rd Generation Partnership Project (3GPP), Tech. Rep. TR36.321, Dec 2020.

[65] ——, "Study on enhancement of 3GPP Support for 5G V2X Services," The 3rd Generation Partnership Project (3GPP), Tech. Rep. TR22.886, Dec 2018.

[66] SAE On-Road Automated Vehicle Standards Committee and others, "Taxonomy and definitions for terms related to on-road motor vehicle automated driving systems," Tech. Rep., 2014.

[67] K. Abboud, H. A. Omar, and W. Zhuang, "Interworking of DSRC and cellular network technologies for V2X communications: A survey," *IEEE transactions on vehicular technology*, vol. 65, no. 12, pp. 9457–9470, 2016.

[68] Y.-H. Xu, Q.-M. Sun, X.-R. Xu, W. Zhou, and G. Yu, "Energy efficiency and delay determinacy tradeoff in energy harvesting-powered zero-touch deterministic industrial m2m communications," *Engineering Applications of Artificial Intelligence*, vol. 121, p. 105997, 2023.

[69] Q. Ye, W. Zhuang, L. Li, and P. Vigneron, “Traffic-load-adaptive medium access control for fully connected mobile ad hoc networks,” *IEEE Transactions on Vehicular Technology*, vol. 65, no. 11, pp. 9358–9371, 2016.

[70] R. Rajamani, *Vehicle dynamics and control.* Springer Science & Business Media, 2011.

[71] M. Di Bernardo, A. Salvi, and S. Santini, “Distributed consensus strategy for platooning of vehicles in the presence of time-varying heterogeneous communication delays,” *IEEE Transactions on Intelligent Transportation Systems*, vol. 16, no. 1, pp. 102–112, 2014.

[72] G. Guo and S. Wen, “Communication scheduling and control of a platoon of vehicles in vanets,” *IEEE Transactions on intelligent transportation systems*, vol. 17, no. 6, pp. 1551–1563, 2015.

[73] H. Peng, D. Li, K. Abboud, H. Zhou, H. Zhao, W. Zhuang, and X. Shen, “Performance analysis of ieee 802.11 p dcf for multiplatooning communications with autonomous vehicles,” *IEEE Transactions on Vehicular Technology*, vol. 66, no. 3, pp. 2485–2498, 2016.

[74] Z. Xie, B. Zhou, X. Cheng, E. Schoenfeld, and F. Ye, “Fusing uwb and depth sensors for passive and context-aware vital signs monitoring,” in *2021 IEEE/ACM Conference on Connected Health: Applications, Systems and Engineering Technologies (CHASE).* IEEE, 2021, pp. 119–120.

[75] Z. Xie, B. Zhou, and F. Ye, “Signal quality detection towards practical non-touch vital sign monitoring,” in *Proceedings of the 12th ACM Conference on Bioinformatics, Computational Biology, and Health Informatics*, 2021, pp. 1–9.

[76] Z. Xie, B. Zhou, X. Cheng, E. Schoenfeld, and F. Ye, “Vitalhub: Robust, non-touch multi-user vital signs monitoring using depth camera-aided uwb,” in *2021 IEEE 9th International Conference on Healthcare Informatics (ICHI).* IEEE, 2021, pp. 320–329.

[77] Z. Xie, H. Wang, S. Han, E. Schoenfeld, and F. Ye, “Deepvs: A deep learning approach for rf-based vital signs sensing,” in *Proceedings of the 13th ACM international conference on bioinformatics, computational biology and health informatics*, 2022, pp. 1–5.

[78] J. Calabuig, J. F. Monserrat, D. Gozalvez, and O. Klemp, “Safety on the roads: LTE alternatives for sending its messages,” *IEEE Vehicular Technology Magazine*, vol. 9, no. 4, pp. 61–70, 2014.

[79] G. Araniti, C. Campolo, M. Condoluci, A. Iera, and A. Molinaro, "LTE for vehicular networking: a survey," *IEEE communications magazine*, vol. 51, no. 5, pp. 148–157, 2013.

[80] E. Yaacoub, F. Filali, and A. Abu-Dayya, "QoE enhancement of SVC video streaming over vehicular networks using cooperative LTE/802.11 p communications," *IEEE Journal of Selected Topics in Signal Processing*, vol. 9, no. 1, pp. 37–49, 2014.

[81] Z. Xie, B. Zhou, X. Cheng, E. Schoenfeld, and F. Ye, "Passive and context-aware in-home vital signs monitoring using co-located uwb-depth sensor fusion," *ACM transactions on computing for healthcare*, vol. 3, no. 4, pp. 1–31, 2022.

[82] Z. Xie, A. Nederlander, I. Park, and F. Ye, "Poster: Quantifying signal quality using autoencoder for robust rf-based respiration monitoring," in *Proceedings of the 8th ACM/IEEE International Conference on Connected Health: Applications, Systems and Engineering Technologies*, 2023, pp. 187–188.

[83] ——, "Short: Rf-q: Unsupervised signal quality assessment for robust rf-based respiration monitoring," in *Proceedings of the 8th ACM/IEEE International Conference on Connected Health: Applications, Systems and Engineering Technologies*, 2023, pp. 158–162.

[84] Z. Xie and F. Ye, "Scaling: plug-n-play device-free indoor tracking," *Scientific Reports*, vol. 14, no. 1, p. 2913, 2024.

[85] H. Peng, D. Li, Q. Ye, K. Abboud, H. Zhao, W. Zhuang, and X. Shen, "Resource allocation for cellular-based inter-vehicle communications in autonomous multiplatoons," *IEEE Transactions on Vehicular Technology*, vol. 66, no. 12, pp. 11 249–11 263, 2017.

[86] P. Wang, B. Di, H. Zhang, K. Bian, and L. Song, "Platoon cooperation in cellular V2X networks for 5G and beyond," *IEEE Transactions on Wireless Communications*, vol. 18, no. 8, pp. 3919–3932, 2019.

[87] S. Hegde, O. Blume, R. Shrivastava, and H. Bakker, "Enhanced resource scheduling for platooning in 5G V2X systems," in *2019 IEEE 2nd 5G World Forum (5GWF)*. IEEE, 2019, pp. 108–113.

[88] C. Hong, H. Shan, M. Song, W. Zhuang, Z. Xiang, Y. Wu, and X. Yu, "A joint design of platoon communication and control based on LTE-V2V," *IEEE Transactions on Vehicular Technology*, vol. 69, no. 12, pp. 15 893–15 907, 2020.

[89] K. Sehla, T. M. T. Nguyen, G. Pujolle, and P. B. Velloso, "Resource allocation modes in C-V2X: From LTE-V2X to 5G-V2X," *IEEE Internet of Things Journal*, 2022.

[90] B. Zhou, Z. Xie, and F. Ye, "Multi-modal face authentication using deep visual and acoustic features," in *ICC 2019-2019 IEEE International Conference on Communications (ICC)*. IEEE, 2019, pp. 1–6.

[91] P. Dharangutte, Z. Xie, J. Gao, E. Schoenfeld, Y. Hua, and F. Ye, "Heartinsightify: Interpreting longitudinal heart rate data for health insights through conformal clustering," in *2023 IEEE International Conference on Bioinformatics and Biomedicine (BIBM)*. IEEE, 2023, pp. 4289–4296.

[92] D. Zhou, S. Gong, L. Li, B. Gu, and M. Guizani, "Deep reinforcement learning for irs-assisted secure noma transmissions against eavesdroppers," in *2024 International Wireless Communications and Mobile Computing (IWCMC)*. IEEE, 2024, pp. 1236–1241.

[93] Y. Jeon, S. Kuk, and H. Kim, "Reducing message collisions in sensing-based semi-persistent scheduling (SPS) by using reselection lookaheads in cellular V2X," *Sensors*, vol. 18, no. 12, p. 4388, 2018.

[94] T. Maruko, S. Yasukawa, R. Kudo, S. Nagata, and M. Iwamura, "Packet collision reduction scheme for LTE V2X sidelink communications," in *2018 IEEE 88th Vehicular Technology Conference (VTC-Fall)*. IEEE, 2018, pp. 1–5.

[95] S. Sabeeh and K. Wesołowski, "Resource re-selection with adaptive modulation and collision detection in LTE V2X mode 4," in *2021 IEEE 32nd Annual International Symposium on Personal, Indoor and Mobile Radio Communications (PIMRC)*. IEEE, 2021, pp. 1005–1010.

[96] J. Zang, V. Towhidlou, and M. Shikh-Bahaei, "Collision avoidance in V2X communication networks," in *2019 IEEE Wireless Communications and Networking Conference Workshop (WCNCW)*. IEEE, 2019, pp. 1–6.

[97] 3GPP, "User equipment (ue) radio transmission and reception; part 1: Range 1 standalone," The 3rd Generation Partnership Project (3GPP), Tech. Rep. TS38.101-1, Oct 2021.

[98] ——, "User equipment (ue) radio transmission and reception; part 2: Range 2 standalone," The 3rd Generation Partnership Project (3GPP), Tech. Rep. TS38.101-2, Oct 2021.

[99] H. Yin, L. Zhang, and S. Roy, "Multiplexing urllc traffic within embb services in 5g nr: Fair scheduling," *IEEE Transactions on Communications*, vol. 69, no. 2, pp. 1080–1093, 2020.

[100] H. Yin, X. Guo, P. Liu, X. Hei, and Y. Gao, "Predicting channel quality indicators for 5g downlink scheduling in a deep learning approach," *arXiv preprint arXiv:2008.01000*, 2020.

[101] 3GPP, "Evolved Universal Terrestrial Radio Access (E-UTRA); User Equipment (UE) radio transmission and reception," The 3rd Generation Partnership Project (3GPP), Tech. Rep. TR36.101, Dec 2020.

[102] J. Chen, Y. Wang, and T. Lan, "Bringing fairness to actor-critic reinforcement learning for network utility optimization," in *IEEE INFOCOM 2021-IEEE Conference on Computer Communications*. IEEE, 2021, pp. 1–10.

[103] J. Chen, J. Chen, T. Lan, and V. Aggarwal, "Multi-agent covering option discovery based on kronecker product of factor graphs," *IEEE Transactions on Artificial Intelligence*, 2022.

[104] ——, "Multi-agent covering option discovery through kronecker product of factor graphs." in *AAMAS*, 2022, pp. 1572–1574.

[105] ——, "Scalable multi-agent covering option discovery based on kronecker graphs," *Advances in Neural Information Processing Systems*, vol. 35, pp. 30 406–30 418, 2022.

[106] J. Chen, T. Lan, and N. Choi, "Distributional-utility actor-critic for network slice performance guarantee," in *Proceedings of the Twenty-fourth International Symposium on Theory, Algorithmic Foundations, and Protocol Design for Mobile Networks and Mobile Computing*, 2023, pp. 161–170.

[107] J. Chen, L. Zhang, J. Riem, G. Adam, N. D. Bastian, and T. Lan, "Explainable learning-based intrusion detection supported by memristors," in *2023 IEEE Conference on Artificial Intelligence (CAI)*. IEEE, 2023, pp. 195–196.

[108] J. Chen, H. Zhou, Y. Mei, G. Adam, N. D. Bastian, and T. Lan, "Real-time network intrusion detection via decision transformers," *arXiv preprint arXiv:2312.07696*, 2023.

[109] J. Chen, T. Lan, and C. Joe-Wong, "Rgmcomm: Return gap minimization via discrete communications in multi-agent reinforcement learning," 2023.

[110] J. Chen, L. Zhang, J. Riem, G. Adam, N. D. Bastian, and T. Lan, "Ride: Real-time intrusion detection via explainable machine learning implemented in a memristor hardware architecture," in *2023 IEEE Conference on Dependable and Secure Computing (DSC)*. IEEE, 2023, pp. 1–8.

[111] J. Chen, J. Chen, T. Lan, and V. Aggarwal, "Learning multiagent options for tabular reinforcement learning using factor graphs," *IEEE Transactions on Artificial Intelligence*, vol. 4, no. 5, p. 1141–1153, Oct. 2023. [Online]. Available: http://dx.doi.org/10.1109/TAI.2022.3195818

[112] X. Gao, Y. Sun, D. Wei, X. Xu, H. Chen, H. Yin, and S. Cui, "Learning for semantic knowledge base-guided online feature transmission in dynamic channels," in *ICC 2024-IEEE International Conference on Communications*. IEEE, 2024, pp. 1035–1040.

[113] X. Gao, H. Yin, Y. Sun, D. Wei, X. Xu, H. Chen, W. Wu, and S. Cui, "Multi-level feature transmission in dynamic channels: A semantic knowledge base and deep reinforcement learning-enabled approach," *Authorea Preprints*, 2024.

[114] T. P. Lillicrap, J. J. Hunt, A. Pritzel, N. Heess, T. Erez, Y. Tassa, D. Silver, and D. Wierstra, "Continuous control with deep reinforcement learning," *arXiv preprint arXiv:1509.02971*, 2015.

[115] R. Bautista-Montesano, R. Galluzzi, K. Ruan, Y. Fu, and X. Di, "Autonomous navigation at unsignalized intersections: A coupled reinforcement learning and model predictive control approach," *Transportation research part C: emerging technologies*, vol. 139, p. 103662, 2022.

[116] Z. Mo, W. Li, Y. Fu, K. Ruan, and X. Di, "Cvlight: Decentralized learning for adaptive traffic signal control with connected vehicles," *Transportation research part C: emerging technologies*, vol. 141, p. 103728, 2022.

[117] K. Ruan, J. Zhang, X. Di, and E. Bareinboim, "Causal imitation learning via inverse reinforcement learning," in *The Eleventh International Conference on Learning Representations*, 2023.

[118] K. Ruan and X. Di, "Learning human driving behaviors with sequential causal imitation learning," in *Proceedings of the AAAI Conference on Artificial Intelligence*, vol. 36, no. 4, 2022, pp. 4583–4592.

[119] K. Ruan, X. He, J. Wang, X. Zhou, H. Feng, and A. Kebarighotbi, "S2e: Towards an end-to-end entity resolution solution from acoustic signal," in *ICASSP 2024-2024 IEEE International Conference on Acoustics, Speech and Signal Processing (ICASSP)*. IEEE, 2024, pp. 10 441–10 445.

[120] K. Ruan and X. Di, “Infostgcan: An information-maximizing spatial-temporal graph convolutional attention network for heterogeneous human trajectory prediction,” *Computers*, vol. 13, no. 6, p. 151, 2024.

[121] K. Ruan, X. Wang, and X. Di, “From twitter to reasoner: Understand mobility travel modes and sentiment using large language models,” *arXiv preprint arXiv:2411.02666*, 2024.

[122] K. Ruan, J. Zhang, X. Di, and E. Bareinboim, “Causal imitation for markov decision processes: A partial identification approach,” Technical Report R-104 (causalai. net/r104. pdf), Causal Artificial . . . , Tech. Rep., 2024.

[123] R. S. Sutton, D. A. McAllester, S. P. Singh, and Y. Mansour, “Policy gradient methods for reinforcement learning with function approximation,” in *Advances in neural information processing systems*, 2000, pp. 1057–1063.

[124] N. Casas, “Deep deterministic policy gradient for urban traffic light control,” *arXiv preprint arXiv:1703.09035*, 2017.

[125] X. Wang, R. A. Berry, I. Vukovic, and J. Rao, “A fixed-point model for semi-persistent scheduling of vehicular safety messages,” in *2018 IEEE 88th Vehicular Technology Conference (VTC-Fall).* IEEE, 2018, pp. 1–5.

[126] L. Zhang, H. Yin, Z. Zhou, S. Roy, and Y. Sun, “Enhancing wifi multiple access performance with federated deep reinforcement learning,” in *2020 IEEE 92nd Vehicular Technology Conference (VTC2020-Fall).* IEEE, 2020, pp. 1–6.

[127] H. Yin, S. Roy, and S. Jin, “Ieee wlans in 5 vs 6 ghz: A comparative study,” in *Proceedings of the 2022 Workshop on ns-3*, 2022, pp. 25–32.

[128] H. Yin, M. Ramanujam, J. Schaefer, S. Adermann, S. Narlanka, P. Lea, R. Netravali, and K. Chintalapudi, “{ADR-X}:{ANN-Assisted} wireless link rate adaptation for {Compute-Constrained} embedded gaming devices,” in *21st USENIX Symposium on Networked Systems Design and Implementation (NSDI 24)*, 2024, pp. 1331–1349.

[129] M. Shen, J. Zhang, H. Yin, S. Roy, and Y. Gao, “Delay in multi-link operation in ns-3: Validation and impact of traffic splitting,” in *Proceedings of the 2024 Workshop on ns-3*, 2024, pp. 19–26.

[130] H. Yin, “Towards low-latency and ultra-reliable services in wireless communication,” Ph.D. dissertation, University of Washington, 2023.

[131] J. Huang, Z. Tang, X. He, J. Zhou, D. Zhou, and C. Y.-C. Chen, "Progressive network based on detail scaling and texture extraction: A more general framework for image deraining," *Neurocomputing*, vol. 568, p. 127066, 2024.

[132] T. Higgins, "Why You Don't Need MU-MIMO," *SmallNetBuilder*, 2017.

[133] S. Sur, I. Pefkianakis, X. Zhang, and K.-H. Kim, "Practical MU-MIMO user selection on 802.11 ac commodity networks," in *Proceedings of the 22nd Annual International Conference on Mobile Computing and Networking*, 2016, pp. 122–134.

[134] J. Liu, R. Porat, N. Jindal, V. Erceg, S. Azizi *et al.*, "IEEE 802.11 ax channel model document," *Wireless LANs, Rep. IEEE*, pp. 802–11, 2014.

[135] T. Yoo and A. Goldsmith, "On the optimality of multiantenna broadcast scheduling using zero-forcing beamforming," *IEEE Journal on Selected Areas in Communications*, vol. 24, no. 3, pp. 528–541, 2006.

[136] E. Björnson, M. Bengtsson, and B. Ottersten, "Optimal multiuser transmit beamforming: A difficult problem with a simple solution structure [lecture notes]," *IEEE Signal Processing Magazine*, vol. 31, no. 4, pp. 142–148, 2014.

[137] X.-R. Xu, Y.-H. Xu, L. Suo, W. Zhou, G. Yu, and A. Nallanathan, "Uav-served energy harvesting-enabled m2m networks for green industry—a perspective of energy efficient resource management scheme," *IEEE Transactions on Green Communications and Networking*, vol. 7, no. 4, pp. 1877–1891, 2023.

[138] T. S. Rappaport, *Wireless communications: principles and practice.* Cambridge University Press, 2024.

[139] L. Schumacher and B. Dijkstra, "Description of a MATLAB implementation of the indoor MIMO WLAN channel model proposed by the IEEE 802.11 TGn channel model special committee," *Implementation note version*, vol. 5, 2004.

VITA

Journal Papers:

[1] **Liu Cao**, Sumit Roy and Hao Yin, ”Resource Allocation in 5G Platoon Communication: Modeling, Analysis and Optimization,” in IEEE Transactions on Vehicular Technology, vol. 72, no. 4, pp. 5035-5048, April 2023, doi: 10.1109/TVT.2022.3223351.

[2] **Liu Cao**, Lyutianyang Zhang, Sian Jin, and Sumit Roy, ”Efficient MIMO PHY Abstraction With Imperfect CSI for Fast Simulations”, in IEEE Wireless Communications Letters, vol. 12, no. 3, pp. 530-534, March 2023, doi: 10.1109/LWC.2022.3233542.

[3] **Liu Cao**, Sumit Roy and Collin Brady, ”Semi-Persistent Scheduling in NR Sidelink Mode 2: MAC Packet Reception Ratio Model and ns-3 Validation”, sent to IEEE Transactions on Communications, under review.

[4] **Liu Cao**, Lyutianyang Zhang, Sumit Roy, and Sian Jin, ”Revisiting Multi-User Downlink in IEEE 802.11 ax: A Designers Guide to MU-MIMO”, sent to IEEE Wireless Communications, under review.

[5] Hao Yin, Sumit Roy, and **Liu Cao**, ”Routing and Resource Allocation for IAB Multi-Hop Network in 5G Advanced,” in IEEE Transactions on Communications, vol. 70, no. 10, pp. 6704-6717, Oct. 2022, doi: 10.1109/TCOMM.2022.3200673.

[6] Lyutianyang Zhang, Hao Yin, Sumit Roy, **Liu Cao**, Xiangyu Gao, and Valin Sathya, ”IEEE 802.11be Network Throughput Optimization With Multilink Operation and AP Controller,” in IEEE Internet of Things Journal, vol. 11, no. 13, pp. 23850-23861, 1 July1, 2024, doi: 10.1109/JIOT.2024.3386653.

[7] Lyutianyang Zhang, Hao Yin, Sumit Roy and **Liu Cao**, ”Multiaccess Point Coordination for Next-Gen Wi-Fi Networks Aided by Deep Reinforcement Learning,” in IEEE Systems Journal, vol. 17, no. 1, pp. 904-915, March 2023, doi: 10.1109/JSYST.2022.3183199.

[8] Peng Liu, Chen Shen, Chunmei Liu, Fernando J. Cintrón, Lyutianyang Zhang, **Liu Cao**, Richard Rouil, Sumit Roy, Towards 5G new radio sidelink communications: A versatile link-level simulator and performance evaluation, Computer Communications, Volume 208, 2023, Pages 231-243, ISSN 0140-3664, https://doi.org/10.1016/j.comcom.2023.06.005.

Conference Papers:

[1] **Liu Cao**, Lyutianyang Zhang, and Sumit Roy, "Efficient PHY Layer Abstraction for 5G NR Sidelink in ns-3", In Proceedings of the 2023 Workshop on ns-3 (WNS3 '23). Association for Computing Machinery, New York, NY, USA, 115–120. https://doi.org/10.1145/3592149.3592163

[2] Collin Brady, **Liu Cao**, and Sumit Roy, "Modeling of NR C-V2X Mode 2 Throughput," 2022 IEEE International Workshop Technical Committee on Communications Quality and Reliability (CQR), Arlington, VA, USA, 2022, pp. 19-24, doi: 10.1109/CQR54764.2022.9918559.

[3] Peng Liu, Chen Shen, Chunmei Liu, Fernando J. Cintrón, Lyutianyang Zhang, **Liu Cao**, Richard Rouil, and Sumit Roy, "5G New Radio Sidelink Link-Level Simulator and Performance Analysis", In Proceedings of the 25th International ACM Conference on Modeling Analysis and Simulation of Wireless and Mobile Systems (MSWiM '22). Association for Computing Machinery, New York, NY, USA, 75–84. https://doi.org/10.1145/3551659.3559049

Teaching Experience:

1. Teaching Assistant, ECE Department, UW, Fall 2024, EE 505 (Probability and Random Process).

2. Teaching Assistant, ECE Department, UW, Spring 2020, EE 506 (Fundamentals of Wireless Communication).

3. Teaching Assistant, ECE Department, UW, Fall 2020, EE 416 (Random Signals for Communications and Signal Processing).

4. Teaching Assistant, ECE Department, UW, Winter 2021, EE 233 (Circuit Theory).

5. Teaching Assistant, ECE Department, UW, Summer 2020 and Spring 2021, EE 215

(Fundamentals of Electrical Engineering).

6. Teaching Assistant, ECE Department, UW, Winter 2020, EE 398 (Introduction to Professional Issues).

Industry Internship:

1. MediaTek USA Inc., San Diego, CA, June-September, 2023.
2. Futurewei Technologies Inc., Dallas, TX, June-September, 2022.